ISSN 2671-7255 (print)
ISSN 2671-7263 (online)

http://www.jees.kr

JEES

Journal of Electromagnetic Engineering and Science

Volume 21, No. 2
April 2021

KIEES

Journal of Electromagnetic Engineering and Science Volume 21, No.2 April 2021 KIEES

JEES Journal of Electromagnetic Engineering and Science

JEES
Journal of
Electromagnetic Engineering
and Science

Apr. 2021
Vol. 21 No. 2

ISSN 2671-7255 (Print)
ISSN 2671-7263 (Online)

Aims and Scope

The Journal of Electromagnetic Engineering and Science (**JEES**) is an official English-language journal of the Korean Institute of Electromagnetic and Science (**KIEES**). This journal was launched in 2001 and has been published quarterly since 2003. It is currently registered with the National Research Foundation of Korea and also indexed in Scopus, CrossRef, EBSCO, DOI/Crossref, Google Scholar, and Web of Science Core Collection as Science Citation Index Expanded (SCIE) journal. The objective of **JEES** is to publish academic as well as industrial research results and discoveries in electromagnetic engineering and science. The particular scope of the journal includes electromagnetic field theory and its applications; high frequency components, circuits, and systems; antennas; electromagnetic wave environments; and relevant industrial developments. In addition to the regular stream of contributed papers, the journal occasionally publishes special issues on specific topics of current interest, to promote a focused coverage of the selected topics. In addition, **JEES** regularly posts invited review papers by leading researchers in the relevant fields, which will provide an overview of various subjects from their own perspectives. The editors of **JEES** are aware of the importance of rapid publication for the delivery of new research results to its readers with minimum delay, and fully recognize the need for a short turnaround time. Manuscripts submitted to **JEES** take about 3–5 months from the initial submission to publication. This rapid process applies to all three types of manuscripts that **JEES** publishes: regular papers, letters, and invited papers. The publication of submitted manuscripts is subject to blind peer review, and the final decision by the Editor-in-Chief is regularly made based on three reviews from experts in the relevant area. This journal actively promotes research in electromagnetic wave-related engineering and sciences, and its ultimate aim is to benefit the global electromagnetic engineering and science community.

Subscription Information

JEES is published quarterly in January, April, July, and October. Full text PDF files are available at the official website (http://www.jees.kr).

The annual subscription rates for this journal are USD 230 for institutional members, USD 55 for regular members, USD 37 for associate members, and USD 28 for student members.

Published by
The Korean Institute of
Electromagnetic Engineering and Science

#706 Totoo Valley, 217 Saechang-ro, Yongsan-gu, Seoul, 04376, Korea
Tel : +82-2-337-9666 / 332-9665
Fax : +82-2-6390-7550
http://www.kiees.or.kr
E-mail : kees@kiees.or.kr

Printed April 25, 2021
Published April 30, 2021

Printed by
Guhmok Publishing Company
Tel : +82-2-2277-3324
Fax : +82-2-2277-3390
E-mail : guhmok@guhmok.com

KOFST
This journal was supported by the Korean Federation of Science and Technology Societies Grant funded by the Korean Government (Ministry of Education).

JEES
Journal of
Electromagnetic Engineering
and Science

Apr. 2021
Vol. 21 No. 2
ISSN 2671-7255 (Print)
ISSN 2671-7263 (Online)

REGULAR PAPERS

ERRATUM

This journal was supported by the Korean Federation of Science and Technology Societies Grant funded by the Korean Government (Ministry of Education).

JOURNAL OF ELECTROMAGNETIC ENGINEERING AND SCIENCE, VOL. 21, NO. 2, 87~94, APR. 2021

https://doi.org/10.26866/jees.2021.21.2.87
ISSN 2671-7263 (Online) · ISSN 2671-7255 (Print)

Measurement of Analog Modulation Index with a Calibrated Radio Frequency Attenuator

Chihyun Cho[1,*] · Hyunji Koo[1] · Jae-Yong Kwon[1,2] · Joo-Gwang Lee[1] · Tae-Weon Kang[1]

Abstract

This paper presents a method for the accurate and traceable measurement of the analog modulation index. A calibrated step attenuator was used as the main apparatus because it has a higher dynamic range and lower uncertainty than a spectrum analyzer or an oscilloscope. In amplitude modulation (AM), the modulation index is obtained from the amplitude difference between the carrier and the first sideband, as in the conventional method. The resolution and calibration uncertainties of the step attenuator were propagated to the measurement uncertainty of the modulation index. The uncertainty produced by the impedance mismatch and repeatability was also included. For frequency modulation (FM) and phase modulation (PM), the modulation index, β, was estimated (with the step attenuator) from the spectrum of each sideband through the nonlinear fitting of the Bessel function. Thus, the uncertainty of the fitting process was added to the uncertainty of the measurement. The three modulations, AM, FM, and PM, exhibited an expanded uncertainty (approximately 95% confidence level, k = 2) of 0.372% for 50% nominal depth of the AM, 88.8 Hz for the peak frequency deviation of 10 kHz, and 0.88 mrad for a 0.1 radian modulation index, respectively.

Key Words: Amplitude Modulation, Frequency Modulation, Measurement Uncertainty, Metrology, Microwave Measurement, Modulation Index, Phase Modulation, Sensitivity Analysis.

I. INTRODUCTION

Since the early 1900s, analog modulation has been used in wireless communication. It is still an important modulation scheme despite the extensive use of digital communications [1–3]. Analog modulation is one of the signal and pulse characteristics under the classification of the electricity and magnetism CMC (calibration and measurement capability) of the International Bureau of Weights and Measures. However, only a few National Measurement Institutes (NMIs) are listed. Moreover, there is no well-known measurement method with traceability.

Analog modulation can be measured in the frequency domain or the time domain [4–6]. In the preliminary work, we found that measuring the modulation index in the frequency domain is more effective than measurement in the time domain to reduce uncertainty. Thus, we measured the analog modulation index in the frequency domain in this study. Measuring the absolute power of a signal is usually important. Measuring the modulation index, however, requires a signal strength relative to the carrier, not the absolute power on each sideband.

In frequency modulation (FM) or phase modulation (PM), the modulation index is usually measured with the Bessel null technique. This method uses the characteristics of carrier or sideband signals have a value of zero when the modulation in-

Manuscript received July 20, 2020 ; Revised September 1, 2020 ; Accepted October 15, 2020. (ID No. 20200720-102J)
[1]Group for Electromagnetic Metrology, Korea Research Institute of Standards and Science, Daejeon, Korea.
[2]Science of Measurement Department, University of Science and Technology, Daejeon, Korea.
[*]Corresponding Author: Chihyun Cho (e-mail: chihyun.cho@kriss.re.kr)

dex achieves a specific value [5, 7]. Thus, the modulation index can only be measured at a specific value.

In this paper, we used a calibrated attenuator as the primary standard for the measurement of the modulation index. It is widely known that attenuators provide high accuracy and low uncertainty in the measurement of the relative signal strength. Moreover, the use of a calibrated attenuator readily makes the analog modulation index traceable to the measurement standard. In addition, we propose a method to measure the arbitrary FM and PM modulation indices through nonlinear fitting to overcome the limitation of the Bessel null technique. Finally, we analyze the measurement uncertainty of an analog modulation. To the best of our knowledge, this is the first comprehensive paper on analog modulation uncertainty analysis.

This paper is organized as follows. Section II describes the system for measuring the modulation index and the experimental evaluation of the effects of the impedance mismatch. Section III explains the measurement of the amplitude modulation (AM), FM, and PM modulation indices. Section IV explains the measurement of the relative amplitude of the sideband with the attenuator. Section V analyzes the uncertainty of each modulation index measurement, and Section VI concludes the paper.

II. Measurement Setup

1. Measurement Setup

Fig. 1(a) shows a block diagram and a photograph of the proposed measurement system for the analog modulation indices. The modulated signal generated by the device under test (DUT) was passed through the calibrated attenuator to the spectrum analyzer. The spectrum analyzer measured the strength of the carrier and sideband signals. Note that the spectrum analyzer had not yet been calibrated. The DUT and the spectrum analyzer were synchronized with 10 MHz, and each device was remotely controlled via a general purpose interface bus (GPIB, IEEE 488). We used a step attenuator with a resolution of 0.1 dB, which was calibrated at 0 dB to 100 dB [8].

2. Impedance Mismatch

Prior to measuring, we analyzed the effect of the impedance mismatch. The state of the impedance matching was adjusted by the insertion of an impedance stub tuner between the spectrum analyzer and the step attenuator (Fig. 2). The analog modulation index was measured by taking the relative amplitude difference between the carrier and sidebands (see a detailed explanation in Section III). Table 1 shows the measurement results. The absolute power of the carrier varied greatly on the basis of the status of the impedance stub tuner. The relative difference between the first sideband and the carrier, however, did not change regardless of the impedance matching status of the impedance tuner. Thus, the impedance mismatch did not significantly affect the analog modulation index measurement.

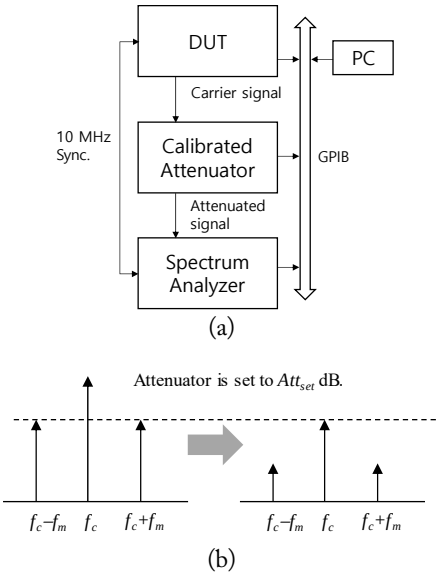

Fig. 1. (a) Block diagram of the measurement system for measuring analog modulation index. The calibrated attenuator is used to correct the raw data measured by the spectrum analyzer. (b) Calibration procedure. First, the modulation signal is measured using the spectrum analyzer. Then, the attenuator is adjusted until the carrier signal is equal to the sideband signal.

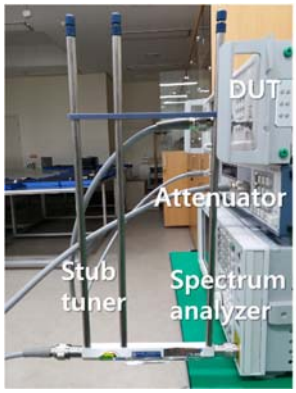

Fig. 2. Measurement setup for the impedance mismatch effect between DUT and the measurement system. The impedance stub tuner is attached to the input port of the spectrum analyzer to produce arbitrary impedance matching status.

Table 1. Effect of the impedance mismatch

Status	Power of carrier (dBm)	Difference between carrier and first sideband (dB)
A	-10	-12.482
B	-18	-12.483
C	-28	-12.467
D	-47	-12.471

III. Modulation Index Measurement

1. Amplitude Modulation

AM changes the amplitude of the carrier, $c(t)$, on the basis of the modulating signal or message, $s(t)$. If $s(t)$ is a continuous wave (CW), similar to that of the carrier, the AM signal, $y(t)$, can be easily expressed as follows:

$$c(t) = A\cos(2\pi f_c t + \phi_c) \tag{1}$$

$$s(t) = Am\cos(2\pi f_m t + \phi_m) \tag{2}$$

$$\begin{aligned} y(t) &= \left(1+\frac{s(t)}{A}\right)c(t) \\ &= A\cos(2\pi f_c t+\phi_c)+\frac{1}{2}Am\left(\cos\left(2\pi(f_c+f_m)t+\phi_c+\phi_m\right)\right) \\ &+\frac{1}{2}Am\left(\cos\left(2\pi(f_c-f_m)t+\phi_c-\phi_m\right)\right) \end{aligned} \tag{3}$$

where A is the amplitude of the carrier and m is the modulation index of AM. Thus, the amplitude of the sideband signal ($f_c \pm f_m$) changes in proportion to the modulation index, and the modulation index is calculated as follows:

$$m = \frac{2V_{SB}}{V_C} = 10^{\frac{\Delta P + 20\log_{10}(2)}{20}} \tag{4}$$

$$\Delta P = 20\log_{10}\left(V_{SB}/V_C\right) \tag{5}$$

where V_C and V_{SB} are the amplitude of the carrier and sideband, respectively. The differences between the carrier and sideband signals on the dB scale are represented by ΔP, and it is easily obtained from the delta marker on the spectrum analyzer. In this paper, all the measured values were corrected with the calibrated attenuator for traceability to the measurement standard (details are provided in Section IV).

Fig. 3 shows the AM measurement results. For the DUT, the modulation index and the frequency of the modulating signal, f_m, were set to 50% and 50 kHz, respectively. Thus, the frequency interval between the carrier and sideband signals became 50 kHz. The nonlinear distortion was generated in the DUT because the large modulation index of 50% produced additional harmonics at $f_c \pm nf_m$ ($n > 2$). In theory, both of the first sidebands should have the same amplitude; however, they should exhibit asymmetric characteristics in the presence of FM distortion [9]. In this study, the average value of the two signals was used as the V_{SB} because the difference between them was very small, less than 0.005 dB. This value is counted as the standard uncertainty for the unbalanced sidebands, assuming a rectangular distribution of ±0.0025 dB.

2. Angle Modulation (FM and PM)

FM is expressed as (6), where Δf_p indicates the peak frequency deviation. Therefore, the changes in the frequency of $y(t)$ depend on $s(t)$. The amplitude, A, is time invariant:

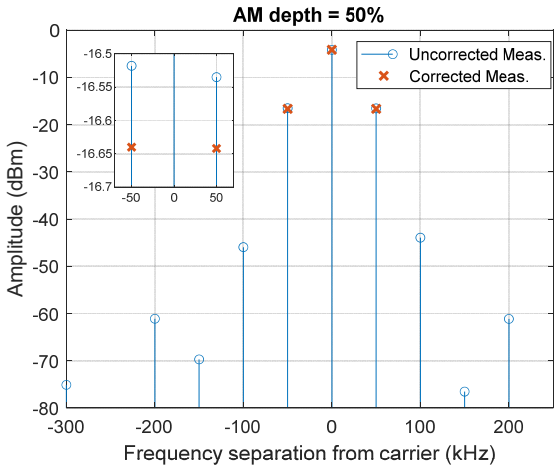

Fig. 3. Measurement results for amplitude modulation (AM) with 50% of the AM depth where the carrier frequency is 500 MHz and the modulation repetition rate is 50 kHz. The uncorrected (raw measurement) and corrected (using the calibrated attenuator) amplitudes are represented with '—O' and 'X', respectively.

$$y(t) = A\cos\left(2\pi f_c t + 2\pi\Delta f_p \int_0^t s(\tau)d\tau\right) \tag{6}$$

If s(t) is CW, as was the case for AM, (6) can be represented as follows:

$$\begin{aligned} y(t) &= A\cos\left(2\pi f_c t + \phi_c + \frac{\Delta f_p}{f_m}\sin(2\pi f_m t + \phi_m)\right) \\ &= A\cos\left(2\pi f_c t + \phi_c + \beta\sin(2\pi f_m t + \phi_m)\right) \end{aligned} \tag{7}$$

where $\beta = \Delta f_p / f_m$ indicates the FM modulation index. Usually, the peak frequency deviation, Δf_p, is measured for a given frequency of the modulating signal, f_m. Eq. (7) also represents PM given that $s(t) = \cos(2\pi f_m t)$ causes a phase change on y(t). Thus, when $s(t)$ is a sinusoidal function, the FM and PM have the same form, and they are commonly referred to as angle modulation. Mathematically, (7) can be expressed as the sum of the Bessel function of the first kind J as follows:

$$\begin{aligned} A\Bigg(&\sum_{k=0}^{\infty}\left|J_k(\beta)\right|\cos\left(2\pi(f_c+kf_m)t+\phi_c+k\phi_m\right) \\ &+\sum_{k=-\infty}^{-1}\left|J_k(\beta)\right|\cos\left(2\pi(f_c+kf_m)t+\phi_c+k(\phi_m+\pi)\right)\Bigg) \end{aligned} \tag{8}$$

where k is the order of the sidebands. For example, when $s(t)$ is a CW, the amplitude values of the carrier, first sideband, and second sideband are $AJ_0(\beta)$, $AJ_1(\beta)$, and $AJ_2(\beta)$, respectively. As stated in previous section, the calculation of analog modulation index requires the relative difference between the carrier and each sideband. Therefore, the amplitude of carrier $AJ_0(\beta)$ can be normalized to 1.

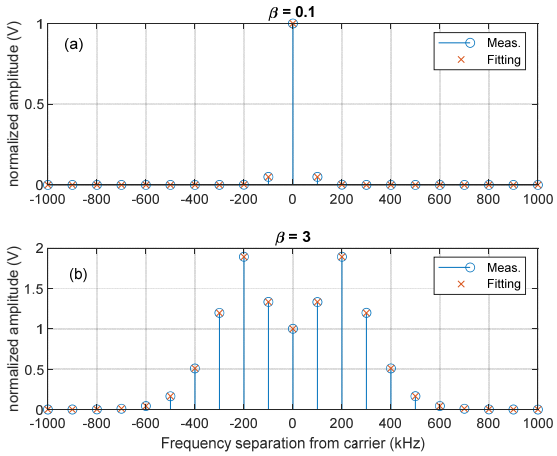

Fig. 4. Measurement results for phase modulation (PM) where the carrier frequency (f_c) is 500 MHz and the modulating signal (f_m) frequency is 100 kHz. (a) $\beta = 0.1$; (b) $\beta = 3$. The calibrated amplitude using the attenuator and the fitting result are represented with '—O' and 'X', respectively.

Then, the angle modulation index β can be estimated by minimizing the difference between the measurement and estimated values through nonlinear least squares fitting:

$$\sum_{k=-n}^{n} \frac{y_{\text{meas}}(k)}{y_{\text{meas}}(0)} - \frac{|J_k(\beta)|}{|J_0(\beta)|} \tag{9}$$

Here $y_{\text{meas}}(k)$ is the measured value of the k-th sideband. The *nlinfit* function in the MATLAB environment was applied as the estimator [10]. This is based on the Levenberg-Marquardt nonlinear least squares algorithm [11]. Nonlinear fitting problems often reach the local minima or slowly converge depending on the initial value. Robust results were obtained from the initial β, which is Δf_p divided by f_m (both are the values for the DUT setting).

Fig. 4 shows the measurement results. As was previously described, the number and shape of the generated sidebands depend on β. The fitted results ("x" marks) on the basis (9) agree well with the measured results (solid line). Estimation of β using 23 sideband measurements takes less than 0.05 seconds on an Intel Xeon E5 2.4 GHz CPU.

IV. Calibration of Spectrum Analyzer with the Attenuator

The power of the frequency spectrum can usually be measured with a spectrum analyzer. As described in the previous section, the relative difference of the sideband signals, rather than the absolute power spectrum, was necessary to assess the measurement modulation index. Thus, for reducing measurement uncertainty and increasing precision, the calibrated attenuator is superior to the spectrum analyzer because of its higher dynamic range and lower uncertainty.

The difference between the carrier and sidebands, ΔP, as measured by a spectrum analyzer, can be corrected with a calibrated attenuator, as shown in Fig. 1(b). First, the modulation signal is measured using the spectrum analyzer. Then, the attenuator is adjusted until the carrier signal is equal to the sideband signal. Now the setting value of the attenuator Att_{set} can replace the uncalibrated ΔP. However, the reduced carrier signal may not be exactly the same as the power level of sidebands. Thus, the calibrated value can be calculated as follows:

$$\Delta P_{\text{corr}} = \Delta P_{\text{SA}} - Att_{\text{set}} - \varepsilon \tag{10}$$

where ΔP_{corr} is the corrected difference on the basis of the attenuator. ΔP_{SA} is the raw measurement using the spectrum analyzer, and ε is the residual error that represents the power difference between the sidebands and the reduced carrier signal after the attenuator is set.

V. Uncertainty Analysis

1. Uncertainty of Amplitude Modulation Measurement

The measuring uncertainty of the AM modulation index is caused by the uncertainty introduced by the attenuator and the impedance mismatch between the DUT and the attenuator. The attenuator had a reading uncertainty of $0.1/(2\sqrt{3})$ dB obtained from a resolution of 0.1 dB and a calibration uncertainty of 0.012 dB. If we actually correct the impedance mismatch by using the measured impedance values, the associated uncertainty will significantly increase due to the uncertainty of a vector network analyzer. To resolve this, we measured the difference the carrier and first sideband of the AM signal under an arbitrary matching condition in Table 1. To account for the uncertainty of the impedance mismatch for the scheme above, the standard deviation was obtained from the measured values in Table 1. Next, (4) was differentiated to propagate each uncertainty to the AM modulation index. The obtained sensitivity coefficient was $\log(10)\times 10^{\frac{\Delta P + 20\log 10(2)}{20}} / 20$. The coefficient was dependent on ΔP; thus, the large modulation index produced a large measurement uncertainty. Type A uncertainty was evaluated from 10 repeated measurements. The uncertainty budget is summarized in Table 2. The modulation index of 50% was measured, and the combined standard uncertainty, $u_c(m)$ 0.186%, was obtained by taking the root sum of squares of the uncertainty contributions presented in Table 2. Since the effective degree of freedom is sufficiently large, the expanded uncertainty $U(m)$ at approximately 95% confidence level is obtained by multiplying $u_c(m)$ by 2.

2. Uncertainty for Frequency and Phase Modulation Measurement

Tables 3 and 4 show the uncertainty budget for FM and PM, respectively. In both cases, the angle modulation required additional uncertainty for estimating β from the measured amplitude of each sideband. Unfortunately, the fitting uncertainty for β could no longer be regarded as analytical. Instead, it was calculated from the residuals, which were calculated from the difference between the fitting model and measurements [12, 13]:

$$\sigma^2_{\text{residual}} = \sum_{k=-n}^{n} \left| \frac{y_{\text{meas}}(k)}{y_{\text{meas}}(0)} - \frac{|J_k(\beta)|}{|J_0(\beta)|} \right|^2 / (l-p) \tag{11}$$

$$\sigma^2_{\beta} = \left(\frac{\partial \sigma_{\text{residial}}}{\partial \beta} \right)^2 \sigma^2_{\text{residual}} \tag{12}$$

where l is the number of sidebands used in the measurement, including the carrier; thus, l is equal to $2n+1$. The number of unknown parameter β used in the fitting process, i.e., 1, is indicated by p. Therefore, the covariance for the fitting parameter

Table 2. Uncertainty budget for AM modulation (f_m = 50 kHz and m = 50%)

Uncertainty	Standard uncertainty	Sensitivity coefficient	Uncertainty contribution	Type	Probability distribution	Degree of freedom
Attenuator						
Resolution	0.029 dB	$\log(10)\times 10^{\frac{\Delta P+20\log 10(2)}{20}}/20$	0.167%	B	Rectangular	∞
Calibration uncertainty	0.012 dB	$\log(10)\times 10^{\frac{\Delta P+20\log 10(2)}{20}}/20$	0.069%	B	Normal	∞
Impedance mismatch	0.008 dB	$\log(10)\times 10^{\frac{\Delta P+20\log 10(2)}{20}}/20$	0.046%	B	Normal	∞
Imbalance of sidebands	0.002 dB	$\log(10)\times 10^{\frac{\Delta P+20\log 10(2)}{20}}/20$	0.012%	B	Rectangular	∞
Repeatability	0.003%	1	0.003%	A	Normal	9
$u_c(m)$	-	-	0.186%	-	Normal	∞
$U(m)$	-	-	0.372%	-	Normal (k = 2)	-

Table 3. Uncertainty budget for FM modulation (f_m = 100 kHz and Δf_p = 10 kHz, 50 kHz, 100 kHz)

Uncertainty	Standard uncertainty			Sensitivity coefficient	Uncertainty contribution			Type	Probability distribution	Degree of freedom
	10 kHz	50 kHz	100 kHz		10 kHz	50 kHz	100 kHz			
Fitting uncertainty	1.6 Hz	21.1 Hz	10.5 Hz	1	1.6 Hz	21.1 Hz	10.5 Hz	B	Normal	-
Attenuator										
Resolution		0.029 dB			40.9 Hz	182.7 Hz	261.8 Hz	B	Rectangular	∞
Calibration uncertainty		0.012 dB			17.0 Hz	76.3 Hz	108.6 Hz	B	Normal	∞
Impedance mismatch	2.9 Hz	14.8 Hz	29.6 Hz	1	2.9 Hz	14.8 Hz	29.6 Hz	B	Normal	∞
Repeatability	1.4 Hz	11 Hz	17.7 Hz	1	1.4 Hz	11 Hz	17.7 Hz	A	Normal	9
$u_c(m)$		-		-	44.4 Hz	213.5 Hz	285.7 Hz	-	Normal	∞
$U(m)$		-		-	88.8 Hz	427.0 Hz	571.4 Hz	-	Normal (k = 2)	-

Table 4. Uncertainty budget for PM modulation (f_m = 100 kHz and β = 0.1 rad, 1 rad, 3 rad)

Uncertainty	Standard uncertainty			Sensitivity coefficient	Uncertainty contribution			Type	Probability distribution	Degree of freedom
	0.1 rad	1 rad	3 rad		0.1 rad	1 rad	3 rad			
Fitting uncertainty	0.03 mrad	0.34 mrad	0.11 mrad	1	0.03 mrad	0.26 mrad	0.11 mrad	B	-	-
Attenuator										
Resolution		0.029 dB		-	0.40 mrad	2.63 mrad	1.43 mrad	B	Rectangular	∞
Calibration uncertainty		0.012 dB		-	0.17 mrad	1.09 mrad	0.60 mrad	B	Normal	∞
Impedance mismatch	0.07 mrad	0.21 mrad	0.21 mrad	1	0.07 mrad	0.21 mrad	0.21 mrad	B	Normal	∞
Repeatability	0.03 mrad	0.15 mrad	0.15 mrad	1	0.03 mrad	0.15 mrad	0.15 mrad	A	Normal	9
$u_c(m)$		-		-	0.44 mrad	2.85 mrad	1.56 mrad	-	Normal	∞
$U(m)$		-		-	0.88 mrad	5.70 mrad	3.12 mrad	-	Normal (k = 2)	-

σ_β^2 was calculated using (12) with the fitting residuals $\sigma_{\text{residual}}^2$. It must be noted that σ_β directly became the fitting uncertainty of β in PM. In the case of FM, the sensitivity coefficient was f_m because the peak frequency deviation was $\Delta f_\text{p} = f_\text{m}\beta$. Thus, the covariance of the peak frequency deviation $\sigma_{\Delta f_p}^2$ for FM was calculated as follows:

$$\sigma_{\Delta f}^2 = \left(\frac{\partial \Delta f_p}{\partial \beta}\right)^2 \sigma_\beta^2 = f_m^2 \sigma_\beta^2 \tag{13}$$

The uncertainty of the attenuator could not be analytically propagated to the uncertainty of the FM and PM modulation indices because of the fitting process. Thus, Monte Carlo simulations were used to account for the uncertainty of the attenuator. The Monte Carlo simulations were performed separately for the reading and the calibration uncertainty of the attenuator because of their rectangular and normal distribution, respectively. The results are summarized in Tables 3 and 4. In addition, the impedance mismatch and repeatability uncertainties were accounted for in the same way as was done for AM. As shown in Fig. 2, the uncertainty of the impedance mismatch was evaluated by the insertion of the impedance tuner between the spectrum analyzer and the attenuator and the adjustment of the state of the tuner. The expanded uncertainty combining the above-described fitting uncertainty, attenuator uncertainty, impedance mismatch uncertainty, and repeatability was observed at 88.8 Hz to 571.4 Hz for FM ($k = 2$) and 0.88 mrad to 5.70 mrad ($k = 2$) for PM.

VI. Conclusion

We proposed an accurate method for measuring the analog modulation index. A calibrated attenuator was used to reduce measurement uncertainty and to ensure traceability. In the case of AM, the modulation index was measured by the power ratio of the first sideband and the carrier, as in the conventional method, and the measurement uncertainty was derived analytically. The 50% AM modulation index exhibited an expanded uncertainty ($k = 2$) of 0.372%. For FM and PM, the modulation index was measured through the nonlinear fitting of the Bessel function of the first kind by using the measured sidebands. Unlike the case for the Bessel null technique, the arbitrary modulation index could be measured. The measurement uncertainty obtained by the Monte Carlo simulation was 88.8 Hz for 10 kHz FM modulation and 0.88 mrad for 0.1 rad PM modulation. It is expected that the measurement uncertainty of analog modulation can be further improved with the application of an attenuator with a higher resolution.

This research was supported by Physical Metrology for National Strategic Needs, funded by the Korea Research Institute of Standards and Science (No. KRISS-2020-GP2020-0002).

Appendix

The signal v_SA received by the spectrum analyzer is calculated as follows [14].

$$v_\text{DUT} = \frac{v_\text{SA}}{h\, S_{21}}\left(1 - \Gamma_\text{DUT} S_{11} - \Gamma_\text{SA} S_{22} - \Gamma_\text{DUT}\Gamma_\text{SA}(S_{21}S_{12} - S_{11}S_{22})\right) \tag{14}$$

where v_DUT, Γ_DUT, Γ_SA, S_ij, and h are the output signal of the DUT, the reflection coefficient of the DUT, the reflection coefficient of the spectrum analyzer, S-parameters of the attenuator, and the frequency response of the spectrum analyzer, respectively. The frequency response of the sampler in most spectrum analyzers can be calibrated using [14–16]. Here, we assume $h = 1$ due to the narrow bandwidth of the analog modulation. In addition, when Γ_DUT, Γ_SA, S_{11}, and S_{22} are negligibly small, the above formula is simplified as below.

$$v_\text{DUT} = \frac{v_\text{SA}}{S_{21}}$$

Note that most apparatuses have a small reflection coefficient. However, if the reflection coefficient is not so small that it is negligible, 10 dB attenuators with low reflection coefficients or tuners can be used as pads to reduce the mismatch between the DUT, the step attenuator, and the spectrum analyzer. Moreover, the output signal of the DUT can be calculated using (14) to include the mismatch effect. The corrected difference of the carrier and sidebands, ΔP_corr, can be calculated at a dB scale as follows:

$$\begin{aligned}\Delta P_\text{corr} &= 20\log_{10}\frac{V_\text{DUT}^\text{SB}}{V_\text{DUT}^\text{C}} \\ &= 20\log_{10}\left(\frac{V_\text{SA}^\text{SB}}{V_\text{SA}^\text{C}}\frac{S_{21}^C}{S_{21}^\text{SB}}\right) = \Delta P_\text{SA} - Att_{set}\end{aligned} \tag{15}$$

where superscripts SB and C represent the sidebands and carrier, respectively.

References

[1] I. Bahceci and A. K. Khandani, "Linear estimation of correlated data in wireless sensor networks with optimum power allocation and analog modulation," *IEEE Transactions on Communications*, vol. 56, no. 7, pp. 1146–1156, 2008.

[2] H. Guldemir and A. Sengur, "Comparison of clustering algorithms for analog modulation classification," *Expert Systems with Applications*, vol. 30, no. 4, pp. 642–649, 2006.

[3] C. Carlsson, H. Martinsson, R. Schatz, J. Halonen, and A. Larsson, "Analog modulation properties of oxide confined VCSELs at microwave frequencies," *Journal of Lightwave Technology*, vol. 20, no. 9, pp. 1740–1749, 2002.

[4] D. A. Humphreys, M. R. Harper, and P. Roberts, "Preliminary results for a traceable amplitude modulation measurement technique using in-phase and quadrature referencing," in *Proceedings of 2007 International Waveform Diversity and Design Conference*, Pisa, Italy, 2007, pp. 145–149.

[5] Keysight Technologies, "Spectrum Analysis Amplitude and Frequency Modulation," 2014; https://www.keysight.com/kr/ko/assets/7018-06742/application-notes/5954-9130.pdf.

[6] J. G. Lee, J. H. Kim, T. W. Kang, S. H. Won, and D. J. Lee, "RF peak power calibration of modulated signals," *IEEE Transactions on Instrumentation and Measurement*, vol. 60, no. 7, pp. 2621–2626, 2011.

[7] P. Roberts, "The challenges of precision analog modulation measurement," in *Proceedings of the Measurement Science Conference*, Long Beach, CA, 2007.

[8] J. G. Lee, J. H. Kim, J. I. Park, and U. T. Kang, "Uncertainty evaluation of a broadband attenuation standard," *IEEE Transactions on Instrumentation and Measurement*, vol. 54, no. 2, pp. 705–708, 2005.

[9] S. Matejka, "Accurate AM depth measurement in the presence of angle modulation," in *Proceedings of 2007 17th International Conference Radioelektronika*, Brno, Czech Republic, 2007, pp. 1–4.

[10] Mathworks, "MATLAB R2019b," 2019; https://www.mathworks.com.

[11] G. A. F. Seber and C. J. Wild, *Nonlinear Regression*. Hoboken, NJ: John Wiley & Sons, 2003

[12] C. Cho, J. G. Lee, T. W. Kang, and N. W. Kang, "Calibration and uncertainty analysis of sample-time error on high jitter of samplers," *Journal of Electromagnetic Engineering and Science*, vol. 18, no. 3, pp. 169–174, 2018.

[13] S. van de Geer, "Least squares estimation," in *Encyclopedia of Statistics in Behavioral Science*. Hoboken, NJ: John Wiley & Sons, 2005, pp. 1041–1045.

[14] T. S. Clement, P. D. Hale, D. F. Williams, C. M. Wang, A. Dienstfrey, and D. A. Keenan, "Calibration of sampling oscilloscopes with high-speed photodiodes," *IEEE Transactions on Microwave Theory and Techniques*, vol. 54, no. 8, pp. 3173–3181, 2006.

[15] A. Dienstfrey, P. D. Hale, D. A. Keenan, T. S. Clement, and D. F. Williams, "Minimum-phase calibration of sampling oscilloscopes," *IEEE Transactions on Microwave Theory and Techniques*, vol. 54, no. 8, pp. 3197–3208, 2006.

[16] C. Cho, H. Koo, J. Y. Kwon, and J. G. Lee, "Uncertainty analysis for characterization of a commercial real-time oscilloscope using a calibrated pulse standard," *IEEE Access*, vol. 7, pp. 159724–159730, 2019.

Chihyun Cho

received the B.S., M.S., and Ph.D. degrees in electronic and electrical engineering from Hongik University, Seoul, South Korea, in 2004, 2006, and 2009, respectively. From 2009 to 2012, he participated in the development of military communication systems at the Communication R&D Center, Samsung Thales, Seongnam, South Korea. Since 2012, he has worked with the Korea Research Institute of Standards and Science (KRISS), Daejeon, South Korea. In 2014, he was a guest researcher at the National Institute of Standards and Technology (NIST) in Boulder, CO, USA. He also served on the Presidential Advisory Council on Science and Technology (PACST) in Seoul, South Korea, from 2016 to 2017. His current research interests include microwave metrology, time domain measurement, and communication standards.

Hyunji Koo

received the B.S. and Ph.D. degrees in electrical engineering from Korea Advanced Institute of Science and Technology (KAIST), Daejeon, Korea in 2008 and 2015, respectively. From March to August 2015, she was a Post-doctoral Research Fellow at the School of Electrical Engineering in KAIST. Since September 2015, she has been a Senior Research Scientist at the Center for Electromagnetic Standards in the Korea Research Institute of Standards and Science (KRISS), Daejeon, Korea. In 2018, she was a visiting researcher at the National Physical Laboratory (NPL), Teddington, UK. Her current research interests include characterization of on-wafer or PCB devices.

Jae-Yong Kwon

received the B.S. degree in electronics from Kyungpook National University, Daegu, South Korea, in 1995, and M.S. and Ph.D. degrees in electrical engineering from the Korea Advanced Institute of Science and Technology, Daejeon, South Korea, in 1998 and 2002, respectively. He was a Visiting Scientist with the Department of High-Frequency and Semiconductor System Technologies, Technical University of Berlin, Berlin, Germany, and with the National Institute of Standards and Technology, Boulder, CO, USA, in 2001 and 2010, respectively. From 2002 to 2005, he was a Senior Research Engineer with the Devices and Materials Laboratory, LG Electronics Institute of Technology, Seoul, South Korea. Since 2005, he has been a Principal Research Scientist with the Division of Physical Metrology, Center for Electromagnetic Metrology, Korea Research Institute of Standards and Science, Daejeon. Since 2013, he has been a professor of the science of measurement with the University of Science and Technology, Daejeon. His current research interests include electromagnetic power, impedance, and antenna measurement.

Joo-Gwang Lee

was born in South Korea in 1960. He received the B.S. degree in electronic engineering from Hanyang University, Seoul, South Korea, in 1984, and the M.S. and Ph.D. degrees from the Korea Advanced Institute of Science and Technology, Daejeon, South Korea, in 1994 and 2000, respectively. Since 1986, he has been with the Korea Research Institute of Standards and Science, Daejeon. His current research interests include radio-frequency and microwave measurements, time-domain metrology, and electromagnetic compatibility.

Tae-Weon Kang

received the B.S. degree in electronics engineering from Kyungpook National University, Daegu, Korea, in 1988, and the M.S. and the Ph.D. degrees in electronic and electrical engineering from the Pohang University of Science and Technology, Pohang, Korea, in 1990 and 2001, respectively. He joined the Center for Electromagnetic Wave, Korea Research Institute of Standards and Science (KRISS), Daejeon, Korea, in 1990. In 2002, he spent a year as a visiting researcher under the Korea Science and Engineering Foundation for Post-Doctoral Fellowship Program with the George Green Institute for Electromagnetics Research, University of Nottingham, Nottingham, UK, where he was involved in measurement of absorbing performance of electromagnetic absorbers and a generalized transmission line modeling method. He has been involved in electromagnetic metrology and is currently a principal research scientist. His current research interests include electromagnetic metrology, such as electromagnetic power, noise, and antenna characteristics, and numerical modeling in electromagnetic compatibility.

JOURNAL OF ELECTROMAGNETIC ENGINEERING AND SCIENCE, VOL. 21, NO. 2, 95~103, APR. 2021

https://doi.org/10.26866/jees.2021.21.2.95
ISSN 2671-7263 (Online) · ISSN 2671-7255 (Print)

Improving the Force and Time Response of a DC Solenoid Electromagnetic Actuator by Changing the Lower Core Angle

Eduard Plavec* · Miroslav Petrinić · Mladen Vidović

Abstract

The aim of almost any electromagnetic actuator development is to increase the electromagnetic force with which an actuator acts on a plunger with as fast a time response as possible while maintaining the dimensions as small as possible. This paper presents research on the impact of the lower core angle on the force and time response of a DC solenoid electromagnetic actuator. The research method is based on the analytical analysis of the magnetic path of the DC solenoid electromagnetic actuator and a comparison with the numerical simulation results. A transient numerical simulation was performed on a 2D axial-symmetric model of the electromagnetic actuator and included simultaneously solving time-dependent partial differential equations of the electromagnetic actuator's magnetic, electrical, and mechanical subsystems. The magnetic subsystem was analyzed by the finite element method (FEM) using the ANSYS Electronics software package. The three prototype models with different lower core angles were produced and tested in the accredited Laboratory Center of KONČAR Electrical Engineering Institute. The obtained measurements are compared with the analytical results and numerical simulation results.

Key Words: DC Electromagnetic Actuator, Force Characteristic, Lower Core Angle, Time Response.

I. Introduction

A solenoid electromagnetic actuator (EMA) is defined as a device through which magnetic energy changes electrical energy into mechanical energy related to almost linear motion or push/pull force [1]. The typical features of EMAs are their compact size, simple structure [2], cheap production, simple activation, ease of control, and high reliability. Due to this, they have become widely used in many different applications.

The design of EMAs starts with the operating conditions of the device. DC EMAs can work in short- or long-term regimes. The most important characteristic for short-term regimes is the shape of the EMA's static characteristic, whereas the temperature rise due to the Joule losses produced by the current is the most common limitation for long-term regimes. DC EMAs usually need to achieve a certain force to overcome the initial force of a mechanism [3]. The aim of almost any EMA development is to increase the electromagnetic force with which an actuator acts on a plunger with as fast a time response as possible while maintaining the dimensions as small as possible. The investigation of plunger shape impact on the electromagnetic force of EMAs was started by Roters, who developed analytical

Manuscript received July 7, 2020 ; Revised October 14, 2020 ; Accepted November 3, 2020. (ID No. 20200707-101J)
Department of Switchgear and Controlgear, KONČAR - Electrical Engineering Institute Inc., Zagreb, Croatia.
*Corresponding Author: Eduard Plavec (e-mail: eduard.plavec@koncar-institut.hr)

force equations for the four main plunger shapes (conical, flat, wedge-shaped and truncated), neglecting the fringing flux and saturation effect [4]. A few more different types of plunger shapes were investigated in [5] using a modeling approach. Plunger shape optimization was conducted using a genetic algorithm-based technique in [1, 6]. A shape optimization of coil and core using a genetic algorithm approach was performed in [7–9]. The coil design parameters based on the magnetic flux leakage were observed in [10]. The speed-increasing method of solenoid EMAs using a non-magnetic ring has been presented in [11]. Since the coils are the main constructional elements of an EMA, the coil parameter selection process is a prerequisite to building an efficient device. The selection of coil parameters in terms of the coil's dimensions and number of turns are investigated in [12]. The impact of the coil winding angle on the force of DC solenoid electromagnetic actuators has been studied in [13]. The shape of the upper core, specifically control cone length and slope, has been investigated in [14]. However, none of these papers investigated the improvement of the electromagnetic force characteristics and time response of DC solenoid EMAs by changing the lower core angle.

This paper presents research on the impact of the lower core angle on the electromagnetic force and time response of a DC solenoid EMA. An analytical analysis of a DC solenoid EMA's magnetic path has been developed. A transient numerical simulation was performed on the 2D axial-symmetric model of the EMA using the ANSYS Maxwell software package. The numerical simulation model includes simultaneously solving time-dependent partial differential equations of the EMA's magnetic, electrical, and mechanical subsystems, whereas its magnetic subsystem is analyzed by FEM. The laboratory testing measurements of EMAs with different lower core angles are compared with the analytical and numerical simulation results.

II. Work Principle and Mathematical Formulation

The general structure of a DC solenoid EMA is shown in Fig. 1. It consists of a coil, plunger, non-magnetic shaft, upper core, non-magnetic ring, spring, lower core, non-magnetic plate, and air gap (Table 1).

A magnetic circuit comprises the lower and upper core, housing, and plunger. The electromagnetic force acting on the plunger is generated in the air gap, the site of energy conversion. The coil provides electrical resistance. The plunger position is initialized by the non-magnetic plate, while the spring returns the plunger to the initial position after activation [9, 13].

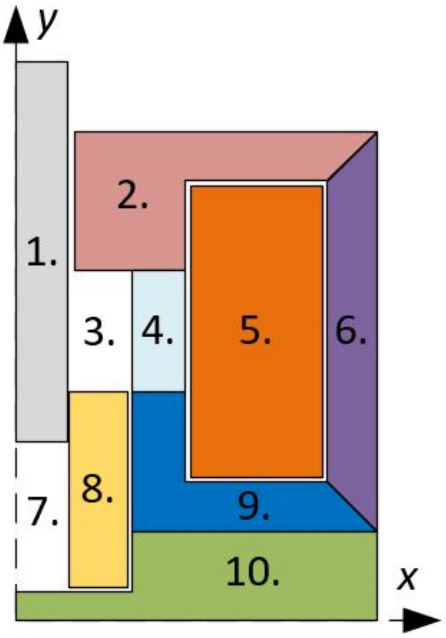

Fig. 1. The 2D axial-symmetric model of a DC solenoid EMA.

Table 1. DC solenoid EMA parts

Label in Fig. 1	Part	Material
1.	Non-magnetic shaft	Stainless steel
2.	Upper core	Pure iron
3.	Air gap	-
4.	Non-magnetic ring	Aluminum
5.	Coil	Copper
6.	Housing	Steel 1010
7.	Spring area	-
8.	Plunger	Pure iron
9.	Lower core	Pure iron
10.	Non-magnetic plate	Stainless steel

The activation response of a DC solenoid EMA consists of three common periods: a sub-transient period, transient period, and stopping period [3]. In the sub-transient period, the excitation voltage is applied, yet there is still no plunger movement. The magnetic flux flows through the magnetic path and builds electromagnetic force. When the electromagnetic force value overcomes the return spring's initial force, the plunger starts to move, and the transient period begins. The plunger movement causes changing magnetic flux in the EMA. Electromotive force, which opposes the voltage source and causes the current to drop, is induced in the coil due to the change in linkage magnetic flux [1]. After the plunger stops its movement, the stopping period begins (the EMF retreats and the current continues to increase).

1. Analytical Model

In this paper, a solenoid EMA is observed as a magnetic circuit, and due to this, it can be described using Ampere's and Hopkinson's laws. If the same current flows through all the turns, Ampere's law can be written as follows [10]:

$$\oint Hdl = \sum_i^N I_i = NI, \tag{1}$$

$$\oint Hdl = \oint \frac{B}{\mu} dl = \oint \frac{\Phi}{\mu S} dl = NI, \tag{2}$$

where H is the magnetic field strength, I_i are the currents flowing in the N windings, B is the magnetic flux density, μ is the permeability of the magnetic material, Φ is the magnetic flux, and S is the area crossed by the magnetic flux. Assuming that all the magnetic flux remains contained inside the EMA, it can be considered as a constant. Since there are two types of materials along the path of integration (magnetic material and air) and considering reluctance, $\Re = \int \frac{dl}{\mu S}$, (2) can be written as:

$$\Phi \left(\int_m \frac{dl_m}{\mu S_m} + \int_a \frac{dl_a}{\mu S_a} \right) = NI, \tag{3}$$

$$\Phi(\Re_m + \Re_a) = NI, \tag{4}$$

where $\Re_m$ is the magnetic material reluctance and $\Re_a$ is the air gap reluctance. The reluctances are represented by the following equations:

$$\Re_m = \frac{l_m}{\mu_0 \mu_r S_m}, \Re_a = \frac{l_a}{\mu_0 S_a}, \tag{5}$$

$$S_m = S_a = S, \tag{6}$$

where l_m is the length of the path along the magnetic material, $\mu_0 = 4\pi \cdot 10^{-7} \frac{H}{m}$ is the magnetic permeability of air, $\mu_r = 160$ is the permeability of the magnetic material, and l_a is the length of the air gap. By combining Eqs. (2) and (5), the magnetic flux density equation is obtained:

$$\Phi \frac{1}{\mu_0 S} \left(\frac{l_m}{\mu_r} + l_a \right) = NI \rightarrow \Phi = \frac{\mu_0 SNI}{\left(\frac{l_m}{\mu_r} + l_a \right)} = BS, \tag{7}$$

$$B = \frac{\mu_0 NI}{\left(\frac{l_m}{\mu_r} + l_a \right)}. \tag{8}$$

From the definition of the Maxwell Stress Tensor and the properties of the Kronecker delta along with the fact that the magnetic field B has only y component (Fig. 1), it is possible to write the electromagnetic force acting on the plunger of the EMA as [15]:

$$\sigma_{yy} = \frac{1}{\mu_0} B_y B_y - \frac{1}{2\mu_0} B^2 \delta_{yy}, \tag{9}$$

$$\sigma_{yy} = \frac{1}{\mu_0} B^2 - \frac{1}{2\mu_0} B^2 = \frac{B^2}{2\mu_0} \rightarrow F = \sigma_{yy} S. \tag{10}$$

By combining Eqs. (8) and (10), the final equation for electromagnetic force (F_e) is obtained:

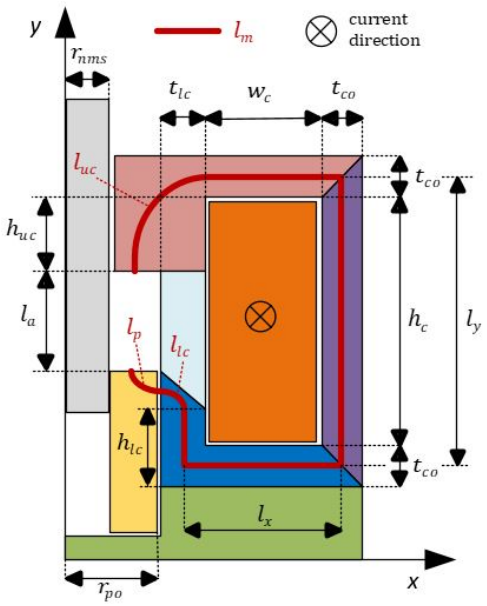

Fig. 2. Design variables overview.

$$F_e = \frac{\mu_0 \mu_r^2 N^2 I^2 S}{2(l_m + \mu_r l_a)^2}. \tag{11}$$

The cross-section area of the plunger can be obtained using the following equation:

$$S = \pi \left(r_{po}^2 - r_{nms}^2 \right), \tag{12}$$

where r_{po} is the plunger's outer radius and r_{nms} is the radius of the non-magnetic shaft. The length of the path along the ferromagnetic material (Fig. 2) is calculated using the following equation:

$$l_m = l_y + l_x + h_{lc} + l_{lc} + l_p + l_{uc} + w_c + \frac{t_{co}}{2} \tag{13}$$

with the following notations: l_x, l_y is the paths along the magnetic material in the x and y direction; h_{lc} is the height of the lower core; l_{lc} is the length of the path along the angled part of the lower core; l_p is the length of the path along the plunger; l_{uc} is the length of the path along the upper core; w_c is the coil width; and t_{co} is the thickness of the core.

The magnetic path length along the angled part of the lower core (l_{lc}) and the magnetic path along the plunger (l_p) are calculated using the expression for ellipse arc length. The equation of the ellipse in the Cartesian coordinate system with the major axis along the x-axis, whose length is $2a$, and with the minor axis along the y-axis, whose length is $2b$, is:

$$b^2 x^2 + a^2 y^2 = a^2 b^2. \tag{14}$$

The expression for computing the arc length of any curve given by the parametric equations ($x = f(t), y = f(t)$) over the range $c \leq t \leq d$ is given as [16]:

$$ds = \int_c^d \sqrt{\left[\left(\frac{dx}{dt}\right)^2 + \left(\frac{dy}{dt}\right)^2\right]} dt. \quad (15)$$

In this case, the range is the first quadrant ($0 \le t \le \pi/2$). The following ellipse parametric equations and their derivations are used:

$$x = a\sin(t), \ \frac{dx}{dt} = a\cos(t), \quad (16)$$

$$y = b\cos(t), \ \frac{dy}{dt} = -b\sin(t), \quad (17)$$

By combining (15) with (16) and (17), the final equation for ellipse arc length in the first quadrant is obtained:

$$ds = \int_0^{\pi/2} \sqrt{[a^2 \cos^2 t + b^2 \sin^2 t]} dt. \quad (18)$$

This can be further rewritten using $\cos^2 t = 1 - \sin^2 t$:

$$ds = \int_0^{\pi/2} \sqrt{\left[1 - \left(\frac{a^2-b^2}{a^2}\right)\sin^2 t\right]} dt, \quad (19)$$

$$ds = \int_0^{\pi/2} \sqrt{[1 - k^2 \sin^2 t]} dt \ . \quad (20)$$

The obtained complete elliptic integral of the second kind is one of those integrals that cannot be expressed in a closed form in terms of the familiar functions of calculus, except if $k = 0$ (circle). For the purpose of analytical calculation of the ferromagnetic path length along the angled lower core, Kepler's approximation is used [16]:

$$ds = \frac{\pi}{4}(a + b). \quad (21)$$

Using the above expression, the length of path along the angled part of the lower core (l_{lc}) and the length of path along the plunger (l_p), both shown in Fig. 3, are calculated:

$$l_{lc} = \frac{\pi}{4}\left(\frac{t_{lc}}{2} + \frac{t_{lc}tg\alpha}{2}\right) = \frac{\pi}{8}(t_{lc} + t_{lc}tg\alpha), \quad (22)$$

$$l_p = \frac{\pi}{8}(r_{po} - r_{nms} + t_{lc}tg\alpha). \quad (23)$$

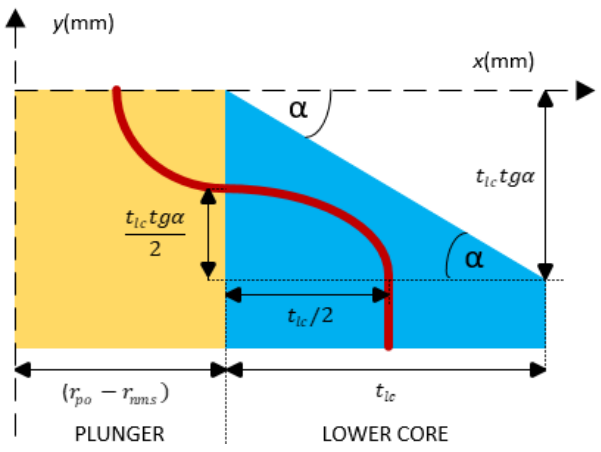

Fig. 3. The plunger and lower core (zoomed detail).

The length of path along the upper core, using (20), is approximated by the following equation (Fig. 2):

$$l_{uc} = \frac{\pi}{8}(2h_{uc} + t_{co} + 2t_{lc} + r_{po} - r_{nms}). \quad (24)$$

When (22), (23), and (24) are put in (13), the total length of the magnetic path through the EMA is obtained by the following equation:

$$l_m = 2w_c + h_c + 2t_{co} + \frac{t_{lc}}{2} + \frac{\pi}{4}\left(\frac{3}{2}t_{lc} + h_{uc} + \frac{t_{co}}{2} + r_{po} - r_{nms} + t_{lc}tg\alpha\right). \quad (25)$$

By combining Eqs. (11) and (25), the final equation for electromagnetic force (F_e) acting on the plunger is obtained.

2. Numerical Model of EMAs

The numerical model of an EMA is represented by three nonlinear systems (magnetic, electrical, and mechanical), which are mutually coupled and solved concurrently. Maxwell's equations are a set of four differential equations that form the theoretical basis of electromagnetism. They describe time- and space-dependent solutions, and they are used to solve the EMA's magnetic subsystem [12]. The vector potential A has only one component, and that scalar function depends on two space variables (r, z) and time (t) when dealing with axially symmetric geometry [1]. The EMA's magnetic subsystem is represented by the following time-dependent differential equation [17]:

$$\frac{\partial}{\partial r}\left(\frac{1}{\mu \cdot r} \cdot \frac{\partial}{\partial r}(rA_\varphi)\right) + \frac{\partial}{\partial z}\left(\frac{1}{\mu} \cdot \frac{\partial A_\varphi}{\partial z}\right) = \frac{N \cdot i}{S_c} - \sigma \frac{\partial A_\varphi}{\partial z} + \sigma v \frac{\partial A_\varphi}{\partial z}, \quad (26)$$

where A_φ is the circular component of the magnetic vector potential, S_c is the cross-section area of coil, σ is the electric conductivity, and v is the plunger velocity. The EMA's electrical subsystem is described by the following equation:

$$u = R\ i + \frac{2\pi \cdot N}{S_c} \int_{S_c} \frac{\partial}{\partial t}(r \cdot A_\varphi)\, dS_c, \quad (27)$$

where u is the applied voltage and R is the coil resistance. The EMA's mechanical subsystem is represented by Newton's second law, whereby the plunger movement is described as follows:

$$m\frac{dv}{dt} + \beta v = F_e - F_l, \quad (28)$$

where m is the plunger mass, β is the damping coefficient, v is the plunger velocity in z direction and F_l is the load force. The plunger velocity in z direction is given as:

$$v = \frac{dz}{dt}. \quad (29)$$

The electromagnetic force calculation was performed in every time step using the magnetic energy change equation [17]:

$$F_e = \frac{dW}{dz} = \frac{\partial}{\partial z}\left[\int_V \left(\int_0^H B dH\right) dV\right], \quad (30)$$

where W is the magnetic energy, H is the magnetic field strength, and V is the volume of the EMA. The electromagnetic calculation was conducted using ANSYS Maxwell and ANSYS Simplorer software (Fig. 4).

III. Simulation Results Analysis

Five different models of solenoid EMA were simulated overall. Plunger shape and mass ($m = 18$ g), applied DC voltage ($U = 220$ V), and coil resistance ($R = 92\ \Omega$) are common to all the simulated models. On the outer edges of all the simulated models, Dirichlet's boundary conditions for the magnetic field ($A_\varphi = 0$), have been applied. This constraint causes the magnetic flux to be tangential at the edges of the model, keeping it within the simulated region. Based on the maximum current that can be interrupted (2.5 A), the coil resistance and the required number of turns have been calculated.

To the modeled motion area containing the plunger, the moving mesh was applied. The mesh size elements should be small enough to prevent significant element deformation, which can have a serious impact on the solution's accuracy due to the magnetic flux density calculation error in the vicinity of the plunger. The variable spring force is modeled as a function of the plunger displacement, to which is added the preload spring force ($F_1 = 0.5$ N), thus making the total load force (F_l):

$$F_l = F_1 + kz, \quad (31)$$

where k is the spring constant and z is the plunger displacement. The total duration of the simulation is set to 10 ms, whereas the simulation time step is set to 0.02 ms. The impact of the lower core angle on the electromagnetic force, inductance, and time response of EMAs was observed at angles of 0°, 20°, 40°, 50°, and 60°. The numerical simulation results of the electromagnetic force dependent on the lower core angle and coil current, as well as inductance and dependency on time, are illustrated in Figs. 5–7 and in Table 2.

The magnetic flux density distribution in EMA at 3.2 ms for lower core angles of 0°, 20°, and 40° is shown in Fig. 8. The plunger velocity and position relative to the plunger starting

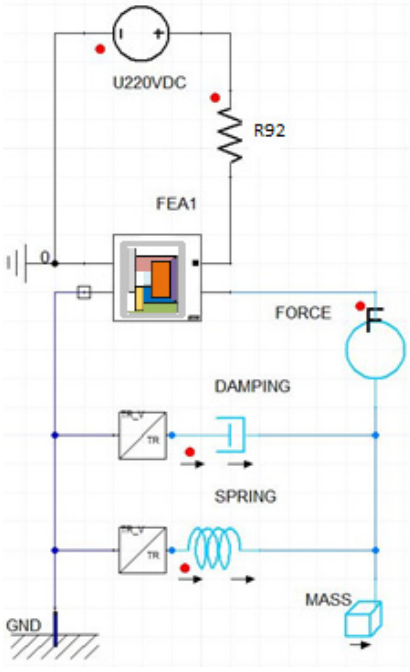

Fig. 4. The model of EMAs in ANSYS Simplorer.

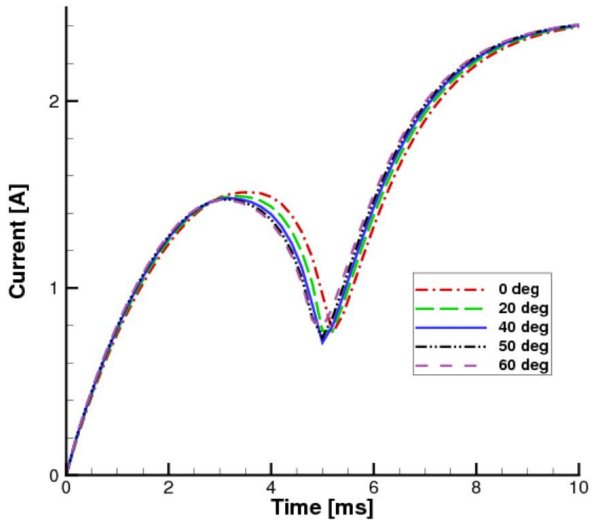

Fig. 5. Numerical simulation results of lower core angle's impact on current.

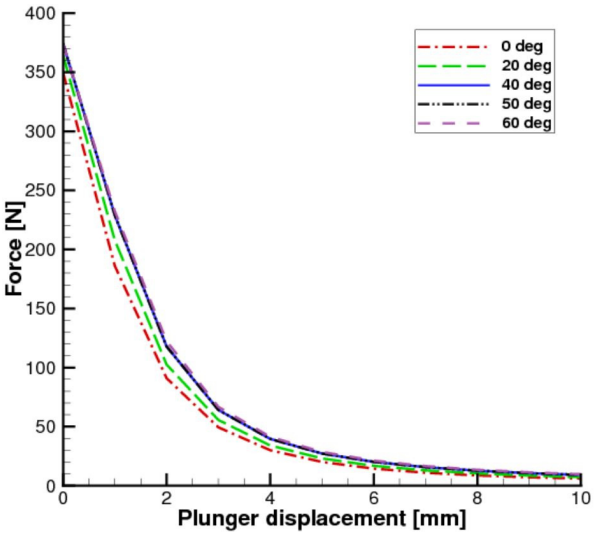

Fig. 6. Numerical simulation results of lower core angle's impact on attraction force.

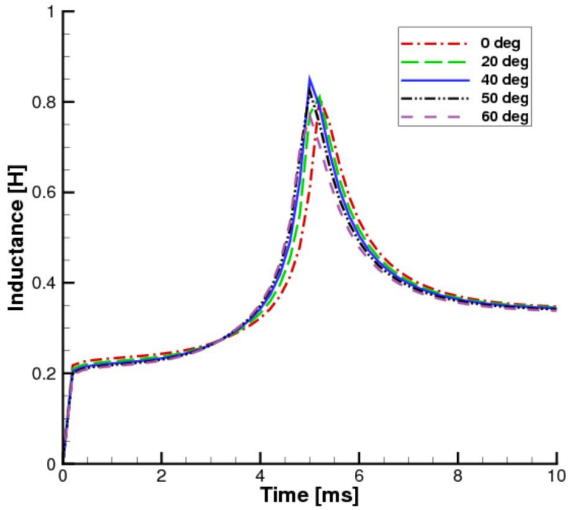

Fig. 7. Numerical simulation results of lower core angle's impact on inductance.

Table 2. Numerical simulation results of lower core angle's impact on EMA characteristics

	0°	20°	40°	50°	60°
Time response (ms)	5.22	5.12	5.04	4.98	4.96
Max force (N)	350	364	374	375	376
Max inductance (H)	0.81	0.82	0.85	0.82	0.77

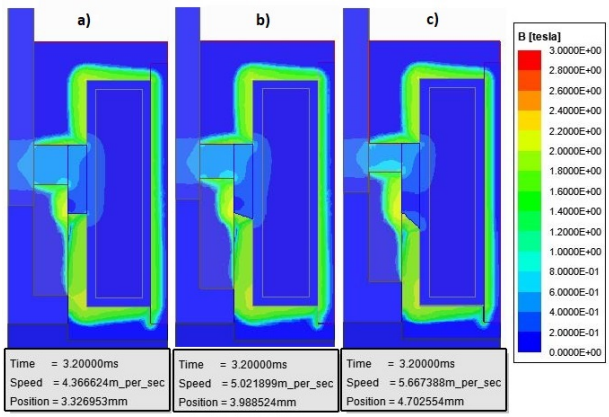

Fig. 8. Magnetic flux density distribution in EMAs at 3.2 ms for lower core angle (α) of (a) 0°, (b) 20°, and (c) 40°.

point are higher if the lower core angle is higher. At 3.2 ms, the lower core with a 40° angle has a velocity of 5.67 m/s and position of 4.7 mm, compared to the flat lower core (0°), which has a velocity of 4.37 m/s and position of 3.33 mm.

IV. Laboratory Testing

A total of three prototype models with lower core angles of 0°, 40°, and 60° were produced. The flat type of plunger was used for testing procedures in all the prototype models. The properties of tested EMAs are given in Table 3, while the design variables are given in Table 4.

The prototype models were tested in the accredited Laboratory Center of KONČAR Electrical Engineering Institute. Coil resistance, current, and electromagnetic force were measured. A standard multimeter, FLUKE 289 IMSK, was used to measure coil resistance. The programmable DC power supply TDK Lambda Genesys 300-11 was used to power EMAs. A National Instruments TR12K transient recorder with a sample rate of 20 MS/s and its acquisition unit were used to measure coil current precisely. The electromagnetic force measurement method was improved compared to [2]. The electromagnetic force acting on the plunger was measured using the universal machine for testing materials: ZwickRoell Z020. To determine the electromagnetic force value, the load cell ZwickRoell Type XForce HP with sensitivity of 2 mV/V, having a linear characteristic for measurement in range from 0 to 500 kg, was used. The load cell has a measurement accuracy of ±2% within this range. Before the force measurement process, the top of the machine extension attached to the load cell was set at a distance of 1 mm from the top of the plunger in its final position. Since the tested prototypes were short-term regime type, the

Table 3. EMA properties

Parameter	Value
Rated power (W)	526
Rated voltage (V)	220
Coil resistance (Ω)	92
Time response (ms)	4.9−5.2
Dimensions (mm)	
Height × Width × Length	41 × 38 × 38

Table 4. EMA design variables

Label	Description	Value
r_{nms}	Non-magnetic shaft radius (mm)	3
r_{po}	Plunger outer radius (mm)	6
t_{co}	Core thickness (mm)	2
w_c	Coil width (mm)	7
h_c	Coil height (mm)	27
l_a	Air gap length (mm)	10
N	Number of turns	1,890
t_{lc}	Lower core thickness (mm)	2
h_{uc}	Upper core height (mm)	8

head velocity of the material testing machine was set to $v_{tm} = 1$ mm/s to prevent the EMAs from overheating during the testing. The load cell moved together with the material testing machine head, reading the electromagnetic force value along with its movement (Fig. 9).

The measurements showed that by changing the lower core angle, the electromagnetic attraction force acting on the plunger could be increased by 7.1%, from the initial 363.35 N to 389.14 N, while at the same time, the EMA's time response is reduced by 2.94%, from 5.11 ms to 4.95 ms (Table 5 and 6, Figs. 10–12).

Fig. 9. The force measurement process.

Table 5. Measurement results of the lower core angle's impact on EMA characteristics

	0°	40°	60°
Time response (ms)	5.11	4.96	4.95
Max force (N)	363.35	388.44	389.14

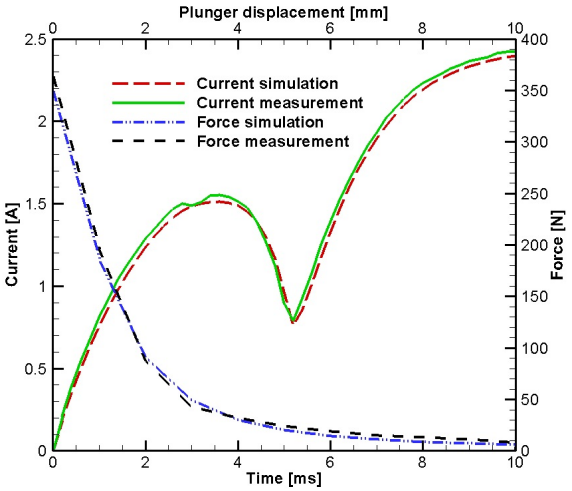

Fig. 10. Measurements and numerical simulation results comparison for angle α = 0°.

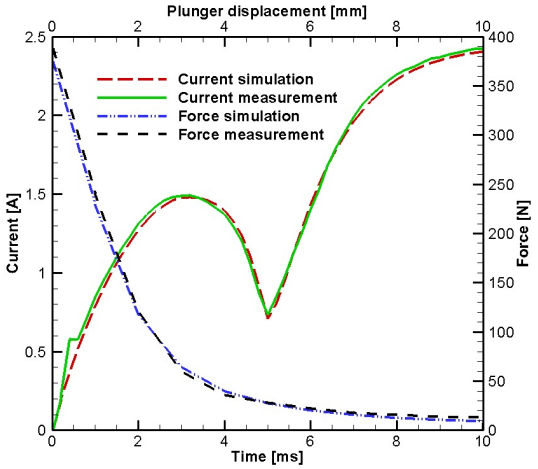

Fig. 11. Measurements and numerical simulation results comparison for angle α = 40°.

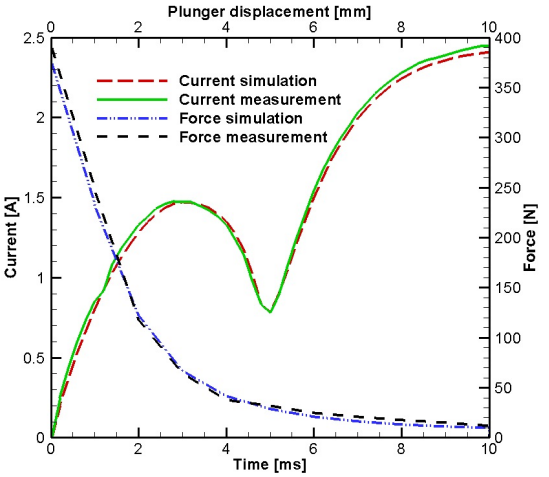

Fig. 12. Measurements and numerical simulation results comparison for angle α = 60°.

V. Results Comparison

Table 6 shows a comparison of measurements, numerical simulation results, and analytical results. The results show that the maximum electromagnetic force of the solenoid EMA increases as the lower core angle increases.

Considering the influence of the lower core angle on the response time of EMA, the numerical simulation results, as well as the analytical and measurement results, reveal that the time response of solenoid EMAs is faster if the lower core angle is higher (Table 6).

The maximum deviation between the simulated and measured values of the electromagnetic force is 3.86% for a lower core angle of 40° (Fig. 13). Concurrently, the maximum deviation between the simulated and measured response time is 1.76% at a lower core angle of 0° (Table 6). The total measurement uncertainty is shown in Fig. 14, and it is ±8%.

Table 6. Comparison of measurement, simulation, and analytical results

		Measured	Simulated	Analytical
α=0°	Max force (N)	363.35	350	393.1
	Time response (ms)	5.11	5.20	-
	Resistance (Ω)	89.81	92	92
α=40°	Max force (N)	388.44	374	418.78
	Time response (ms)	4.96	5.04	-
	Resistance (Ω)	89.69	92	92
α=60°	Max force (N)	389.14	376	424.23
	Time response (ms)	4.95	4.96	-
	Resistance (Ω)	89.90	92	92

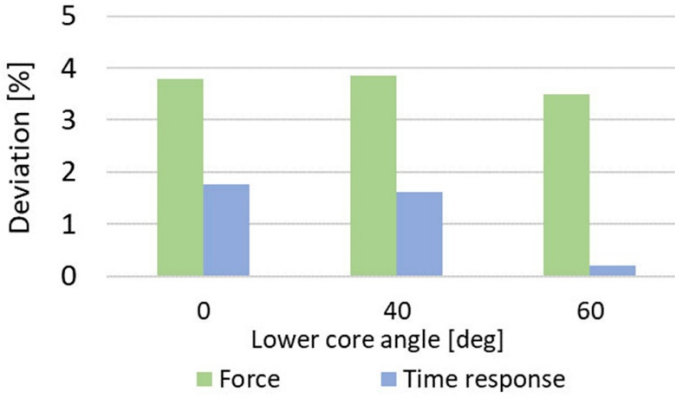

Fig. 13. Deviation between numerical simulation results and measurements.

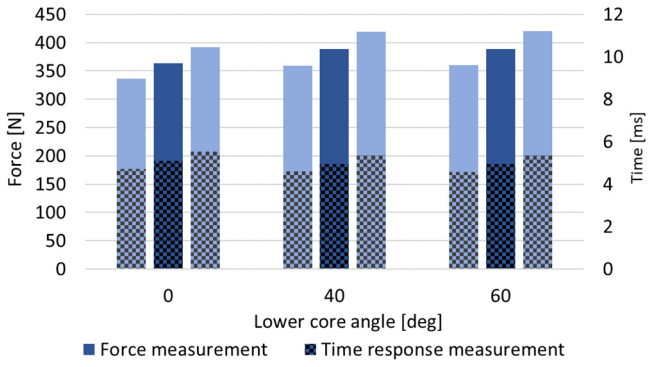

Fig. 14. Measurement uncertainty, ±8%.

VI. Conclusion

The aim of almost any electromagnetic actuator development is to increase the electromagnetic force with which an actuator acts on a plunger with as fast a time response as possible while maintaining the dimensions as small as possible.

This paper has presented research performed on the impact of the lower core angle on the electromagnetic force and response time of a DC solenoid EMA, which is based on a magnetic path analysis. The measurements, numerical simulation results, and analytical results were compared.

Numerical simulation results showed that, by increasing the lower core angle from 0° to 60°, it is possible to increase the maximum electromagnetic force by 7.43% while, at the same time, reducing the response time by 4.6%. The three prototypes with lower core angles of 0°, 40°, and 60° were produced and tested in an accredited Laboratory Center at KONČAR Electrical Engineering Institute.

Measurements were taken of the EMA's electromagnetic force and response time. The maximum deviation between the simulated and measured values of the electromagnetic force was 3.86%, whereas the maximum deviation between the simulated and measured response times was only 1.76%. The analytical method presented yields a maximum deviation of 9.02% compared to the measured values of the electromagnetic force, and therefore, it can be concluded that it is suitable for the rapid calculation of maximum electromagnetic force.

References

[1] E. Plavec and M. Vidovic, "Genetic algorithm based plunger shape optimization of DC solenoid electromagnetic actuator," in *Proceedings of 2016 24th Telecommunications Forum (TELFOR)*, Belgrade, Serbia, 2016, pp. 1-4.

[2] S. Lin and B. Li, "Shift force optimization and trajectory tracking control for a novel gearshift system equipped with electromagnetic linear actuators," *IEEE/ASME Transactions on Mechatronics*, vol. 24, no. 4, pp. 1640-1650, 2019.

[3] E. Plavec, B. Filipovic-Grcic, and M. Vidovic, "The impact of plunger angle and radius on the force and time response of DC solenoid electromagnetic actuator used in high-voltage circuit breaker," *International Journal of Electrical Power & Energy Systems*, vol. 118, article no. 105767, 2020. https://doi.org/10.1016/j.ijepes.2019.105767.

[4] H. C. Roters, *Electromagnetic Devices*. New York, NY: Wiley, 1941.

[5] D. Cvetkovic, I. Cosic, and A. Subic, "Improved performance of the electromagnetic fuel injector solenoid actuator using a modelling approach," *International Journal of Applied Electromagnetics and Mechanics*, vol. 27, no. 4, pp. 251-273, 2008.

[6] F. Mach, I. Novy, P. Karban, and I. Dolezel, "Shape optimization of electromagnetic actuators," in *Proceedings of 2014 ELEKTRO*, Rajecke Teplice, Slovakia, 2014, pp. 595-598.

[7] S. H. Lee, H. C. Yi, K. Han, and J. H. Kim, "Genetic algorithm-based design optimization of electromagnetic

valve actuators in combustion engines," *Energies*, vol. 8, no. 11, pp. 13222-13230, 2015.

[8] S. B. Yoon, J. Hur, Y. D. Chun, and D. S. Hyun, "Shape optimization of solenoid actuator using the finite element method and numerical optimization technique," *IEEE Transactions on Magnetics*, vol. 33, no. 5, pp. 4140-4142, 1997.

[9] E. Plavec, I. Uglesic, and M. Vidovic, "Genetic algorithm based shape optimization method of DC solenoid electromagnetic actuator," *Applied Computational Electromagnetics Society Journal*, vol. 33, no. 3, pp. 325-334, 2018.

[10] W. Zhang, Y. B. Shi, and Y. J. Li, "Magnetic coil parameters design of oil casing damage detector based on magnetic flux leakage," in *Proceedings of 2011 International Conference on Applied Superconductivity and Electromagnetic Devices*, Sydney, Australia, 2011, pp. 50-53.

[11] B. J. Sung and E. W. Lee, "Optimal design and speed increasing method of solenoid actuator using a non-magnetic ring," in *Proceedings of 2005 International Conference on Power Electronics and Drives Systems*, Kuala Lumpur, Malaysia, 2005, pp. 1140-1145.

[12] Z. Gosiewski and M. Kondratiuk, "Selection of coils parameters in magnetic launchers," *Solid State Phenomena*, vol. 147-149, pp. 438-443, 2009.

[13] E. Plavec, I. Ladisic, and M. Vidovic, "The impact of coil winding angle on the force of DC solenoid electromagnetic actuator," *Advances in Electrical and Electronic Engineering*, vol. 17, no. 3, pp. 244-250, 2019.

[14] S. N. Yun, Y. B. Ham, and J. H. Park, "New approach to design control cone for electro-magnetic proportional solenoid actuator," in *Proceedings of 2012 IEEE/ASME International Conference on Advanced Intelligent Mechatronics (AIM)*, Kaohsiung, Taiwan, 2012, pp. 982-987.

[15] D. Righetti, *Solenoid Actuators: Theory and Computational Methods*. Rome, Italy: Youcanprint, 2017.

[16] T. R. Chandrupatla and T. J. Osler, "The perimeter of an ellipse," *Mathematical Scientist*, vol. 35, no. 2, pp. 122-131, 2010.

[17] ANSYS Inc., "Introduction to ANSYS Maxwell 17.0 Release," 2016 [Online]. Available: https://studylib.net/doc/25201551/maxwell-intro-17.0-m01-basics.

Eduard Plavec

was born in 1988 in Zagreb, Croatia. He received a Ph.D. degree in electrical engineering and computing from the University of Zagreb, Faculty of Electrical Engineering and Computing, in 2018. He joined KONČAR Electrical Engineering Institute in 2014. Currently, he is the head of the Research and Development section in the Switchgear and Controlgear Department. His areas of interest include computational electromagnetics and high-voltage engineering. He is a member of CIGRÉ study committee A3—Transmission and Distribution Equipment, an IEEE member since 2012, and an ACES member since 2016.

Miroslav Petrinić

was born in Zagreb, Croatia, in 1983. He received a B.Sc. degree in 2007 at the University of Zagreb, Faculty of Electrical Engineering and Computing, where he also received his Ph.D. degree in Electric Machines, Drives and Automation in 2019. Since 2007, he has been employed at KONČAR Electrical Engineering Institute, Inc. in Zagreb. There he works as an R&D engineer in the field of electromagnetism. His scientific research activities are aimed at the analysis and development of electromagnetic devices. He is a coauthor of several papers published in proceedings of scientific and expert conferences and gatherings in the country and abroad. He is a member of the HRO CIGRÉ A1 committee for rotating machines.

Mladen Vidović

was born in Zagreb, Croatia. He received a B.Eng. degree from the University of Zagreb, Faculty of Electrical Engineering in 1984. He has worked at KONČAR Electrical Engineering Institute since 1986 in the Switchgear and Controlgear Department, where he is currently the Head of Research and Development. His areas of interest are design and diagnostics of high-voltage switchgears and development of online monitoring systems of high-voltage apparatuses. He is the author of several papers and patents.

JOURNAL OF ELECTROMAGNETIC ENGINEERING AND SCIENCE, VOL. 21, NO. 2, 104~110, APR. 2021

https://doi.org/10.26866/jees.2021.21.2.104
ISSN 2671-7263 (Online) · ISSN 2671-7255 (Print)

An Improved Radiative Transfer Model for Polarimetric Backscattering from Agricultural Fields at C- and X-Bands

Yisok Oh[1,*] · Jisung Geba Chang[2] · Maxim Shoshany[2]

Abstract

The first-order vector radiative transfer model (FVRTM) is modified mainly by examining the effects of leaf curvature of vegetation canopies, the higher-order multiple scattering among vegetation scattering particles, and the underlying-surface roughness for forward reflection on radar backscattering from farming fields at C- and X-bands. At first, we collected the backscattering coefficients measured by scatterometers and space-borne synthetic aperture radar (SAR), field-measured ground-truth data sets, and theoretical scattering models for radar backscattering from vegetation fields at microwaves. Then, these effects on the RTM were examined using the database at the C- and X-bands. Finally, an improved RTM was obtained by adjusting its parameters, mainly related with the leaf curvature, the higher-order multiple scattering, and the underlying-surface small-roughness characteristics, and its accuracy was verified by comparisons between the improved RTM and measurement data sets.

Key Words: Backscattering Coefficient, Leaf Curvature, Multiple Scattering, Radiative Transfer Model, Surface Roughness.

I. Introduction

Microwave remote sensing of Earth's terrain using satellite synthetic aperture radar (SAR) provides us valuable information nowadays. There are many SARs at C- and X-bands, such as SENTINEL-1(A and B) and RADARSAT-2 at the C-band and TerraSAR-X/TanDEM-X, COSMO-SkyMed(1, 2, 3, 4), and KOMPSAT-5 at the X-band. Therefore, in this study we focused on the C- and X-bands, and also on farming fields and rangelands that microwaves at C- and X-bands can penetrate through their vegetation canopies.

The radiative transfer (RT) technique has been widely used for microwave backscattering from vegetation fields [1, 2]. The radiative transfer model (RTM) has a relatively good accuracy for estimating the backscattering coefficients for a wide range of vegetation canopies [3, 4]. In the RTM, the phase matrix should be accurately calculated for a scattering particle with given incident, scattered, and orientation angles in elevation and azimuthal directions ($\theta_i, \phi_i;\ \theta_s, \phi_s;\ \theta_p, \phi_p$) as well as the size of the particles relative to the wavelength [1].

The phase matrix is obtained from a scattering matrix [S] that is calculated assuming that a leaf is a dielectric lossy flat

Manuscript received July 23, 2020 ; Revised October 20, 2020 ; Accepted November 3, 2020. (ID No. 20200723-106J)
[1]School of Electronic and Electrical Engineering, Hongik University, Seoul, Korea.
[2]Faculty of Civil & Environmental Engineering, Technion - Israel Institute of Technology, Haifa, Israel.
[*]Corresponding Author: Yisok Oh (e-mail: yisokoh@hongik.ac.kr)

rectangular or circular plate. The RTM may need to be examined further in terms of the effect of the curvature of a leaf on the radar backscatter to be more practical for applying this model to the determination of the backscattering coefficients of vegetation canopies. The effect of curvature on the radar backscatter is quite large for backscattering from a curved dielectric sheet at C- and X-band frequencies [5, 6]. Therefore, we may need to examine in detail the effect of the leaf curvature on the RTM.

The first-order vector RTM does not include the higher-order multiple scattering among scattering particles in a vegetation canopy. The cross-polarized backscattering coefficient (σ_{vh}^0 or σ_{hv}^0) of a vegetation field is much more sensitive to the multiple/volume scattering from a vegetation canopy than the co-polarized backscattering coefficients (σ_{hh}^0 and σ_{vv}^0), and consequently, σ_{vh}^0 is used for calculating the radar vegetation index (RVI) or polarimetric radar vegetation index (PRVI) [7]. It was also shown with a numerical calculation that the cross-polarized backscattering coefficient is very sensitive to the higher-order multiple scattering, whereas the co-polarized coefficients are not [8]. Therefore, the reexamination of the multiple-scattering effect on the RTM might be crucial, especially for the cross-polarized backscattering coefficients of vegetation fields.

Although the backscattering from a bare soil surface can be accurately computed with theoretical and empirical models such as the integral equation method (IEM) [9] and polarimetric radar inversion for soil moisture (PRISM) [10], the reflection from a rough soil surface needs to be examined in more detail, because the microwave interaction between the vegetation canopy and the underlying soil surface mainly depends on the soil-surface roughness in addition to the soil moisture. We may need to redefine the surface roughness for microwave reflection in a different scale (small roughness) in comparison with the surface roughness for microwave backscattering (large roughness).

In this paper, we first examine the RTM for the effect of the leaf curvature in a vegetation canopy, the multiple-scattering effect for *vv*-, *hh*-, and *vh*- (*hv*-) polarization combinations, and the effect of the surface roughness on the reflection coefficient of an underlying soil surface. Then, the RTM is modified with the optimized input parameters in relation with the leaf curvature, the higher-order multiple scattering, and the small roughness of underlying surface. Finally, the accuracy of the modified RTM is verified by comparing it with experimental data sets.

II. Examination of RTM

The first-order RTM is a well-known theoretical model for radar backscattering from a vegetation canopy over an underlying soil surface, especially for range and farming fields, as shown in Fig. 1. In general, the RTM includes five scattering mechanisms:

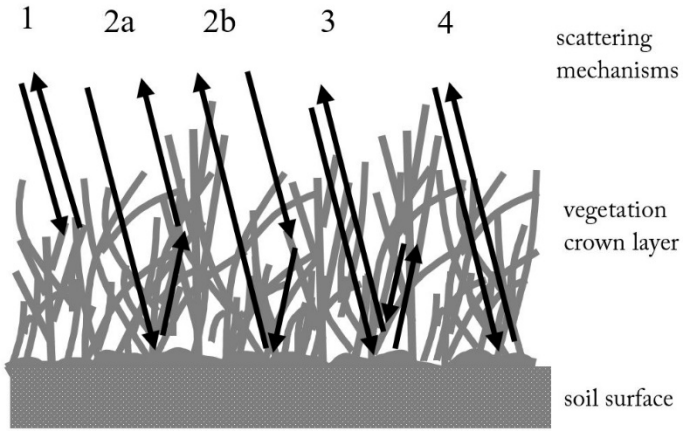

Fig. 1. Scattering mechanisms in FVRTM model.

(1) the direct backscatter from the vegetation layer,
(4) the direct backscatter from the underlying soil surface with the attenuation through the vegetation layer, and
(2)–(3) the interactions between the vegetation layer and the underlying soil surface: i.e.,
(2a) incidence – reflection from the ground – forward scattering from the vegetation layer – backscatter,
(2b) incidence – forward scattering from the vegetation layer – reflection from the ground – backscatter, and
(3) incidence – reflection from the ground –backscattering from the vegetation layer – reflection from the ground – backscatter.

Then the backscattering coefficient of a vegetated surface can be computed by the following summation of the five scattering mechanisms:

$$\sigma_{pq}^o = \sigma_v^o + \sigma_{gv}^o + \sigma_{vg}^o + \sigma_{gvg}^o + \sigma_g^o, \tag{1}$$

where the first four terms can be formulated with scattering matrices of vegetation particles such as lossy dielectric disks for leaves and lossy dielectric cylinders for stems and branches [1–3]. The last term of Eq. (1) can be obtained from a theoretical or empirical model for microwave backscattering from soil surfaces [9, 10].

Eq. (1) can be explicitly expressed in the following form:

$$\sigma_{pq}^o = 4\pi \cos\theta_0 \, T_{mn}, \tag{2}$$

where p or q denotes v- or h-polarization, m or n is 1 or 2, and *vv*-, *vh*-, *hv*-, and *hh*-polarizations correspond to 11, 12, 21, and 22 elements of the 4×4 transformation matrix $\bar{\bar{T}}$ that can be computed with the following matrix multiplications with the canopy scattering matrix $\bar{\bar{A}}$, the eigen matrix $\bar{\bar{E}}$, the diagonal extinction matrix $\bar{\bar{D}}$, the reflectivity matrix $\bar{\bar{R}}$, the Stokes scattering operator matrix $\bar{\bar{M}}$, and the phase matrix $\bar{\bar{P}}$ [1, 5].

$$\bar{\bar{T}} = \sum_{k=1}^{5} sec\theta_0 \bar{\bar{T}}_k$$

with

$$\bar{\bar{T}}_1 = \bar{\bar{E}}_4\ \bar{\bar{A}}_{41}\ \bar{\bar{E}}_1^{-1}$$
$$\bar{\bar{T}}_2 = \bar{\bar{E}}_4\ \bar{\bar{A}}_{42}\ \bar{\bar{E}}_2^{-1}\bar{\bar{R}}\ \{\bar{\bar{E}}_1\bar{\bar{D}}_1\bar{\bar{E}}_1^{-1}\}$$
$$\bar{\bar{T}}_3 = \{\bar{\bar{E}}_4\bar{\bar{D}}_4\bar{\bar{E}}_4^{-1}\}\bar{\bar{R}}\ \bar{\bar{E}}_3\ \bar{\bar{A}}_{31}\ \bar{\bar{E}}_1^{-1}$$
$$\bar{\bar{T}}_4 = \{\bar{\bar{E}}_4\bar{\bar{D}}_4\bar{\bar{E}}_4^{-1}\}\bar{\bar{R}}\ \bar{\bar{E}}_3\ \bar{\bar{A}}_{32}\ \bar{\bar{E}}_2^{-1}\bar{\bar{R}}\ \{\bar{\bar{E}}_1\bar{\bar{D}}_1\bar{\bar{E}}_1^{-1}\}$$
$$\bar{\bar{T}}_5 = \{\bar{\bar{E}}_4\bar{\bar{D}}_4\bar{\bar{E}}_4^{-1}\}\bar{\bar{M}}\{\bar{\bar{E}}_1\bar{\bar{D}}_1\bar{\bar{E}}_1^{-1}\}, \quad (3)$$

where $[\bar{\bar{A}}_{kl}]_{ij} = [\bar{\bar{E}}_k^{-1}\bar{\bar{P}}_{kl}\bar{\bar{E}}_l]_{ij}\ C_{kl,ij}$ [4].

The subscripts k = 1, 2, 3, 4, and 5 of the transformation matrix $\bar{\bar{T}}_k$ correspond to the scattering mechanisms 1, 2a, 2b, 3, and 4, respectively, in Fig. 1. The subscripts 1, 2, 3, and 4 of other matrices indicate the scattering or incident directions (↘), (↗), (↙), and (↖), respectively. The 4×4 phase matrix $\bar{\bar{P}}$ can be computed from the 2×2 scattering matrices $\bar{\bar{S}}$ of scattering particles, and the constant $C_{kl,ij}$ can be obtained using the averaged scattering matrices $\langle\bar{\bar{S}}\rangle$, for the ij^{th} elements of the matrices. The Stokes scattering operator matrix $\bar{\bar{M}}$ can be computed from a polarimetric theoretical or empirical surface scattering model for backscattering coefficients, such as the IEM model and the PRISM model [2].

1. Effect of Leaf Curvature

There are various shapes and sizes of leaves in rangelands and farming fields, such as blade-type and disk-type lossy dielectric leaves. Those natural and agricultural leaves usually have curved shapes and/or irregular surfaces. The reduction of radar cross section (RCS σ) of a curved dielectric sheet can be analytically computed accurately by multiplying a curve factor to the scattering matrix of a flat dielectric disk, using a Fresnel integral with the argument of leaf length a and the radius of curvature ρ for a given frequency [6].

$$S_c = S_{fp}\ F(\gamma)/\gamma, \quad \text{with } \gamma = \frac{a}{2}\sqrt{\frac{k_0}{\rho}}, \quad (4)$$

where S_c is the scattering matrix element for a curved lossy dielectric sheet, S_{fp} is the scattering matrix element for a flat plate, $F(\gamma)$ is the Fresnel integral with an argument γ, and k_0 is the wavenumber. For example, the reductions of RCS at normal incidence are about 0.98, 0.75, and 0.4 in magnitude for L-, C-, and X-bands, respectively, when both the curvature radius and leaf length are 6 cm. The RCS reductions are 0.95, 0.75, and 0.32 for the curvature radii of 12, 6, and 3 cm, respectively, with a fixed leaf length of 6 cm at the C-band [6]. Therefore, we need to multiply a multiplicative factor, i.e., the "curve factor" C_{factor}, to the scattering matrices for leaves and stems to compensate for the RCS reduction because of the leaf-curvature effect in the RTM.

$$C_{factor} \equiv \langle\frac{S_c}{S_{fp}}\rangle = \langle F(\gamma)/\gamma\rangle, \quad (5)$$

$$[S]_m = C_{factor}\ [S], \quad (6)$$

where $[S]_m$ is the modified scattering matrix of a leaf or a branch.

The curve factor may also cover the RCS reduction that would be caused by the irregularity deviating from the flatness of a leaf.

2. Effect of Multiple Scattering

The RTM does not include the higher-order multiple scattering as shown in Fig. 1, whereas the actual microwave backscatter will include the higher-order multiple scattering inside the vegetation layer and between the vegetation layer and the underlying ground surface. A full-wave analysis by the moment method for a relatively sparse vegetation field revealed that the effect of multiple scattering is negligible for co-polarization, whereas the cross-polarized backscattering coefficients are significantly influenced by the effect of multiple scattering [8]. For example, the difference between a full-wave analysis that includes all orders of multiple scattering and a theoretical model that includes only single scattering is about 9 dB for *hv*-polarization and less than 0.5 dB for *hh*-polarization for a sample vegetation canopy with only ten 2λ-length stems on a 2λ-diameter underlying surface [8]. The fully phase-coherent computation [11] for the backscattering coefficients of grasslands also showed that the higher-order scattering terms should be added to fit the radar measurements for the cross-polarized data [12].

The effect of multiple scattering can be accounted by multiplying a factor, the so-called "multiple factor" M_{factor}, to the transformation matrix elements for the higher-order multiple scattering from scatters in a vegetation layer.

$$[T]_{km} = M_{factor,k}[T]_k, \quad (7)$$

where $[T]_{km}$ is the modified k^{th} transformation matrix, and the multiple factor may be obtained from an extensive database of experimental measurements.

3. Effect of Surface Roughness

For the backscattering from an underlying soil surface, the microwave radiates from an antenna of a radar far from the rough surface. Therefore, the surface roughness should be considered for the whole antenna footprint that provides a large-scale roughness. However, for the reflection from the underlying soil surface in the scattering mechanisms 2a, 2b, and 3 in Fig. 1, the scattering particles are positioned near the surface. Therefore, the area of reflection might be small, which provides a small roughness. The retrieval of the RMS height depends on the length of the surface profile, and the measured RMS height rapidly decreases with a decrease in the profile length of the surface [13, 14]. Therefore, the use of large-scale roughness pa-

rameters for mechanism 4 and small-scale roughness parameters for mechanisms 2a, 2b, and 3 can be recommended.

The effect of small roughness would be implemented with the decrease in the RMS height for the computation of the microwave reflection, such as $h_{RMS-s} =$ roughness factor $(R_{factor}) \times h_{RMS}$, where h_{RMS-s} is the small-roughness RMS height for reflection, and h_{RMS} is the RMS height for backscattering from the soil surface. For the reflection from a rough surface, the following form of the reflection coefficient is used for the reflectivity matrix.

$$[R]_m = R_{mult}\ [R], \tag{8}$$

where $[R]_m$ is the modified reflectivity matrix, and

$$R_{mult} = \left[\frac{\Gamma_{sp}}{\Gamma_{fp}}\right]^2 = [exp[-X]\ I_0[X]]^2 \tag{9}$$

with $X = 2(kh_{RMS-s}\cos\theta)^2$, where Γ_{sp} is the reflection coefficient of a rough soil surface, Γ_{fp} is the Fresnel reflection coefficient of a flat plane, the subscript p is the polarization, θ is the incidence angle, and $I_0[\cdots]$ is the modified first-kind Bessel function.

III. Modification and Verification of RTM

The parameters of the RTM with regard to the effects of the leaf curvature, multiple scattering, and small roughness can be determined on the basis of comparisons between the measurements and the RTM. There are numerous data sets for radar backscattering coefficients of vegetation fields at the C- and X-bands. However, it is difficult to find the ground-truth data sets that include all input parameters of the RTM, such as the water contents of leaves and stems, the root-mean-square (RMS) height of the underlying soil surface, the volumetric soil moisture content, the height of the vegetation-crown layer, and the averages and standard deviations of leaf length, leaf width, leaf density, leaf thickness, leaf vertical and horizontal angles, stem length, stem diameter, stem density, and stem vertical and horizontal angles. Therefore, we collected the ground-truth data in relation with the input parameters of the RTM as well as polarimetric scatterometer measurement data sets.

1. Experimental Data Sets

The Hongik polarimetric scatterometer (HPS) was used to acquire the full-polarimetric backscattering coefficients of vegetation fields to closely examine the RTM. The backscattering coefficients of a cornfield in Suwon, Korea, were acquired at the C-band and five different incidence angles (20°, 30°, 40°, 50°, and 60°) from May 29 to July 11, 2013, covering a whole growing season. The HPS is a vector-network-analyzer-based full-polarimetric L-, C-, and X-band scatterometer, and it is calibrated by the differential Mueller matrix calibration technique (DMMCT) [15] with a single calibration target, namely, a trihedral corner reflector. The backscattering coefficients of a bean field in Suwon, Korea, were also collected by the COSMO-SkyMed SAR at the X-band at 40° for *hh*-polarization during the bean growth cycle from July 22 to September 24, 2010.

We also collected *in situ* measured ground-truth data for all the input parameters of the RTM on the same days when the radar data were collected. The parameters for vegetation fields were obtained by sampling. The surface roughness parameters such as the RMS height were obtained from surface profiles that were measured with a laser profilometer and a pin profilometer. The leaf-area index (LAI) values were acquired using AccuPAR LP-80 of Decagon Devices Inc., and the soil moisture contents were measured using EC-5 of the same company.

2. Determination of Parameters

By minimizing the root-mean-square error (RMSE) between the RTM and the scatterometer measurements of a cornfield at the C-band, we can obtain optimum curve, multiple, and roughness factors. It was found that the optimized curve factors for considering the effect of leaf curvatures are about 0.7 for leaves and 1.0 for stems at the C-band for scattering from cornfields. The curve factor depends on frequency (or wavelength) [6], and the curve factor becomes about 0.5 for leaves and 0.7 for branches (stems) at the X-band for scattering from soybean fields.

The co-polarized backscattering coefficients that were measured from vegetation fields agree well with the RTM, and consequently, the multiple factor is about 1.0 at *vv*- and *hh*-polarizations as determined by the RMSE technique while considering the effect of multiple scattering, which means that the first-order multiple scattering is dominant for the co-polarized backscattering coefficients. However, the RMSE technique provides about 50 for the cross-polarized scattering from the corn fields.

The RMSE technique leads us to the rough factor of about 0.7. The effect of the rough factor is negligible for very sparse and very dense vegetation canopies, because the interaction between the vegetation canopy and the underlying surface in these cases is negligible.

3. Verification

The RTM is modified with the induced parameters from the effects of the leaf curvature, multiple scattering, and small roughness for the reflection, and its accuracy is examined by comparisons between the modified RTM and the scatterometer measurements. Fig. 2 shows the comparison among the scatterometer measurements on May 29, the traditional RTM ("Old Model"), and the new RTM modified with the "curve factor," "multiple factor," and "roughness factor" as explained in

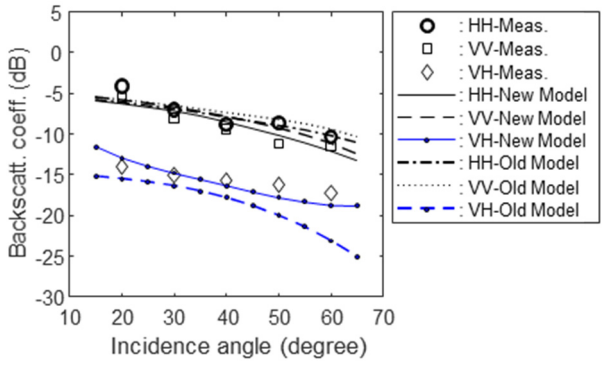

Fig. 2. Comparison among HPS measurements on May 29, 2013, traditional RTM, and modified RTM for *vv*-, *hh*-, and *vh*-polarizations.

the previous section, and with *in situ* field-measured 21 input parameters, for multi-polarized backscattering coefficients of the cornfield. The early-stage cornfield on May 29, 2013 was a sparse vegetation field with a plant height of 30 cm and an LAI of 0.48. The backscattering from the underlying soil surface would be dominant in this case. Therefore, the improvement of the modified RTM is minimal for co-polarized backscattering coefficients. However, the cross-polarized backscattering coefficient of the modified RTM is remarkably improved, such as 2.2 dB at 50° and 4.4 dB at 60° as shown in Fig. 2.

Fig. 3 shows the comparison among the scatterometer measurements on July 11, 2013, the traditional RTM, and the modified RTM for the multi-polarimetric data. The full-grown cornfield on July 11 was a dense vegetation field with a plant height of 250 cm and an LAI of 2.62. Fig. 3 shows that the traditional RTM provided about 2–3 dB higher co-polarized backscattering coefficient than the radar measurements without correction for the effect of leaf curvature, whereas the modified model and the measurements agree quite well for the co-polarized backscattering coefficients. The improvement of the cross-polarized backscattering coefficients with the modification for the higher-order multiple scattering is very large as shown in Fig. 3 and Table 1, especially for higher incidence angles, because of (1) the vertical structures of the corn-plant stems and (2) the effective depth increase at higher incidence angles. The discrepancy between the measurements and the modified RTM for *vh*-polarization at low incidence angles, especially 20° and 30°, may be from the fact that the RTM inherently does not include the shape and location of the full-grown leaves.

Table 1. Comparison of RMS deviations

	RMS deviation (dB)					
	Fig. 2			Fig. 3		
	Old	New	Δ	Old	New	Δ
VV	1.94	1.28	0.66	3.72	0.95	2.77
HH	1.01	1.39	−0.38	2.89	0.74	2.15
VH	3.39	1.13	2.26	7.88	2.70	5.18

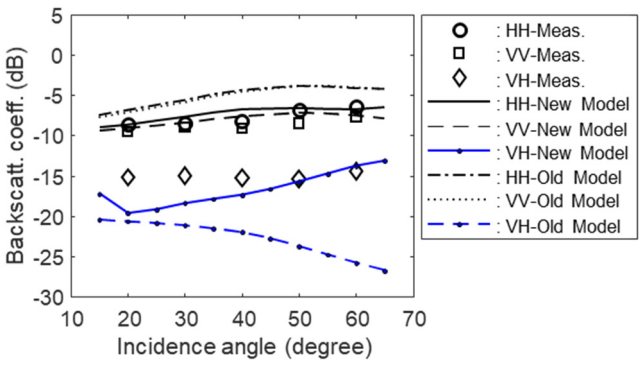

Fig. 3. Comparison between HPS measurements on July 11, 2003, traditional RTM, and modified RTM for multi-polarized data.

The modified RTM is also compared with the COSMO-SkyMed data at the X-band, which were acquired from a bean field in Suwon, Korea, at 40° for *hh*-polarization during the bean growth cycle from July to October 2010. The ground-truth data were also collected *in situ* during the period for about two dozens of input parameters of the RTM. The LAIs of the bean fields were 0.73, 2.42, 3.21, 3.36, and 4.54 for 22, 37, 53, 70, and 86 days after planting, respectively. Fig. 4 shows the comparison between the COSMO-SkyMed data and the modified RTM for the bean field in a growing season. In this comparison, we used a curve factor of 0.5 for leaves and a curve factor of 0.7 for branches and stems, which are lower than the factors at the C-band, because the RCS reduction increases as frequency increases.

There are no changes in the multiple and rough factors: i.e., a multiple factor of 1.0 for *hh*-polarization and a rough factor of 0.7 for the small-roughness effect.

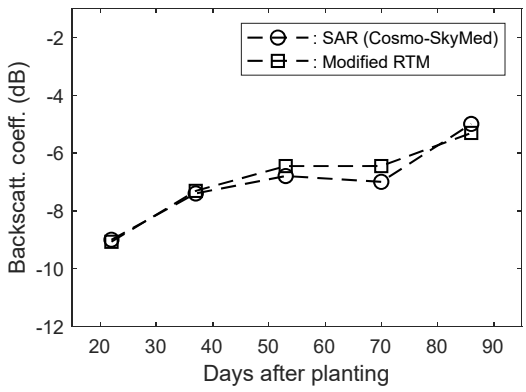

Fig. 4. Comparison between COSMO-SkyMed data and modified RTM for a bean field for X-band *hh*-polarized backscattering coefficients at various days after planting.

IV. Concluding Remarks

First, a modified RTM was formulated for estimating the backscattering coefficients of one-layered vegetation fields, and the model was modified on the basis of the HPS measurements and *in situ* measured ground-truth data for typical agricultural canopies. The modified RTM was multiplied by two multiplicative factors: (1) one is the curvature factor for the curvature effect of leaves and branches (or stems) for all polarizations and (2) the other is the multiple-scattering factor for the cross-polarized backscattering because the cross-polarized backscattering coefficient is very sensitive to the higher-order multiple scattering. In addition to the aforementioned two multiplicative parameters, the small-roughness parameter for microwave reflection from the underlying soil surface was also introduced.

The authors would like to thank J. H. Hwang of Seoul National University and S. K. Kweon and S. M. Park of LIGNex1 Co. for providing their valuable measurement data. The authors also thank the anonymous reviewers for their thoughtful comments. This work was supported by the NRF of Korea (2016R1D1A1A09918412).

References

[1] L. Tsang, J. A. Kong, and R. T. Shin, *Theory of Microwave Remote Sensing*, 1st ed. Hoboken, NJ: Wiley, 1985.

[2] F. T. Ulaby and D. G. Long, *Microwave Radar and Radiometric Remote Sensing*. Norwood, MA: Artech House, 2014 .

[3] F. T. Ulaby, K. Sarabandi, K. McDonald, M. Whit, and M. C. Dobson, "Michigan microwave canopy scattering model," *International Journal of Remote Sensing*, vol. 11, no. 7, pp. 1223–1253, 1990.

[4] Y. Oh, S. Y. Hong, Y. Kim, J. Y. Hong, and Y. H. Kim, "Polarimetric backscattering coefficients of flooded rice fields at L- and C-bands: measurements, modeling, data analysis," *IEEE Transactions on Geoscience and Remote Sensing*, vol. 47, no. 8, pp. 2714–2721, 2009.

[5] F. T. Ulaby and C. Elachi, *Radar Polarimetry for Geoscience Applications*. Norwood, MA: Artech House, 1990.

[6] K. Sarabandi, T. B. Senior, and F. T. Ulaby, "Effect of curvature on the backscattering from a leaf," *Journal of Electromagnetic Waves and Applications*, vol. 2, no. 7, pp. 653–670, 1988.

[7] J. G. Chang, M. Shoshany, and Y. Oh, "Polarimetric radar vegetation index for biomass estimation in desert fringe ecosystems," *IEEE Transactions on Geoscience and Remote Sensing*, vol. 56, no. 12, pp. 7012–7018, 2018.

[8] Y. Oh, Y. M. Jang, and K. Sarabandi, "Full-wave analysis of microwave scattering from short vegetation: an investigation on the effect of multiple scattering," *IEEE Transactions on Geoscience and Remote Sensing*, vol. 40, no. 11, pp. 2522–2526, 2002.

[9] A. K. Fung, Z. Li, and K. S. Chen, "Backscattering from a randomly rough dielectric surface," *IEEE Transactions on Geoscience and Remote Sensing*, vol. 30, no. 2, pp. 356–369, 1992.

[10] Y. Oh, K. Sarabandi, and F. T. Ulaby, "An empirical model and an inversion technique for radar scattering from bare soil surfaces," *IEEE Transactions on Geoscience and Remote Sensing*, vol. 30, no. 2, pp. 370–381, 1992.

[11] J. M. Stiles and K. Sarabandi, "Electromagnetic scattering from grassland—Part I: a fully phase-coherent scattering model," *IEEE Transactions on Geoscience and Remote Sensing*, vol. 38, no. 1, pp. 339–348, 2000.

[12] J. M. Stiles, K. Sarabandi, and F. T. Ulaby, "Electromagnetic scattering from grassland—Part II: measurement and modeling results," *IEEE Transactions on Geoscience and Remote Sensing*, vol. 38, no. 1, pp. 349–356, 2000.

[13] Y. Oh and Y. C. Kay, "Condition for precise measurement of soil surface roughness," *IEEE Transactions on Geoscience and Remote Sensing*, vol. 36, no. 2, pp. 691–695, 1998.

[14] Y. Oh and J. Y. Hong, "Effect of surface profile length on the backscattering coefficients of bare surfaces," *IEEE Transactions on Geoscience and Remote Sensing*, vol. 45, no. 3, pp. 632–638, 2007.

[15] K. Sarabandi, Y. Oh, and F. T. Ulaby, "Measurement and calibration of differential Mueller matrix of distributed targets," *IEEE Transactions on Antennas and Propagation*, vol. 40, no. 12, pp. 1524–1532, 1992.

Yisok Oh

received his B.E. degree from Yonsei University, Seoul, Korea, in 1982, and his Ph.D. degree from the University of Michigan, Ann Arbor, MI, USA, in 1993, all in electrical engineering. In 1994, he joined the faculty of Hongik University, Seoul, where he is currently a professor at the School of Electronic and Electrical Engineering. His current research interests include polarimetric radar backscattering from various Earth surfaces and microwave remote sensing of soil moisture and surface roughness.

Jisung Geba Chang

received his Ph.D. degree in geo-information from the Technion – Israel Institute of Technology in 2017. His research area is remote sensing of the environment using multi-temporal data, multi/hyperspectral data, and multi-frequency/polarization SAR data. His current research interest includes machine-learning-based integration of multi-source for classification/clustering and their decomposition.

Maxim Shoshany

holds a Ph.D. degree in remote sensing from the University of Tasmania, Australia, in 1990. He is currently a full professor at the Faculty of Civil and Environmental Engineering at the Technion – Israel Institute of Technology. His research area is environmental geo-information, specializing in remote sensing and spatio-temporal modeling of Mediterranean and arid environments.

JOURNAL OF ELECTROMAGNETIC ENGINEERING AND SCIENCE, VOL. 21, NO. 2, 111~118, APR. 2021

https://doi.org/10.26866/jees.2021.21.2.111
ISSN 2671-7263 (Online) · ISSN 2671-7255 (Print)

Imbalance Detection of Rotor Rotational Speed Using Doppler Radar

Young-Jae Choi · In-Sik Choi*

Abstract

In operating a wind turbine, both predictive and condition-based maintenances are required to minimize the downtime caused by maintenance. The imbalance of rotor rotational speed is an important factor for diagnosing wind turbine failures. The rotational speed imbalance can be caused by accumulated damage or the accumulation of ice, dust, and moisture. In this paper, we proposed a method for detecting the rotational speed imbalance of a wind turbine using a Doppler radar. We calculated the difference in the rotational speed for different times using spectrograms obtained by observing the wind turbine with a Doppler radar and determined the rotational speed imbalance using the fast Fourier transform. The performance of the proposed algorithm was verified using both synthetic and numerical data.

Key Words: Doppler Radar, Dynamic Radar Cross-Section, Imbalance Detection, Spectrogram, Wind Turbine.

I. INTRODUCTION

The wind power market has grown rapidly over the past decade. Although wind power is a well-known eco-friendly energy source, the associated operating and maintenance costs are high [1]. In particular, wind turbines are expensive to maintain because they require expensive cranes to lift the equipment [1]. In general, predictive maintenance (PdM) and condition-based maintenance (CBM) are required to minimize the downtime of wind turbines due to maintenance [1]. To realize the PdM and CBM, a condition monitoring system is often required. For wind turbines, the main failures can be found in the gearboxes, bearings, generators, rotors, blades, and pitch control systems [1, 2]. Among these failures, rotor imbalance can be caused by damage accumulated on the rotor blades or by the accumulation of uneven ice, dust, and moisture [2]. Regarding direct-drive wind turbines, analyzing the current output of the generator can detect rotor imbalance [1]. This is because a direct-drive wind turbine can directly affect the output current of the rotor. From previous studies, power spectral density analysis, bicoherence analysis, time-frequency analysis, amplitude demodulation, and data mining have been used for the imbalance fault detection of wind turbines [3]. It is clear that data can be obtained when a sensor is installed on the rotor axis [4]; however, sensor installation remains a very difficult task [1]. It is expected that if the rotational motion of the blade can be directly observed, many shortcomings of the existing methods can be overcome. However, since the wind turbine blade is a large structure of several tens of meters, it is complex to accurately observe the rotational motion of the blade. In the past decade, radars have been used in many studies to measure wind turbines. Laboratory measurements of spectrograms for wind turbine scale models were reported

Manuscript received July 25, 2020 ; Revised October 31, 2020 ; Accepted November 16, 2020. (ID No. 20200725-109J)
Department of Electrical & Electronic Engineering, Hannam University, Daejeon, Korea.
*Corresponding Author: In-Sik Choi (e-mail: recog@hnu.kr)

in 2010 and 2013 [5–8]. From 2015 to 2017, studies have been conducted to directly measure the industrial wind turbine to obtain the spectrogram [9–11]. Many studies have examined the performance of structural health monitoring of wind blades using noncontact sensors. Many types of noncontact sensors have been used in structural health monitoring, including infrared thermography, laser sensors, and microwaves [12]. The requirement for many of these sensors is that the target rotors are stationary or only move slowly during the measurements. In particular, the radar-based method has shown good performance. Since this method requires a wide bandwidth, the system is expensive; thus, more affordable methods require exploration. It is important to note from these studies that Doppler radar can be used to construct a system to observe the entire blade of an industrial wind turbine at very low costs [10]. Also, it was commonly reported that a unique flash component can be found in the spectrogram of a rotating wind blade [9–11]. The occurrence of the flash component is the most evident characteristic of a wind blade and is closely related to its motion state [9–11]. In this study, we propose a method for detecting the imbalance of the wind turbine blade with the spectrogram obtained using Doppler radar. We describe the phenomenon that occurs when a wind-turbine blade rotates at an unbalanced speed. Then, we explain the effect of this phenomenon on the obtained spectrogram. Also, we introduce an algorithm that can detect the imbalance using these characteristics. Finally, the proposed method is verified using both synthetic and numerical data.

II. Proposed Method

1. Derivation of the Algorithm

Wind turbine blades are normally large structures of several tens of meters and are affected by gravity during rotation. The mass balance between the three blades of a wind turbine is critical for the blades to rotate stably under gravity. Fig. 1 illustrates a situation in which the mass balance of blades is violated [3, 13].

In Fig. 1, it is assumed that the mass of each blade is M, except that one blade has an additional mass of m. Any slight differences between the masses of the three blades are neglected. When mass M is removed from each blade, the model can be simplified to have only one blade with mass m [3]. In the simplified model, the change in angular acceleration during rotation is illustrated in Fig. 2.

In Fig. 2(a), the maximum acceleration is applied when the rotating angle is $0°$, while the maximum deceleration is applied at $180°$. Therefore, the angular acceleration at different blade rotation angles is cosinusoidal function (Fig. 2(b)). Fig. 2(a) is referred to as a mass model in related studies [3, 14]. From Eq. (9) of [14], the angular acceleration is derived below:

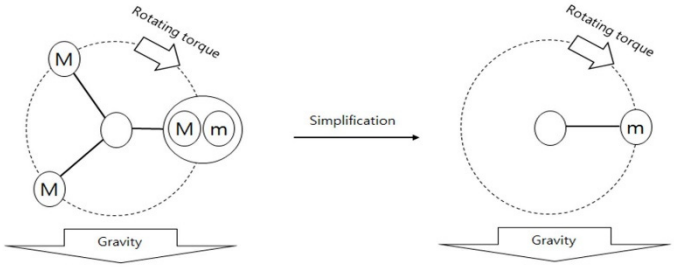

Fig. 1. Illustrative model of the wind turbine blades with unbalanced masses.

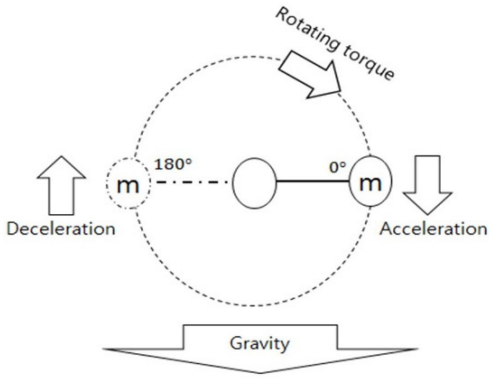

(a)

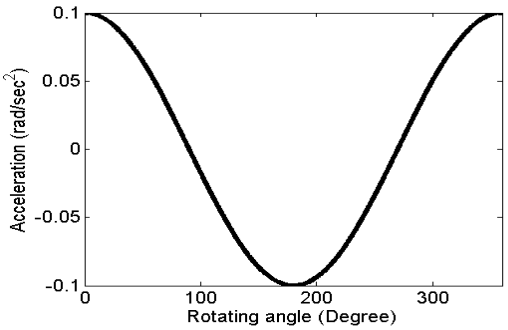

(b)

Fig. 2. Change in the acceleration of imbalanced blades: (a) the simplified model and (b) acceleration.

$$a(t) = z\ cos(2\pi Xt), \tag{1}$$

where X is the revolution per second (rps) of the rotor, t is the time sample, and z is a variable that determines the amount of change in acceleration. z is proportional to the additional mass. The rotational speed of the wind blade, which is changed by the acceleration of Eq. (1), can be obtained as

$$\Omega(t) = 2\pi X + \int_0^t z\ cos(2\pi Xt)\, dt = 2\pi X + \frac{z\ sin(2\pi Xt)}{2\pi X} \tag{2}$$

Adding the base rotational speed $2\pi X$ to Eq. (2) and integrating it regarding t, we can obtain the rotation angle of the wind turbine blade regarding time as

$$\theta(t) = \int_0^t \left(2\pi X + \frac{z\ sin(2\pi Xt)}{2\pi X}\right) dt = 2\pi Xt - \frac{z\ cos(2\pi Xt)}{4\pi^2 X^2} \quad (3)$$

Eq. (4) can be obtained by removing the term $2\pi Xt$ from Eq. (3).

$$\theta(t) - 2\pi Xt = -\frac{z\ cos(2\pi Xt)}{4\pi^2 X^2} \quad (4)$$

The Fourier transform is applied to the left side of Eq. (4), and we can obtain

$$\Theta(X_n) = \left|\int_{-T/2}^{T/2} -\frac{z\ cos(\Omega_0 t)}{\Omega_0^2} exp(-j2\pi X_n t)\, dt\right| = \left|-\frac{z\left(\frac{1}{2}sinc(\pi XT-\pi TX_n)-\frac{1}{2}sinc(\pi XT+\pi TX_n)\right)}{4\pi^2X^2}\right| = \left|\frac{\frac{z}{2}sinc(\pi XT+\pi TX_n)}{4\pi^2X^2}\right| + \left|\frac{\frac{z}{2}sinc(\pi XT-\pi TX_n)}{4\pi^2X^2}\right| \quad (5)$$

In Eq. (5), X is always positive, and thus, Eq. (5) can be simplified to

$$\Theta(X_n) = \left|\frac{\frac{z}{2}sinc(\pi XT - \pi TX_n)}{4\pi^2X^2}\right| \quad (6)$$

where $\Theta(X_n)$ reaches its maximum value when $X_n = X$, and z is always positive. By substituting $X_n = X$ into Eq. (6), we obtain

$$z = 8\pi^2X^2\Theta(X) \quad (7)$$

2. Parameter Estimation Algorithm

From Eqs. (3) to (7), z and X in Eq. (1) can be estimated from $\theta(t)$ in Eq. (3), and $\theta(t)$ can be obtained from the spectrogram. Fig. 3 shows the relationship between the rotation angle and the spectrogram of a rotating wind blade.

In Fig. 3(b), a flash occurs in the positive Doppler direction whenever the blade passes the $0°$ point. Regarding the three blades, the angle between each blade is $120°$ and, therefore, the rotation angle between each flash is $120°$.

The time sample in which the n-th flash occurs is substituted into t_n, and the rotation angle corresponding to the n-th flash is calculated using

$$\theta(t_n) = \frac{2\pi}{3}n, \quad (8)$$

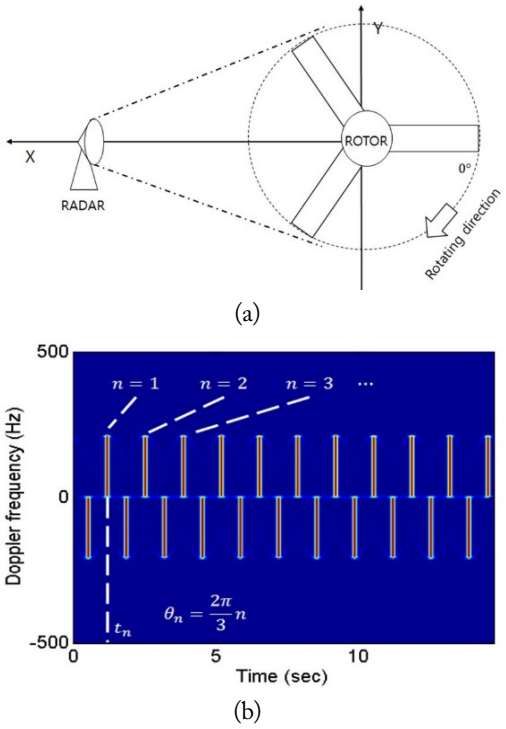

Fig. 3. Relationship between the rotation angle and the spectrogram of a rotating wind blade: (a) the geometry of the rotating rotor blade and radar and (b) the spectrogram of a rotating rotor blade.

where $n = 1, 2, \cdots, N$, and N is the number of flashes on the positive Doppler direction of the spectrogram.

From Eq. (8), we obtain $\dot{X}$ and b that satisfy the condition given by

$$\dot{X} = \min_{\dot{X},b} \sum_{n=1}^{N} \left(\theta(t_n) - (2\pi\dot{X}t_n + b)\right)^2, \quad (9)$$

where b is the initial rotation angle, $\dot{X}$ can be obtained by the least square solution according to [15], as given by

$$\vec{x} = \begin{bmatrix} 2\pi\dot{X} \\ b \end{bmatrix} = (\bar{A}^T\bar{A})^{-1}\bar{A}^T\vec{\theta}, \quad (10)$$

where $\vec{\theta} = [\theta(t_n)] \in \mathbb{R}^N$ and $\bar{A} = [t_n \quad 1_n] \in \mathbb{R}^{N\times 2}$. For $\vec{\theta}$, the primary and direct current components obtained in Eq. (10) are removed and the frequency spectrum is obtained using

$$\Theta(X_j) = \left|\overrightarrow{D_J}^T\left(\vec{\theta} - \bar{A}\vec{x}\right)\right|, \quad (11)$$

where $\overrightarrow{D_J} = \left[exp(-j2\pi X_j t_n)\right] \in \mathbb{C}^N$ and $\vec{\Theta} = \left[\Theta(X_j)\right] \in \mathbb{R}^J$, J is the number of samples on the frequency axis, and $X_j = 1.5(j-1)\frac{\dot{X}}{J}$. From Eq. (11), the element with the maximum value is located at $\dot{X}$, and its value is equal to

$$\Theta(\dot{X}) = \max\vec{\Theta} \quad (12)$$

Substituting $\Theta(\dot{X})$ into Eq. (7), and z can be estimated by

$$\dot{z} = 8\pi^2 X^2 \Theta(\dot{X}) \tag{13}$$

3. Flash Extraction from Spectrogram

The proposed method can accurately extract the interval between two flashes that appear in the spectrogram. The signal vector of the dynamic radar cross-section can be obtained by $\vec{s} = [s_p] \in \mathbb{C}^P$. The spectrogram $\overline{S} = [S_{q,p}] \in \mathbb{R}^{Q\times P}$ can be obtained by performing a short-time Fourier transform on $\vec{s}$ [16], where Q is the number of Doppler frequency samples and P is the number of time samples. The spectrogram can be converted to a one-dimensional vector using

$$U_p = \sum_{q=1}^{Q} S_{q,p} F_q, \tag{14}$$

where F_q is the q-th sample of the Doppler frequency and $\vec{U} = [U_p] \in \mathbb{R}^P$ is the vector of one-dimensional signals obtained from Eq. (14). Fig. 4 shows the one-dimensional graph obtained by substituting the spectrogram of Fig. 3(b) into Eq. (14).

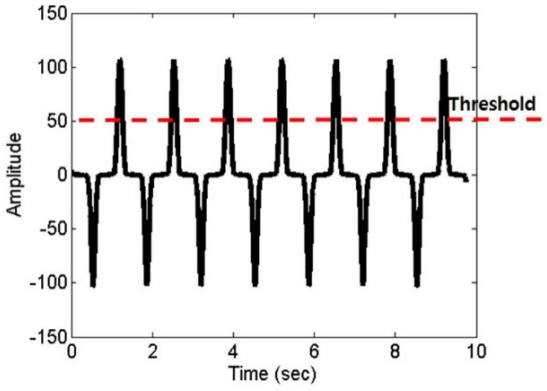

(a)

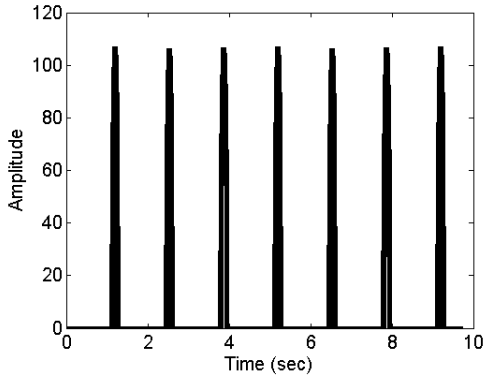

(b)

Fig. 4. One-dimensional graph: (a) example of the one-dimensional graph and (b) the graph after applying threshold.

The location of the flash in the spectrogram in Fig. 3(b) is the same as the peak location in the one-dimensional graph in Fig. 4(a). A threshold is applied to remove unwanted components by

$$U_p^m = \begin{cases} U_p & others \\ 0 & U_p < B \end{cases} \tag{15}$$

where $p = 1,2,\cdots P$, $m = 1$ is the iteration index, and B is the threshold value. In this study, we use $B = \frac{U_{max}}{2}$ and $U_{max} = \max \vec{U}$.

The peak is removed using the following procedure:

Step 1. Defining a vector $\overrightarrow{U_m} = [U_p^m] \in \mathbb{R}^P$ using U_p^m, and initializing it from $m = 1$;

Step 2. Using Eq. (16) to find p that makes $\overrightarrow{U_m}$ the largest;

Step 3. Removing the extracted component from $\overrightarrow{U_m}$ using Eq. (17);

Step 4. Updating with $m = m + 1$;

Step 5. Repeating Steps 2–4 until there is no component to extract;

Step 6. Sorting $\vec{K} = [K_m] \in \mathbb{R}^P$ in ascending order. $\vec{K} = [K_p] \in \mathbb{R}^P$ is the vector of time index, where $p = 1,2,\cdots P$, and p is the index assigned to the element while sorting $\vec{K}$. By substituting $n = K_p$ into Eq. (8), we obtain $t_n = t(K_p)$ and $\theta(t_n)$.

$$K_m = \max_p \overrightarrow{U_m} \tag{16}$$

$$U_p^{m+1} = \begin{cases} U_p^m & others \\ 0 & p_{min} < p < p_{max} \end{cases} \tag{17}$$

$$p_{min} = \begin{cases} K_m - 2W & ,others \\ 1 & (K_m - 2W) < 1 \end{cases} \tag{18}$$

$$p_{max} = \begin{cases} K_m + 2W & ,others \\ P & (K_m + 2W) > P \end{cases} \tag{19}$$

where W is the number of time samples corresponding to the width of the flash in the spectrogram.

III. Simulation

1. Synthetic Data

Assuming that the radar observes the wind turbine from the side, the point scatter model of a rotor with three blades can be simply expressed as in [17]:

$$s_p = \sum_{k=0}^{2} sinc(\Phi_k(p))\, exp\{j\Phi_k(p)\} \tag{20}$$

where $\Phi_k(p)$ is given in [17] as

$$\Phi_k(p) = \frac{4\pi f}{c}\frac{L}{2}cos\left(\Omega t_p + k\pi\frac{2}{3} + \frac{\pi}{2}\right), \quad (21)$$

where Ωt_p is the rotational angle at t_p. In our problem, the rotational speed, Ω, changes over time. Thus, $\theta(t)$ should be used instead of Ωt_p. $\theta(t)$ is given by Eq. (3). Eq. (22) can be obtained by substituting $\theta(t)$ into Eq. (21).

$$\Phi_k(p) = \frac{4\pi f}{c}\frac{L}{2}cos\left(k\pi\frac{2}{3} + \frac{\pi}{2} + 2\pi X t_p - \frac{z\ cos(2\pi X t_p)}{4\pi^2 X^2}\right), \quad (22)$$

where L is the radius of the rotor, f is the radar transmission frequency, and c is the speed of light in the free space. Table 1 lists the parameters for the simulation in this study. Fig. 3(a) shows the geometry of the simulation.

In Table 1, f_s is a sampling frequency. Fig. 5 shows the frequency spectrum $\Theta(X_j)$ calculated by applying the proposed algorithm to the composite data using the parameters listed in Table 1. As illustrated in Fig. 5, the peak occurs at 0.28 rps in the rotation period of the wind blade. As z increases, higher peaks occur at the corresponding positions, and therefore, it is possible to determine the degree of wind turbine imbalance by checking the peaks. In Fig. 5, the peak value can be substituted into Eq. (7) to calculate z, and the results are as listed in Table 2.

It can be summarized in Table 2 that the estimated z shows an error below 2%, compared to the actual z. However, for $z = 0.01$, where the amplitude of the acceleration is small, the error exceeds 4%. $z = 0.01$ is the limit of the z value that can be extracted under the conditions of Table 1. By increasing the sampling frequency and observation time, the precision of the observation value can be improved.

Fig. 6 illustrates the frequency spectrum when the condition is changed to $X = 0.2$ rps.

As illustrated in Fig. 6, the peak occurs at 0.2 rps in the rotation cycle of the wind blade. However, $\Theta(X_j)$ for different z values is found to differ from that in Fig. 5. Table 3 summarizes the z values calculated by substituting the peak value obtained in Fig. 6 into Eq. (7).

Table 1. Parameters of the synthetic simulation

Parameter	Value
L	11 m
X	0.28 rps
f	1 GHz
f_s	1,200 sps
P	144,000
t_P	120 s

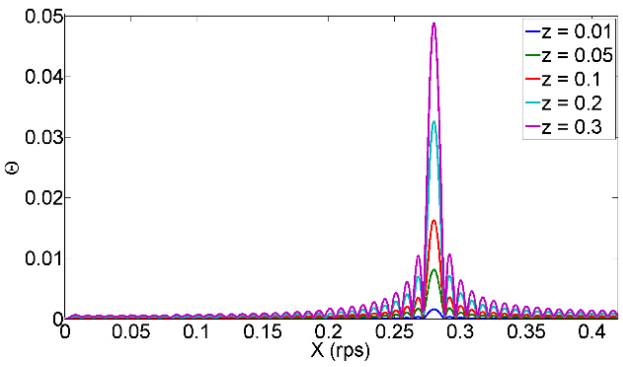

Fig. 5. Frequency spectrum for different z (rad/sec^2) values (X = 0.28 rps).

Table 2. Estimated parameters of the synthetic simulation (X = 0.28 rps)

True z (rad/sec^2)	Estimated z (rad/sec^2)	Relative error for z (%)
0.01	0.0096	4.43
0.05	0.0504	0.84
0.1	0.1007	0.73
0.2	0.2022	1.11
0.3	0.3046	1.54

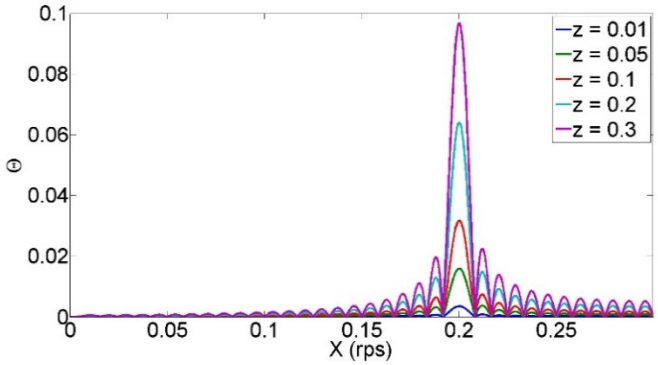

Fig. 6. Frequency spectrum for different z (rad/sec^2) values (X = 0.2 rps).

Table 3. Estimated parameters of the synthetic simulation (X = 0.2 rps)

True z (rad/sec^2)	Estimated z (rad/sec^2)	Relative error for z (%)
0.01	0.0110	10.28
0.05	0.0507	1.43
0.1	0.1005	0.45
0.2	0.2039	1.97
0.3	0.3054	1.79

From Table 3, the estimated z also shows an error below 2%, compared to the actual z. However, for $z = 0.01$, where the amplitude of the acceleration is small, the error exceeds 10%.

2. Numerical Data

The numerical data are calculated using the physical optics method by reflecting the rotational speed obtained using Eq. (2) [18]. Table 4 illustrates the parameters used for the simulation. Doppler radar used a continuous wave and a horizontal polarization. The material of wind turbine was considered a perfect electric conductor.

Fig. 7 illustrates the spectrogram of the numerical data. At signal-to-noise ratio (SNR) of 5 dB, there is almost no flash in the negative Doppler direction. This is because the front part of the round shape in the airfoil of the wing has a larger radar cross section (RCS) than the rear part of the pointed shape. Moreover, despite the change in z values, the change in the spectrogram is insignificant in both pictures. Therefore, it is not possible to obtain the change in z from the images. Fig. 8 illustrates the results of calculating the

Table 4. Parameters of the numerical simulation

Parameter	Value
L	1 m
X	0.25 rps
f	24 GHz
f_s	600 sps
P	36,000
t_P	60 s

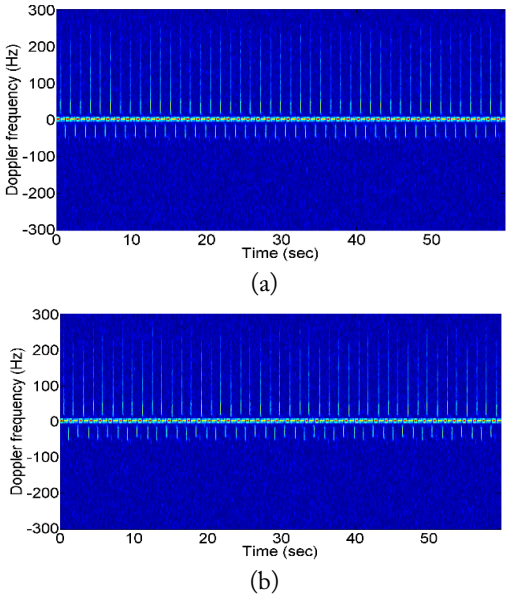

Fig. 7. Spectrogram obtained from the numerical data with SNR = 5 dB: (a) $z = 0.1$ rad/sec^2 and (b) $z = 0.3$ rad/sec^2.

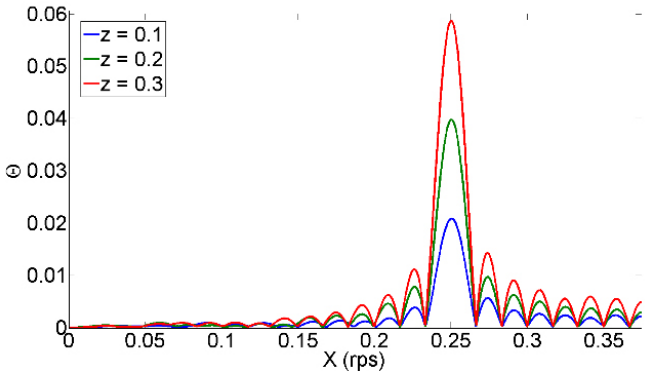

Fig. 8. Frequency spectrum for different z (rad/sec^2) values with SNR = 5 dB.

Table 5. Estimated parameters of the numerical simulation with X = 0.25 rps and SNR = 5 dB

True z (rad/sec^2)	Estimated z (rad/sec^2)	Relative error for z (%)
0.1	0.1028	2.8
0.2	0.1961	1.95
0.3	0.2883	3.9

frequency spectrum by applying the proposed method to the images in Fig. 7. Table 5 shows the z extracted by the proposed method and their relative errors. From Table 5, the estimated z shows an error below 4% compared to the actual z.

We used the additive Gaussian noise to represent a noisy signal. In this paper, SNR is defined based on the signal power excluding DC components. Fig. 9 shows the relative error of the proposed method calculated by 5,000 times Monte-Carlo simulation. The relative error is given by:

$$\mathrm{RE} = \frac{|S - N|}{S} \times 100 \ (\%), \tag{23}$$

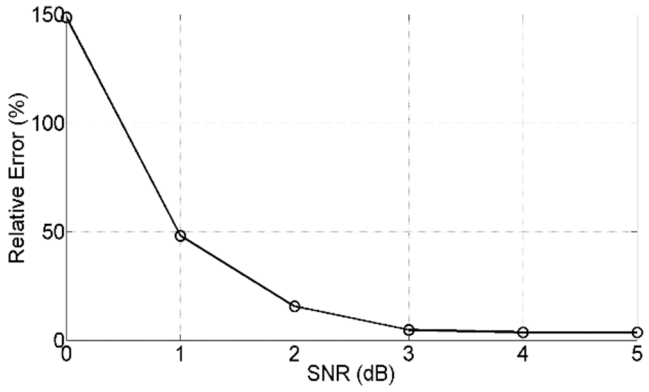

Fig. 9. Relative error of the proposed method calculated by 5,000 times Monte-Carlo simulation; $z = 0.3$ (rad/sec^2).

where S is the signal power, and N is the noise power. Fig. 10 shows the error of z estimated by the proposed method in a frequency range from 1 GHz to 24 GHz.

In Fig. 10, it is shown that the errors of z estimated by the proposed method are almost the same, from 1 GHz to 24 GHz. These results suggest that the proposed method has equal performance regardless of frequency.

IV. Discussion and Conclusion

In this study, we proposed a method to detect the imbalance of the rotational speed and the rotational acceleration of wind turbines using the Doppler radar. The proposed method can accurately estimate the rotational speed of the wind turbine and the acceleration amplitude on the blade with an error within 2%. Therefore, it is possible to detect the rotational speed imbalance of the wind turbine blade from the acceleration value of the blade. However, when $z = 0.01$, the error was found to increase significantly. This study primarily presented a method that can detect the imbalance of rotational speed using Doppler radar outside the wind turbine. While most sensors that determine the state of motion of a wind turbine acquire data from the blade rotation axis, Doppler radar can obtain data by directly observing the blade motion. Thus, the Doppler radar can provide a simpler way of obtaining data compared to the existing sensors. It is suggested that adding a Doppler radar to the existing condition monitoring system to observe the blades of a wind turbine is useful for diagnosing faults in the wind turbine.

Although the performance of the proposed method has been verified through simulation, there is a problem in practice that requires consideration. The power received by rainfall clutter is proportional to the square of the frequency. It is known that, in a high-frequency system such as a 24-GHz Doppler radar, weather clutter—rainfall or fog—can cause serious performance degradation. This problem can be avoided using a low-frequency system—L-band; however, low-frequency radar systems are more expensive than high frequency radar systems. Therefore, it is necessary to determine the optimum operating frequency by considering performance, economics, and portability.

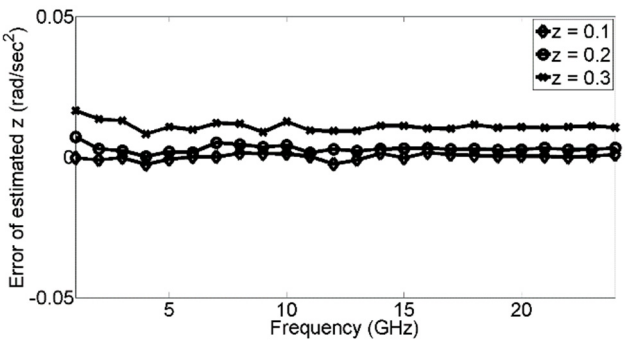

Fig. 10. Relative error of z in a frequency range from 1 GHz to 24 GHz (noise free).

When the rotor rotation speed is measured using a Doppler radar, the change in angular speed due to the imbalance of the rotor rotation speed is too small to determine the wind turbine failure. However, the change in the rotor rotation speed has a periodic pattern, which can be expressed as sinusoidal. Finally, the sinusoidal wave can be extracted using a Fourier transform. Using this principle, it is possible to estimate accurately the imbalance of the rotor rotation speed.

This research was supported by the Korea Electric Power Corporation (No. R19XO01-50). This work was also supported by the National Research Foundation of Korea (NRF) grant funded by the Korean government (Ministry of Science, ICT & Future Planning) (No. NRF2018R1D1A1B07041496).

References

[1] B. Lu, Y. Li, X. Wu, and Z. Yang, "A review of recent advances in wind turbine condition monitoring and fault diagnosis," in *Proceedings of 2009 IEEE Power Electronics and Machines in Wind Applications*, Lincoln, NE, 2009, pp. 1-7.

[2] S. A. Saleh and C. R. Moloney, "Development and testing of wavelet packet transform-based detector for ice accretion on wind turbines," in *Proceedings of 2011 Digital Signal Processing and Signal Processing Education Meeting (DSP/SPE)*, Sedona, AZ, 2011, pp. 72–77.

[3] X. Gong and W. Qiao, "Imbalance fault detection of direct-drive wind turbines using turbine current signals," *IEEE Transactions on Energy Conversion*, vol. 27, no. 2, pp. 468–476, 2012.

[4] W. Yang, P. J. Tavner, and M. Wilkinson, "Wind turbine condition monitoring and fault diagnosis using both mechanical and electrical signatures," in *Proceedings of 2008 IEEE/ASME International Conference on Advanced Intelligent Mechatronics*, Xian, China, 2008, pp. 1296–1301.

[5] A. Naqvi, S. Yang, and H. Ling, "Investigation of Doppler features from wind turbine scattering," *IEEE Antennas and Wireless Propagation Letters*, vol. 9, pp. 485–488, 2010.

[6] F. Kong, Y. Zhang, R. Palmer, and Y. Bai, "Wind turbine radar signature characterization by laboratory measurements," in *Proceedings of IEEE RadarCon (RADAR)*, Kansas City, MO, 2011, pp. 162–166.

[7] F. Kong, Y. Zhang, and R. D. Palmer, "Wind turbine radar interference studies by polarimetric measurements of a scaled model," *IEEE Transactions on Aerospace and Electronic Systems*, vol. 49, no. 3, pp. 1589–1600, 2013.

[8] A. Naqvi and H. Ling, "Time-frequency and ISAR characteristics of wind turbines with higher order motions," *Progress in Electromagnetics Research*, vol. 143, pp. 331–347, 2013.

[9] J. Munoz-Ferreras, Z. Peng, Y. Tang, R. Gomez-Garcia, and C. Li, "Doppler-radar-based short-range acquisitions of time-frequency signatures from an industrial-type wind turbine," in *Proceedings of IEEE Topical Conference on Wireless Sensors and Sensor Networks (WiSNet)*, Phoenix, AZ, 2017, pp. 5–7.

[10] T. Nikoubin, J. Munoz-Ferreras, R. Gomez-Garcia, D. Liang, and C. Li, "Structural health monitoring of wind turbines using a low-cost portable k-band radar: An ab-initio field investigation," in *Proceedings of 2015 IEEE Topical Conference on Wireless Sensors and Sensor Networks (WiSNet)*, San Diego, CA, 2015, pp. 69–71.

[11] J. Munoz-Ferreras, Z. Peng, Y. Tang, R. Gomez-Garcia, D. Liang, and C. Li, "Short-range Doppler-radar signatures from industrial wind turbines: theory, simulations, and measurements," *IEEE Transactions on Instrumentation and Measurement*, vol. 65, no. 9, 2108–2119, 2016.

[12] F. X. Ochieng, C. M. Hancock, G. W. Roberts, and J. Le - Kernec, "A review of ground-based radar as a non con tact sensor for structural health monitoring of in-field wind turbines blades," *Wind Energy*, vol. 21, no. 12, pp. 1435–1449, 2018.

[13] P. Caselitz and J. Giebhardt, "Rotor condition monitoring for improved operational safety of offshore wind energy converters," *Journal of Solar Energy Engineering*, vol. 127, no. 2, pp. 253–261, 2005.

[14] P. Li, W. Hu, R. Hu, and Z. Chen, "Imbalance fault detection based on the integrated analysis strategy for variable-speed wind turbines," *International Journal of Electrical Power & Energy Systems*, vol. 116, article no. 105570, 2020. https://doi.org/10.1016/j.ijepes.2019.105 570.

[15] T. K. Moon and W. C. Stirling, *Mathematical Methods and Algorithms for Signal Processing*. Upper Saddle River, NJ: Prentice-Hall, 2000.

[16] N. A. Khan, M. N. Jafri, and S. A. Qazi, "Improved resolution short time Fourier transform," in *Proceedings of the 7th International Conference on Emerging Technologies, Islamabad*, Pakistan, 2011, pp. 1–3.

[17] V. C. Chen "Radar signatures of rotor blades," in *Proceedings of SPIE 4391: Wavelet Applications VIII*. Bellingham, WA: The International Society for Optical Engineering, 2001, pp. 63–70, 2001.

[18] C. Y. Kee and C. Wang, "Efficient GPU implementation of the high-frequency SBR-PO method," *IEEE Antennas and Wireless Propagation Letters*, vol. 12, pp. 941–944, 2013.

Young-Jae Choi

received B.S. and M.S. degrees in Electronics Engineering from Hannam University, Daejeon, Korea, in 2013 and 2018, respectively. He is working toward a Ph.D. degree in Electronics Engineering from Hannam University, Daejeon, Korea. His research interests include radar signal processing, RCS simulation and analysis.

In-Sik Choi

received a B.S. degree in Electrical and Electronics Engineering from Kyungpook National University, Daegu, Korea in 1998 and M.S. and Ph.D. degrees in Electrical and Electronics Engineering from Pohang University of Science and Technology (POSTECH), Pohang, Korea in 2000 and 2003, respectively. From 2004 to 2007, he worked at the Agency for Defense Development as a senior research engineer. He is now a Professor in the Department of Electrical and Electronics Engineering, Hannam University, Daejeon, Korea. His research interests include radar signal processing, RCS measurement and analysis, and EMI/EMC.

JOURNAL OF ELECTROMAGNETIC ENGINEERING AND SCIENCE, VOL. 21, NO. 2, 119~125, APR. 2021

https://doi.org/10.26866/jees.2021.21.2.119
ISSN 2671-7263 (Online) · ISSN 2671-7255 (Print)

Analytical Dispersion Equations of a Lossy Coaxial Waveguide in the Microwave and Visible Spectra

Yong Heui Cho*

Abstract

Analytical hybrid-mode dispersion relations of a lossy coaxial waveguide were rigorously analyzed using a mode-matching technique. In order to model a practical coaxial line with inevitable losses, we adopted an all-dielectric coaxial waveguide surrounded by the perfect electric conductor (PEC) boundary. The rigorous dispersion characteristics of the TM_{01}, TE_{01}, and EH_{11} modes were investigated for lossy coaxial waveguides filled with different electrical conductivities. Based on the exact solutions, approximate but accurate dispersion equations were proposed for the TM_{0p}, TE_{0p} , EH_{mp}, and HE_{mp} modes in order to estimate and compare the behaviors of complex propagation constants in the microwave and visible spectra.

Key Words: Coaxial Line, Complex Propagation Constant, Dispersion Relation, Guided Wave, Mode-Matching Technique.

I. INTRODUCTION

A coaxial waveguide is a fundamental transmission line to stably guide a light for optoelectronics [1–3] or precisely measure the reflection coefficient and impedance up to millimeter-wave bands [4, 5]. Accurate evaluation of wave propagation through a practical coaxial waveguide is essential for quantifying measurement uncertainty occurring in microwave transmission [5]. Even in the visible spectrum, a nanocoax [3] is one of the promising structures for low-loss propagation composed of plasmonic and photonic modes, where the permittivity can be negative or complex to model real metals at optical frequency.

Since a practical coaxial line is inherently lossy owing to finite electrical conductivity, the TM wave ($E_z \neq 0,\ H_z = 0$) instead of the TEM wave ($E_z = 0,\ H_z = 0$) propagates and is gradually decreased in the z-direction. This behavior makes the dispersion analysis of the lossy coaxial waveguide more involved. Therefore, it is of great importance to derive and formulate an exact and rigorous dispersion relation of the lossy coaxial waveguide, which can be modeled as a multilayered dielectric coaxial waveguide [1, 6–8]. A dielectric coaxial waveguide was analyzed using the boundary conditions of an open region [6] and an infinitely lossy outer conductor [7, 8]. In the following sections, we apply a standard mode-matching technique [9] for analyzing a dielectric coaxial waveguide surrounded by the perfect electric conductor (PEC) boundary. A newly-derived rigorous dispersion relation is used to determine precise complex propagation constants for the hybrid, TM, and TE modes in microwave and optical spectra, where we use Davidenko's method [10, 11] for searching complex roots.

Using the conductor condition or high permittivity approximation, we obtained simplified but accurate dispersion equations useful for characterizing the transmission behaviors of the lossy coaxial waveguide. This means that our rigorous dispersion equations can be utilized to generate the field distributions for the TM_{0p}, TE_{0p}, EH_{mp}, and HE_{mp} modes and formulate the

Manuscript received August 22, 2020 ; Revised November 5, 2020 ; Accepted December 1, 2020. (ID No. 20200822-125J)
School of Information and Communication Engineering, Mokwon University, Daejeon, Korea.
*Corresponding Author: Yong Heui Cho (e-mail: yongheui.cho@gmail.com)

scattering characteristics of canonical coaxial structures used in a coaxial calibration kit [5]. The quasi-TEM mode also yields a closed-form approximate solution for the TM_{01}-mode complex propagation constant, which becomes identical to the propagation constant [5, 7] in the high electrical conductivity limit.

II. Mode-Matching Analysis

A lossy coaxial waveguide can be modeled using a multilayered dielectric coaxial waveguide [1, 6–8] as shown in Fig. 1, where the medium constants—$\epsilon_1, \epsilon_2, \epsilon_3$ and μ_1, μ_2, μ_3—can be any complex number. We use and omit $e^{i(\beta z-\omega t)}$ for the time convention, where β is a complex propagation constant composed of phase ($\Re[\beta]$) and attenuation ($\Im[\beta]$) constants. The interesting point of the geometry shown in Fig. 1 is that a dielectric coaxial waveguide [1, 6–8] shown in Fig. 2 is entirely surrounded by the PEC boundary. It is known that unwanted multiple leaky modes [11] are inevitably generated in open magnetodielectric waveguides including dielectric coaxial structures [1, 6] with an open boundary as shown in Fig. 2. The existence of leaky phenomena caused by the open boundary makes a dispersion analysis of the dielectric coaxial waveguide much more involved. For instance, the dielectric coaxial waveguide shown in Fig. 2 should satisfy a leaky dispersion relation in an open region as

$$k_0^2 = \kappa_\rho^2 + \beta^2, \tag{1}$$

where $k_0 = \omega\sqrt{\mu_0\epsilon_0}$, and κ_ρ is a leaky wavenumber for a radial direction $\rho = \sqrt{x^2+y^2}$. Equating the imaginary parts of the left and right sides of Eq. (1) yields a leaky-wave relation for κ_ρ and β as

$$\Re[\kappa_\rho]\Im[\kappa_\rho] = -\Re[\beta]\Im[\beta], \tag{2}$$

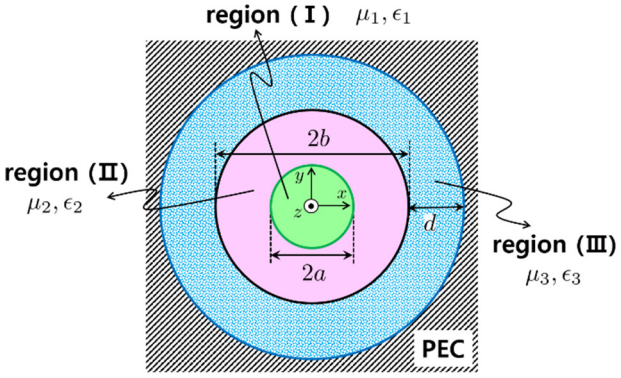

Fig. 1. Modeling of a lossy coaxial waveguide using a multilayered dielectric coaxial waveguide surrounded by the perfect electric conductor (PEC) boundary.

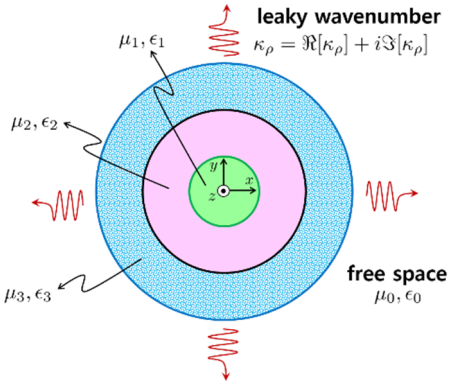

Fig. 2. The geometry of a three-layered dielectric coaxial waveguide placed in free space or with an open boundary.

where the phase term of a guided wave is $e^{i(\kappa_\rho\rho+\beta z)}$. Eq. (2) indicates that the radial and longitudinal radiation conditions of κ_ρ and β cannot be satisfied at the same time, owing to the fact that the signs of the real or imaginary parts of κ_ρ and β are always different from each other. Contrary to the geometry shown in Fig. 2, the PEC boundary and lossy region (III) introduced in Fig. 1 enable us to block the leaky modes completely and model the conductor loss precisely. This is because the PEC boundary at $\rho = b + d$ is imposed and ϵ_3 can be complex, thus confirming there are no leaky modes and the waves are evanescent in region (III). Therefore, the field representations for regions (I) through (III) as shown in Fig. 1 are formulated using magnetic and electric vector potentials [9]:

$$A_z^{\mathrm{I}}(\bar{r}) = \sum_{m=-\infty}^{\infty} A_m J_m(\kappa_1\rho)e^{im\phi}, \tag{3}$$

$$A_z^{\mathrm{II}}(\bar{r}) = \sum_{m=-\infty}^{\infty} \left[E_m^{(1)}J_m(\kappa_2\rho) + E_m^{(2)}N_m(\kappa_2\rho)\right]e^{im\phi}, \tag{4}$$

$$A_z^{\mathrm{III}}(\bar{r}) = \sum_{m=-\infty}^{\infty} G_m C_m(\kappa_3\rho)e^{im\phi}, \tag{5}$$

$$F_z^{\mathrm{I}}(\bar{r}) = \sum_{m=-\infty}^{\infty} B_m J_m(\kappa_1\rho)e^{im\phi}, \tag{6}$$

$$F_z^{\mathrm{II}}(\bar{r}) = \sum_{m=-\infty}^{\infty} \left[F_m^{(1)}J_m(\kappa_2\rho) + F_m^{(2)}N_m(\kappa_2\rho)\right]e^{im\phi}, \tag{7}$$

$$F_z^{\mathrm{III}}(\bar{r}) = \sum_{m=-\infty}^{\infty} H_m D_m(\kappa_3\rho)e^{im\phi}, \tag{8}$$

where $A_m, B_m, E_m^{(1),(2)}, F_m^{(1),(2)}, G_m$, and H_m are the unknown modal coefficients for the mth azimuthal mode, $\rho = \sqrt{x^2+y^2}$, $\phi = \tan^{-1}(y/x)$, $\kappa_n = \sqrt{k_n^2 - \beta^2}$, $k_n = \omega\sqrt{\mu_n\epsilon_n}$,

$$C_m(\psi) = J_m(\psi)N_m[\kappa_3(b+d)] - N_m(\psi)J_m[\kappa_3(b+d)], \quad (9)$$

$$D_m(\psi) = J_m(\psi)N'_m[\kappa_3(b+d)] - N_m(\psi)J'_m[\kappa_3(b+d)], \quad (10)$$

and $(\cdot)'$ denotes differentiation for the entire argument; $J_m(\cdot)$ and $N_m(\cdot)$ are the mth order Bessel functions of the first and second kinds, respectively. Based on the standard mode-matching analysis [9], we enforce E_z-, E_ϕ-, H_z-, and H_ϕ-field continuities at $\rho = a$ and b for the mth azimuthal mode. First, by multiplying the E_z- and H_z-field continuities at $\rho = a$ by $e^{-il\phi}$ $(l = 0, \pm1, \pm2, \cdots)$ and integrating over $0 \le \phi \le 2\pi$ yields, respectively, we get:

$$A_m J_m(u_1) = \frac{\mu_1\epsilon_1\kappa_2^2}{\mu_2\epsilon_2\kappa_1^2}\varepsilon_m(u_2), \quad (11)$$

$$B_m J_m(u_1) = \frac{\mu_1\epsilon_1\kappa_2^2}{\mu_2\epsilon_2\kappa_1^2}\varphi_m(u_2), \quad (12)$$

where $u_n = \kappa_n a$,

$$\varepsilon_m(u) = E_m^{(1)}J_m(u) + E_m^{(2)}N_m(u), \quad (13)$$

$$\varphi_m(u) = F_m^{(1)}J_m(u) + F_m^{(2)}N_m(u). \quad (14)$$

Next, we apply and integrate the E_ϕ- and the H_ϕ-field continuities at $\rho = a$ with $e^{-il\phi}$ to obtain the additional field-matching equations, respectively:

$$\frac{im}{Z_1^{\mathrm{TE}}}A_m J_m(u_1) - u_1 B_m J'_m(u_1) = \frac{\epsilon_1}{\epsilon_2}\left[\frac{im}{Z_2^{\mathrm{TE}}}\varepsilon_m(u_2) - u_2\varphi'_m(u_2)\right], \quad (15)$$

$$u_1 A_m J'_m(u_1) + \frac{im}{Y_1^{\mathrm{TM}}}B_m J_m(u_1) = \frac{\mu_1}{\mu_2}\left[u_2\varepsilon'_m(u_2) + \frac{im}{Y_2^{\mathrm{TM}}}\varphi_m(u_2)\right], \quad (16)$$

where $Z_n^{\mathrm{TE}} = \omega\mu_n/\beta$, $Y_n^{\mathrm{TM}} = \omega\epsilon_n/\beta$, $\varepsilon'_m(u) = \frac{d}{du}\varepsilon_m(u)$, and $\varphi'_m(u) = \frac{d}{du}\varphi_m(u)$. Similar to Eq. (11), in Eqs. (12), (15), and (16), we utilize the tangential boundary conditions for the E_z-, E_ϕ-, H_z-, and H_ϕ-fields at $\rho = b$. Then, we formulate the modal relations of $E_m^{(1),(2)}, F_m^{(1),(2)}, G_m$ and H_m as

$$G_m C_m(v_3) = \frac{\mu_3\epsilon_3\kappa_2^2}{\mu_2\epsilon_2\kappa_3^2}\varepsilon_m(v_2), \quad (17)$$

$$H_m D_m(v_3) = \frac{\mu_3\epsilon_3\kappa_2^2}{\mu_2\epsilon_2\kappa_3^2}\varphi_m(v_2), \quad (18)$$

$$\frac{im}{Z_3^{\mathrm{TE}}}G_m C_m(v_3) - v_3 H_m D'_m(v_3) = \frac{\epsilon_3}{\epsilon_2}\left[\frac{im}{Z_2^{\mathrm{TE}}}\varepsilon_m(v_2) - v_2\varphi'_m(v_2)\right], \quad (19)$$

$$v_3 G_m C'_m(v_3) + \frac{im}{Y_3^{\mathrm{TM}}}H_m D_m(v_3) = \frac{\mu_3}{\mu_2}\left[v_2\varepsilon'_m(v_2) + \frac{im}{Y_2^{\mathrm{TM}}}\varphi_m(v_2)\right], \quad (20)$$

where $v_n = \kappa_n b$. Combining and simplifying Eqs. (11), (12), and (15)–(20), we obtained the mth hybrid-mode dispersion relation as

$$|\mathbf{\Phi}_m(\beta)| = 0\ , \quad (21)$$

where $|\mathbf{A}|$ is the determinant of a matrix $\mathbf{A}$ and a system of simultaneous equations for $E_m^{(1),(2)}, F_m^{(1),(2)}$ is given by:

$$\mathbf{\Phi}_m(\beta)\mathbf{E}_m = \begin{bmatrix} \phi_{11}^{(1)} & \phi_{11}^{(2)} & \phi_{12}^{(1)} & \phi_{12}^{(2)} \\ \phi_{21}^{(1)} & \phi_{21}^{(2)} & \phi_{11}^{(1)} & \phi_{11}^{(2)} \\ \phi_{31}^{(1)} & \phi_{31}^{(2)} & \phi_{32}^{(1)} & \phi_{32}^{(2)} \\ \phi_{41}^{(1)} & \phi_{41}^{(2)} & \phi_{31}^{(1)} & \phi_{31}^{(2)} \end{bmatrix}\begin{bmatrix} E_m^{(1)} \\ E_m^{(2)} \\ F_m^{(1)} \\ F_m^{(2)} \end{bmatrix} = 0\ . \quad (22)$$

The elements of $\mathbf{\Phi}_m(\beta)$ are defined by:

$$\phi_{11}^{(n)} = im\frac{u_2^2 - u_1^2}{(u_1u_2)^2}Z_m^{(n)}(u_2), \quad (23)$$

$$\phi_{12}^{(n)} = Z_2^{\mathrm{TE}}\frac{Z_m^{(n)\prime}(u_2)}{u_2} - Z_1^{\mathrm{TE}}\frac{J'_m(u_1)}{J_m(u_1)}\frac{Z_m^{(n)}(u_2)}{u_1}, \quad (24)$$

$$\phi_{21}^{(n)} = Y_1^{\mathrm{TM}}\frac{J'_m(u_1)}{J_m(u_1)}\frac{Z_m^{(n)}(u_2)}{u_1} - Y_2^{\mathrm{TM}}\frac{Z_m^{(n)\prime}(u_2)}{u_2}, \quad (25)$$

$$\phi_{31}^{(n)} = im\frac{v_2^2 - v_3^2}{(v_1v_3)^2}Z_m^{(n)}(v_2)\ , \quad (26)$$

$$\phi_{32}^{(n)} = Z_2^{\mathrm{TE}}\frac{Z_m^{(n)\prime}(v_2)}{v_2} - Z_3^{\mathrm{TE}}\frac{D'_m(v_3)}{D_m(v_3)}\frac{Z_m^{(n)}(v_2)}{v_3}, \quad (27)$$

$$\phi_{41}^{(n)} = Y_3^{\mathrm{TM}}\frac{C'_m(v_3)}{C_m(v_3)}\frac{Z_m^{(n)}(v_2)}{v_3} - Y_2^{\mathrm{TM}}\frac{Z_m^{(n)\prime}(v_2)}{v_2}, \quad (28)$$

where

$$Z_m^{(n)}(u) = \begin{cases} J_m(u) & \text{if } n = 1 \\ N_m(u) & \text{if } n = 2 \end{cases}. \quad (29)$$

Therefore, a complex propagation constant β can be determined by solving Eq. (21). When $m = 0$, the hybrid-mode dispersion relation shown in Eq. (21) can be divided into

$$\underbrace{\left(\phi_{21}^{(1)}\phi_{41}^{(2)}-\phi_{21}^{(2)}\phi_{41}^{(1)}\right)}_{\mathrm{TM}_{0p}\ \mathrm{mode}}\times\underbrace{\left(\phi_{12}^{(1)}\phi_{32}^{(2)}-\phi_{12}^{(2)}\phi_{32}^{(1)}\right)}_{\mathrm{TE}_{0p}\ \mathrm{mode}}=0\ . \tag{30}$$

Eq. (30) clearly proves that the TM and TE modes exist for $m=0$, although the coaxial waveguide is filled with lossy dielectrics. Since Eq. (21) is applicable to a general coaxial waveguide of any μ_n and ϵ_n, we can use Eq. (21) to analyze canonical waveguides, including the PEC circular and coaxial waveguides. For instance, when $\mu_n=\mu_0$ and $\epsilon_n=\epsilon_0$, the geometry shown in Fig. 1 becomes a PEC circular waveguide with a radius of $b+d$, and Eq. (21) is thus simplified to

$$\underbrace{\phi_{41}^{(1)}}_{\mathrm{TM\ mode}}\times\underbrace{\phi_{32}^{(1)}}_{\mathrm{TE\ mode}}=0. \tag{31}$$

Similarly, when $\mu_n=\mu_0$, $\epsilon_1\to\infty$, and $\epsilon_3=\epsilon_2$, the geometry in Fig. 1 is considered a PEC coaxial waveguide. Then, the dispersion equation in Eq. (21) reduces to that of a PEC coaxial waveguide as

$$\underbrace{\left(\phi_{11}^{(1)}\phi_{41}^{(2)}-\phi_{11}^{(2)}\phi_{41}^{(1)}\right)}_{\mathrm{TM\ mode}}\times\underbrace{\left(\phi_{12}^{(1)}\phi_{32}^{(2)}-\phi_{12}^{(2)}\phi_{32}^{(1)}\right)}_{\mathrm{TE\ mode}}=0. \tag{32}$$

III. Numerical Computations

We used Davidenko's method [10, 11] to search a complex root β by equating $|\mathbf{\Phi}_m(\beta)|=0$ as shown in Eq. (21). Davidenko's method in [11] uses the fourth-order Runge–Kutta method and the Newton–Raphson method in the complex domain, which is suitable for searching the complex propagation constant β. An iterative update equation for the next approximate solution β_{n+1} is given by

$$\beta_{n+1}=\beta_n+\Delta\beta_{n+1}\ , \tag{33}$$

where β_n is the current approximate value for β and $\Delta\beta_{n+1}$ is defined in [11, Eq. (10)]. The next differential step $\Delta\beta_{n+1}$ is computed using β_n, $\Delta\beta_n$, and h, where β_0 and $\Delta\beta_0$ are the initial value and step for root searching, respectively, and h is a fixed step of the Runge–Kutta method. As n increases very steeply, β_{n+1} stably converges to β [10, 11]. We set $h=1$ and $\Delta\beta_0={}^{\beta_0}/_{100}$ for all root-searching computations.

The TM_{01}-mode dispersion results of the lossy coaxial waveguide are shown in Fig. 3 using $m=0$ and $f=100$ GHz, where the TM_{01} mode ($m=0$) is a dominant quasi-TEM mode. We assume that regions (I) and (III) are filled with lossy conductors using $\epsilon_1=\epsilon_3=\epsilon_0\left(1+i\frac{\sigma}{\omega\epsilon_0}\right)$, where σ denotes the electrical conductivity of a lossy dielectric. Using Eq. (30) and the conductor condition ($|\epsilon_1|\gg1$, $|\epsilon_3|\gg1$), we obtain an approximate dispersion relation for the TM_{0p} mode as

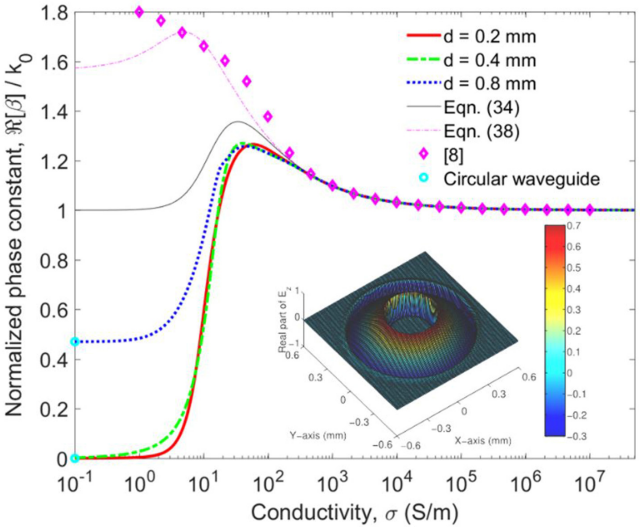

(a)

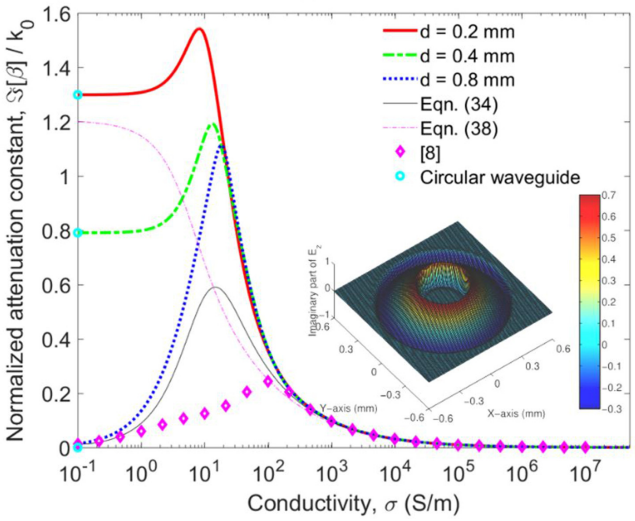

(b)

Fig. 3. Complex dispersion relation versus electrical conductivity σ for the TM_{01} mode in the lossy coaxial waveguide using $m=0$, $f=100$ GHz, $2a=0.434$ mm, $2b=1$ mm, $\mu_n=\mu_0$, $\epsilon_1=\epsilon_3=\epsilon_0\left(1+i\frac{\sigma}{\omega\epsilon_0}\right)$, and $\epsilon_2=\epsilon_0$: (a) phase constant $\Re[\beta]$ and (b) attenuation constant $\Im[\beta]$.

$$iU_0(v_2)-P_3U_0'(v_2)+P_1V_0(v_2)\approx0, \tag{34}$$

where $P_n={}^{\epsilon_2\kappa_n}/_{\epsilon_n\kappa_2}$,

$$U_m(v)=J_m(u_2)N_m(v)-N_m(u_2)J_m(v), \tag{35}$$

$$V_m(v)=J_m'(u_2)N_m(v)-N_m'(u_2)J_m(v). \tag{36}$$

Note that setting $U_m(v_2)$ and $V_m'(v_2)$ equal to zero yields

the TM_{mp}- and TE_{mp}-mode dispersion relations of an ideal coaxial line, respectively, where the subscript mp means that m and p are the numbers of field variations in the ϕ- and ρ-directions, respectively. This property indicates that Eq. (34) is a perturbed but accurate solution for the lossy coaxial waveguide when P_1 and P_3 are very small owing to $|\epsilon_1| \gg 1$ and $|\epsilon_3| \gg 1$. Utilizing $\beta \approx k_2$, $|k_1| \gg |\beta|$, and $|k_3| \gg |\beta|$, Eq. (34) can be further simplified to

$$\kappa_2 \approx i\epsilon_2 \frac{\frac{\kappa_1}{\epsilon_1}V_0(v_2) - \frac{\kappa_3}{\epsilon_3}U_0'(v_2)}{U_0(v_2)} \approx \frac{ik_2^2}{\mu_2} \frac{\frac{\mu_1}{k_1}N_0'(u_2) + \frac{\mu_3}{k_3}N_0'(v_2)}{N_0(u_2) - N_0(v_2)} , \quad (37)$$

when $u \to 0$, $N_0(u)$ and $N_0'(u)$ become $\frac{2}{\pi}\ln\left(\frac{u}{2}\right)$ and $\frac{2}{\pi u}$, respectively. Therefore, an approximate closed-form solution for Eq. (37) is finally obtained as

$$\beta \approx k_2 \sqrt{1 + \frac{i}{\mu_2 \ln\frac{b}{a}}\left(\frac{\mu_1}{k_1 a} + \frac{\mu_3}{k_3 b}\right)} . \quad (38)$$

Note that Eq. (38) is identical to [7, Eq. (37)] even though the boundary conditions for the outer conductors are different from each other. When $\mu_n = \mu_0$ and $\sigma \gg 1$, Eq. (38) becomes a complex propagation constant [5] obtained by the transmission line theory and penetration depth δ_s. Fig. 3 clearly indicates that the thickness (d) of an outer conductor hardly affects complex dispersion relations for $\sigma \geq 10^3$ S/m and $d \geq 0.2$ mm $\approx 4\delta_s$, where $\delta_s \approx 50$ μm and $\sigma = 10^3$ S/m. A comparison with [8] provides a favorable agreement when $\sigma \geq 10^3$ S/m. This is because [8] assumes an infinite outer conductor ($d \to \infty$) and the effects of the thick outer conductor are negligible for high electrical conductivity, where the outer conductor shown in Fig. 1 has finite thickness (d), which differs from [8]. As is also shown in Fig. 3, Eqs. (34) and (38) are practically good formulas in lieu of Eq. (21) for $\sigma \geq 10^3$ S/m. When σ approaches zero, Eq. (31) predicts that β becomes that of a PEC circular waveguide denoted as ○ in Fig. 3. The insets in Fig. 3 illustrate the normalized real and imaginary parts of the E_z-field distributions when $\sigma = 10^4$ S/m and $\beta \approx 2161.77 + 65.96i$ rad/m. The real and imaginary E_z-fields of the TM_{01} mode are continuous across the boundaries at $\rho = a$ and b, thus verifying that Davidenko's method in Eq. (33) is effective for searching the complex root β of a lossy coaxial waveguide. In addition, the magnitude of the E_z-fields is rapidly attenuated within lossy dielectrics in regions (I) and (III), and thus their field distributions illustrate the behaviors of the penetration depth very well.

Fig. 4 shows the dispersion behaviors of the TM_{01}, TE_{01}, and EH_{11} modes in the lossy coaxial waveguide versus microwave frequency. The TM_{01} mode has the lowest attenuation when compared with the TE_{01} and EH_{11} modes, thus indicating that the TM_{01} mode is a dominant mode irrespective of σ. Applying Eq. (30) and the conductor condition ($|\epsilon_1| \gg 1$, $|\epsilon_3| \gg 1$) yields an approximate dispersion equation for the TE_{0p} mode as

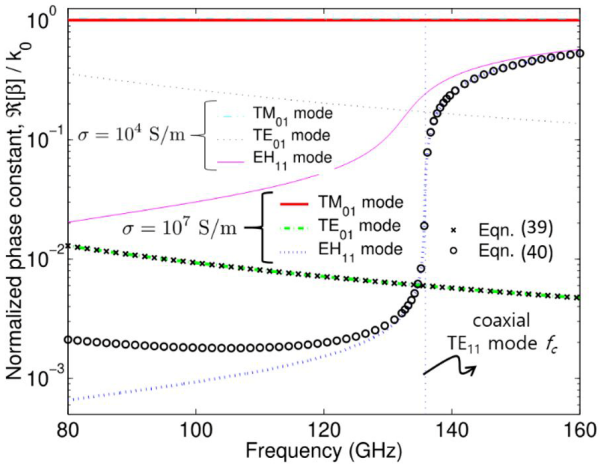

(a)

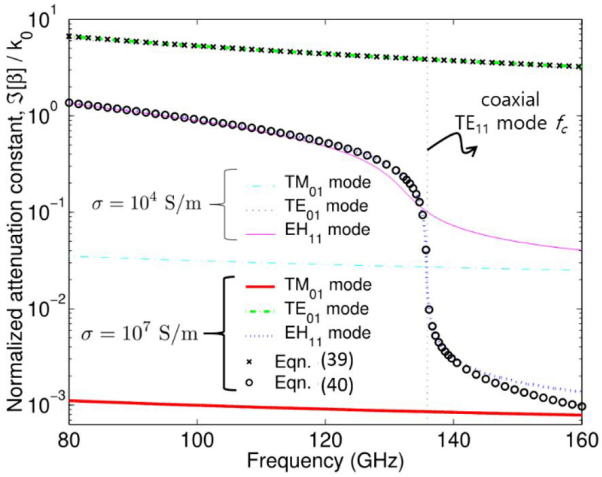

(b)

Fig. 4. Microwave behaviors of complex dispersion relations of multiple modes in the lossy coaxial waveguide using m = 0 or 1, d = 0.4 mm, and the same parameters given in the caption of Fig. 3. The coaxial TE_{11}-mode cutoff frequency (f_c) is computed using an ideal coaxial line: (a) phase constant $\Re[\beta]$ and (b) attenuation constant $\Im[\beta]$.

$$iV_0'(v_2) + Q_3V_0(v_2) - Q_1U_0'(v_2) \approx 0 , \quad (39)$$

where $Q_n = {\mu_n\kappa_2}/{\mu_2\kappa_n}$. Similar to Eqs. (34) and (39), the dispersion relation Eq. (21) approximately reduces to

$$\underbrace{[iU_m(v_2) - P_3U_m'(v_2) + P_1V_m(v_2)]}_{\mathrm{HE}_{mp}\ \mathrm{mode}} \times \underbrace{[iV_m'(v_2) + Q_3V_m(v_2) - Q_1U_m'(v_2)]}_{\mathrm{EH}_{mp}\ \mathrm{mode}} \approx 0 . \quad (40)$$

When $\sigma \geq 10^7$ S/m, the magnitude of ϵ_1 and ϵ_3 becomes very high and thus the TE_{01}- and EH_{11}-mode β computed by Eqs. (39) and (40) agree well with more precise solutions obtained by Eqs. (30) and (21), respectively. In Fig. 4, the attenuation constant ($\Im[\beta]$) of the EH_{11} mode rapidly decreases above $f_c \approx 135.9$ GHz. Therefore, the TM_{01} and EH_{11} modes coexist and propagate along the lossy coaxial waveguide above f_c. Considering Eq. (40), the cutoff frequency (f_c) of the lossy EH_{11} mode can be approximately determined using $V_1'(v_2) \approx 0$, which is related to f_c of the TE_{11} mode in an ideal coaxial line. The vertical dotted lines as shown in Fig. 4 denote f_c of the coaxial TE_{11} mode.

Fig. 5 illustrates the dispersion characteristics of the TM_{01} and EH_{11} modes within the visible spectrum. To theoretically obtain the dispersion relations of the lossy coaxial waveguide composed of real metals, we use optical dielectric constants [12] of silver (Ag), copper (Cu), and gold (Au). In the visible spectrum, the real part of the metal permittivity is usually negative caused by plasma oscillation in the metal. Fig. 5 indicates that Eq. (38) is valid within the optical spectrum and the cutoff or transition wavelength (λ_c) can be obtained by Eq. (40). As a result, our approximate solutions obtained from Eqs. (38) and (40) are useful for predicting the optical behaviors of the TM_{01} and EH_{11} modes in the nanoscale coaxial waveguide.

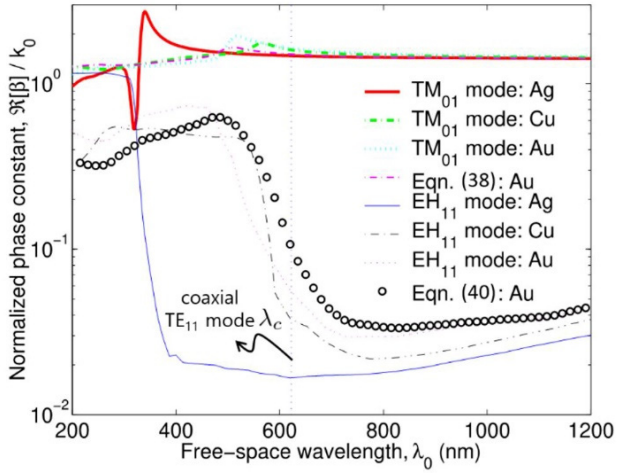

(a)

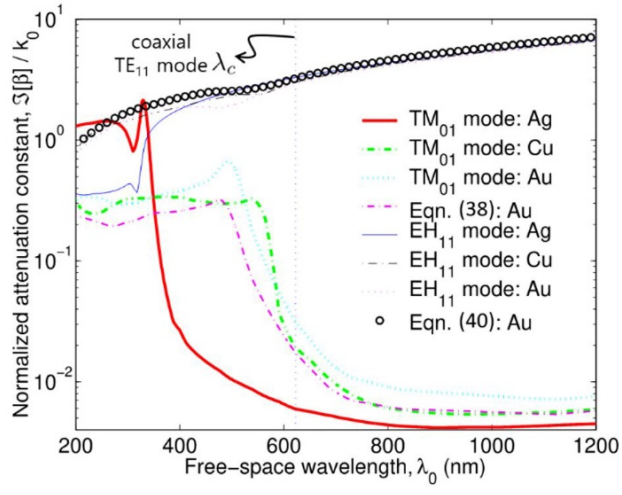

(b)

Fig. 5. Optical behaviors of complex dispersion relations of silver (Ag), copper (Cu), and gold (Au) coaxial waveguides using $m = 0$ or 1, $a = 75$ nm, $b = 125$ nm, and $d = 100$ nm, $\mu_n = \mu_0$, $\epsilon_2 = \epsilon_0$, and ϵ_1 and ϵ_3 ($\epsilon_1 = \epsilon_3$) are determined by optical dielectric constants of metals: (a) phase constant $\Re[\beta]$ and (b) attenuation constant $\Im[\beta]$.

IV. Conclusion

Analytical hybrid-mode dispersion relations of the lossy coaxial waveguide are presented based on the mode-matching technique and the vector potential formulations. Precise phase and attenuation constants of the TM_{01}, TE_{01}, and EH_{11} modes have been numerically evaluated using the root-searching algorithm based on Davidenko's method. Approximate but accurate dispersion equations for the TM_{0p}, TE_{0p}, EH_{mp}, and HE_{mp} modes are also proposed and agree well with more rigorous dispersion relations even for low electric conductivity or negative permittivity. Our dispersion solutions can be applied to the theoretical evaluation of a coaxial calibration kit or the analytical determination of light distribution within the optical coaxial waveguide.

This work was supported by the research fund of Mokwon University in 2019 and conducted at the Center for Electromagnetic Metrology, Korea Re-search Institute of Standards and Science (KRISS), Daejeon, Korea.

References

[1] M. Ibanescu, Y. Fink, S. Fan, E. L. Thomas, and J. D. Joannopoulos, "An all-dielectric coaxial waveguide," *Science*, vol. 289, no. 5478, pp. 415–419, 2000.

[2] F. I. Baida, A. Belkhir, D. Van Labeke, and O. Lamrous, "Subwavelength metallic coaxial waveguides in the optical range: role of the plasmonic modes," *Physical Review B*, vol. 74, no. 20, article no. 205419, 2006.

[3] B. Rizal, J. M. Merlo, M. J. Burns, T. C. Chiles, and M. J. Naughton, "Nanocoaxes for optical and electronic devices," *Analyst*, vol. 140, pp. 39–58, 2015.

[4] J. Y. Kwon, J. S. Kang, D. J. Lee, and J. H. Kim, "Analysis of a stepped air line using an air line simulator," *MAPAN*, vol. 27, no. 2, pp. 105–111, 2012.

[5] C. Cho, J. S. Kang, J. G. Lee, and H. Koo, "Characterization of a 1 mm (DC to 110 GHz) calibration kit for

VNA," *Journal of Electromagnetic Engineering and Science*, vol. 19, no. 4, pp. 272–278, 2019.

[6] R. DeVore, J. F. Toth, and R. Caldecott, "Dielectric coaxial waveguide," *Journal of Applied Physics*, vol. 44, no. 10, pp. 4488–4500, 1973.

[7] W. C. Daywitt, "Exact principal mode field for a lossy coaxial line," *IEEE Transactions on Microwave Theory and Techniques*, vol. 39, no. 8, pp. 1313-1322, 1991.

[8] W. C. Daywitt, "The propagation constant of a lossy coaxial line with a thick outer conductor," *IEEE Transactions on Microwave Theory and Techniques*, vol. 43, no. 4, pp. 907-911, 1995.

[9] H. J. Eom, *Electromagnetic Wave Theory for Boundary-Value Problems: An Advanced Course on Analytical Methods.* Berlin, Germany: Springer-Verlag, 2004.

[10] H. A. N. Hejase, "On the use of Davidenko's method in complex root search," *IEEE Transactions on Microwave Theory and Techniques*, vol. 41, no. 1, pp. 141–143, 1993.

[11] Y. H. Cho and D. H. Kwon, "Efficient analytical evaluation of complex dispersion relations of a multiple-row periodic array of magnetodielectric circular cylinders," *IEEE Transactions on Antennas and Propagation*, vol. 66, no. 5, pp. 2449–2457, 2018.

[12] S. Babar and J. H. Weaver, "Optical constants of Cu, Ag, and Au revisited," *Applied Optics*, vol. 54, no. 3, pp. 477–481, 2015.

Yong Heui Cho

received his B.S. degree in electronics engineering from Kyungpook National University, Daegu, Korea in 1998, and his M.S. degree and Ph.D. in electrical engineering from the Korea Advanced Institute of Science and Technology (KAIST), Daejeon, Korea in 2000 and 2002, respectively. From 2002 to 2003, he was Senior Research Staff with the Electronics and Telecommunications Research Institute (ETRI), Daejeon, Korea. In 2003, he joined the School of Information and Communication Engineering, Mokwon University, Daejeon, Korea, where he is currently a professor. From 2011 to 2012, he was a visiting professor with the Department of Electrical and Computer Engineering, University of Massachusetts Amherst, Amherst, MA, USA. From 2019 to 2020, he was a visiting researcher with the Center for Electromagnetic Metrology, Korea Research Institute of Standards and Science (KRISS), Daejeon, Korea. His current research interests include electromagnetic wave theory and scattering, numerical analysis, design of reflectarrays, and dispersion characteristics of transmission lines.

JOURNAL OF ELECTROMAGNETIC ENGINEERING AND SCIENCE, VOL. 21, NO. 2, 126~133, APR. 2021

https://doi.org/10.26866/jees.2021.21.2.126
ISSN 2671-7263 (Online) · ISSN 2671-7255 (Print)

A Uniform Heating Technique for Cavity in Volatile Organic Compound (VOC) Removal System Using Slotted Waveguide Array

Taewoo Yu[1] · Hyunwook Lee[2] · Sang-Jun Park[2] · Sangwook Nam[1,*]

Abstract

In this study, two types of slotted waveguide are designed in the frequency of 2.45 GHz to improve the microwave heating uniformity of a quadrangular prism-shaped cavity in a volatile organic compound (VOC) removal system. Both types adopt the equivalent circuit approach used for a waveguide slot array antenna. The difference between the two types is the slot impedance extraction method of the waveguide slot array: one calculates the impedance taking the cavity structure into account and the other finds it in free space. Both methods show that the heating uniformity is improved by 52% compared with that of the conventional horn-type feeding structure system according to the simulation results. Even though there is no difference in the heating uniformity between the two models, it is confirmed that the slotted waveguide array feeding model designed by using the impedance data of the slot incorporating the cavity ($SAWFM_{cavity}$) has about 6.35 dB better impedance matching characteristics than the other model designed by extracting the impedance data of the slot in free space ($SAWFM_{free}$). Also, it is found that the $SAWFM_{cavity}$ shows more stable impedance characteristics with respect to the loading condition than the $SAWFM_{free}$. Therefore, it is concluded that the impedance of the slot should be extracted taking the cavity into account for the design of the slotted waveguide feeding structure since it improves the reflection characteristic as well as the heating uniformity compared with the horn-type feeding structure.

Key Words: Cavity, Heating Uniformity, Impedance Matching, Power Loss Density Distribution, Slotted Waveguide.

I. Introduction

Microwave heating has been used for a long time in commercial and industrial applications owing to its heating efficiency. A typical example of a heating method using microwaves is a microwave oven at home. It is also used industrially in various fields such as soil moisture removal, volatile organic compound (VOC) removal, disinfection, and sterilization [1–3].

VOCs such as toluene and xylene inevitably occur in many industrial facilities, including semiconductor processing plants, refineries, and shipyards [4]. To prevent environmental pollution and human hazards, VOCs should be filtered by VOC filters. The confinement process of VOCs through filters is called adsorption. Owing to their volatility, the filters used for VOC adsorption can be recycled through microwave heating, and the desorbed VOCs can be separated by an air intake system. This process is called desorption. The adsorption and desorption processes are sequentially performed in separate spaces. To regenerate the VOC filter well, high energy efficiency and heating uniformity are required during desorption.

Manuscript received July 7, 2020 ; Revised October 26, 2020 ; Accepted December 8, 2020. (ID No. 20200707-099J)
[1]Department of Electronic and Computer Engineering, INMC, Seoul National University, Seoul, Korea.
[2]Department of MW Project Team, ECOPRO Co. Ltd., Cheongju, Korea.
[*]Corresponding Author: Sangwook Nam (e-mail: snam@snu.ac.kr)

Since most microwave heating systems are high-power applications, the shielding is very important, and thus, a cavity structure is frequently used. In addition, to avoid dielectric breakdown, the microwave feeding structure often uses a waveguide aperture type composed of a single conductor. For example, a VOC removal facility using a cavity fed by a horn-type microwave feeding structure is suggested [5].

In general, much care is needed for the design of the feeding structure of a cavity since many modes exist inside the cavity as determined by the cavity structure, and the excitation of the mode is dependent on the feeding structure. Many research studies related to this have been actively conducted [6–12]. The optimization process for improving the electric field's uniformity by analyzing the modes existing in the cavity and expressing the electric field inside the cavity in a linear combination of the modes has been presented [6]. However, modal analysis in a cavity and finding the feeding structure are very difficult because the cavity structures have different characteristics. Another method proposed for improving the uniformity is to use multiple microwave sources with sequential feeding [7]. However, using multiple sources has the disadvantages of system complexity and higher cost. The other method of increasing the uniformity is to employ a mode stirrer to mix multiple electromagnetic modes in the cavity, and parametric studies with a genetic algorithm for a dielectric multilayer in a rectangular cavity were suggested [8, 9]. Nevertheless, the mode stirrer itself is an extra structure that makes the system complicated, and the parametric studies with a genetic algorithm are also difficult to analyze.

There are studies in which dielectric slabs are uniformly heated using a slotted waveguide structure, and studies in which the heating uniformity is improved by using multiple slotted waveguides in a rectangular cavity [10–12]. Unlike the methods introduced earlier, these feeding structures can have the effect of generating multiple microwave sources with a single excitation port in a simple design method. However, the technique was used for heating a dielectric slab and the rectangular cavity only.

In this study, two types of slotted waveguide feeding structures are designed for the uniform heating of a VOC absorbent material in a quadrangular prism-shaped cavity used in a VOC removal facility. This paper is organized as follows. The entire VOC removal system, the cavity structure, and the basic horn-type feeding structure are introduced in Section II. In Section III, the basic theory of waveguide slot and the design method of the two types of slotted waveguide feeding structures are presented. In Section IV, the figure of merit of heating uniformity used in this study is presented, and the comparison result of the heating uniformity performance among the horn-type and the two types of slotted waveguide feeding structures is introduced. The impedance matching characteristics are compared and the load sensitivity is discussed in Section V, followed by the conclusion in Section VI.

II. Entire VOC Removal System and Horn-Type Feeding Structure

Fig. 1(a) shows the entire VOC removal system [4]. The total structure is a large metallic cylinder divided into several cylindrical wedge-shaped rooms, and the red part represents the air intake system. Each room is shielded with metal plates, and the upper and lower surfaces are composed of a metal perforated plate, which shields microwaves, but air can be inhaled. A VOC absorbent material (so-called VOC filter) is partially filled in each room, and microwaves are applied to each room to desorb VOC from the filter. The desorbed VOC is removed by the air intake system, and the system is rotated every certain time to remove the desorbed VOC in other spaces. Owing to the air intake system, microwaves cannot be fed from the top and bottom, but from the outer face of the system or sidewall of the cavity. Fig. 1(b) shows the quadrangular prism-shaped cavity structure for uniform heating used in this study, which is actually a piece of 16 room cavities arranged in circular form in the VOC removal system shown in Fig. 1(a). Table 1 shows the geometric parameters of the cavity. The cavity is partially filled with a dielectric material (VOC filter after adsorption) to be heated, the dielectric constant and loss tangent of which are 4.98 and 0.16, respectively.

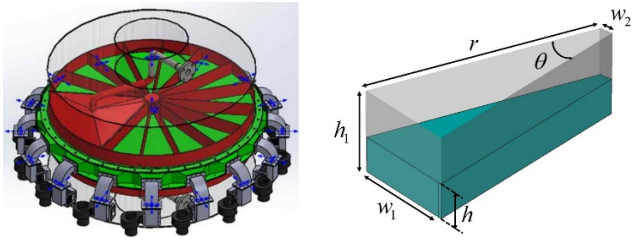

(a) (b)

Fig. 1. (a) Entire VOC removal system. (b) A piece of 16 cavities of the entire system (quadrangular prism-shaped cavity).

Table 1. Geometric parameters of the cavity

Parameter	Value
r (mm)	990.6
h_1 (mm)	350.0
h (mm)	150.0
w_1 (mm)	448.1
w_2 (mm)	58.2
θ (°)	22.5

Fig. 2 shows a piece of room cavity with the conventional horn-type feeding structure. In this study, two types of slotted waveguide are designed and attached at the sidewall of the cavity to improve the heating uniformity.

III. Two Types of Slotted Waveguide Design

The microwave source used for heating is a magnetron operating at 2.45 GHz. Therefore, the waveguide structure of WR340 (width = 86 mm, height = 43 mm) is selected. The first method (hereinafter, $SAWFM_{free}$) is to design the microwave feeding structure according to the well-known broad-wall resonant waveguide slot array (WSA) antenna design method. This method has been used for the uniform heating of a rectangular cavity [12].

Fig. 3(a) shows a longitudinal slot with an offset on a broad wall of a rectangular waveguide. The slot length is around $\lambda_0/2$ so that the slot shows a resonance characteristic. Specifically, this structure can be modeled as a shunt admittance element [13–15]. When the TE_{10} mode is excited in the waveguide, the normalized shunt admittance value can be calculated as

$$y = 2.09\frac{\lambda_g}{\lambda_0}\frac{a}{b}\cos^2\left(\frac{\pi\lambda_0}{2\lambda_g}\right)\sin^2\left(\frac{\pi d}{a}\right), \tag{1}$$

where λ_g is the guided wavelength in the waveguide [13].

Fig. 4 shows the broad-wall resonant single slot used in this study. Since the admittance value may vary depending on the thickness and width of the slot, a more accurate admittance value can be obtained through full wave simulation. In this study, the

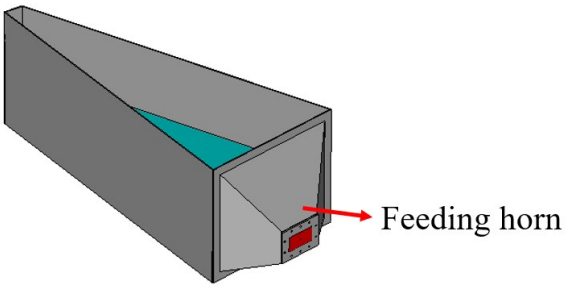

Fig. 2. Horn-type microwave excitation structure for the quadrangular prism-shaped cavity.

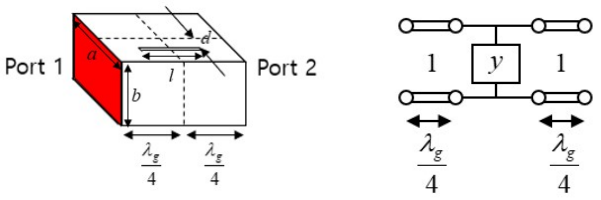

(a) (b)

Fig. 3. (a) Longitudinal slot on a broad wall of waveguide. (b) Equivalent circuit model of Fig. 2(a).

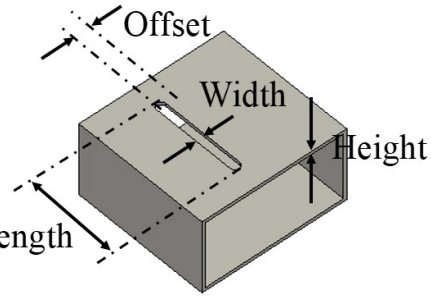

Fig. 4. Broad-wall resonant single slot.

slot width and height, shown in Fig. 4, are fixed to 6 mm and 5 mm, respectively. The normalized admittance value can be calculated as

$$y = \frac{\left((1-S_{11})^2 - S_{21}^2\right)}{2S_{21}}, \tag{2}$$

where the normalization factor is a wave impedance of the TE_{10} mode in the rectangular waveguide. The scattering parameters used in Eq. (2) are the data obtained by simulating the waveguide slot and de-embedding the $\lambda_g/4$ waveguide section on each port. The basic WSA antenna design method uses an equivalent circuit approach where the calculated shunt admittance elements representing broad-wall slots are connected by the transmission line representing the waveguide. For broadside radiation, the slot spacing is set to $\lambda_g/2$, and the offset direction of the adjacent slot is opposite to compensate the phase of the $\lambda_g/2$ waveguide section. The end of the waveguide is short, and the distance from the end to the last slot is $\lambda_g/4$ [13]. Fig. 5 shows the equivalent circuit model of the slotted waveguide structure, and the normalized input admittance can be calculated as

$$y_{in} = \sum_{k=1}^{n} y_k, \tag{3}$$

where y_k is the normalized admittance value of the kth slot. Considering the overall size of the cavity, the total number of slots is set to 10. Following the broad-side radiation WSA antenna design, the normalized shunt conductance and susceptance value are set close to 0.1 and 0, respectively. The waveguide center is placed at a distance of 235 mm from the floor of the system to

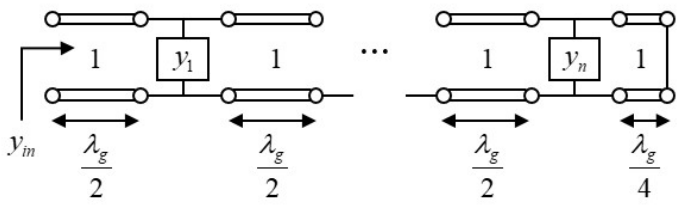

Fig. 5. Equivalent circuit model of slotted waveguide to be used as the feeding structure of the cavity.

avoid direct contact between the VOC absorbent dielectric and the slot. Fig. 6 shows the entire heating system with the slotted waveguide feeding structure, and Table 2 shows the normalized admittance value of each slot and the length and offset properties. The height of the centerline of the slot array and the position of the first slot (#1) are fixed to $z = 235$ mm and $y_1 = 42.08$ mm, respectively. Also, the quantity of the VOC absorbent material (loading) depends on the operational situation so that the height h is a variable in the range of 130 to 170 mm. The reference h is set to 150 mm, which is an intermediate value of the height range.

For $SAWFM_{free}$, the feeding structure is designed using the resonant broad-side WSA antenna design method in free space. However, as soon as the slotted waveguide structure is attached to the sidewall of the cavity, the calculated admittance property is changed by the cavity structure. After all, in order to find the correct admittance data of the slot attached to the cavity, the admittance properties have to be extracted including the effect of the cavity. The second method (hereinafter, $SAWFM_{cavity}$) is to extract admittance data of the slot including the effect of the cavity and to design the slotted waveguide feeding structure in the same way as the approach in $SAWFM_{free}$. In this case, two slots having the same length and offset have different admittances, since the fields excited by the two slots are different depending on the position of the slot inside the cavity. Hence, the position of the slot should be considered as a variable. The height of the centerline of the slot array and the position of the first slot are the same as in the $SAWFM_{free}$ case. Fig. 7 shows the extracted normalized admittance data with varying lengths and offsets of all slots. Since there are two variables, namely, the slot's length and offset, the admittance value is calculated by fixing one variable and changing the other variable. Fig. 7(a) and

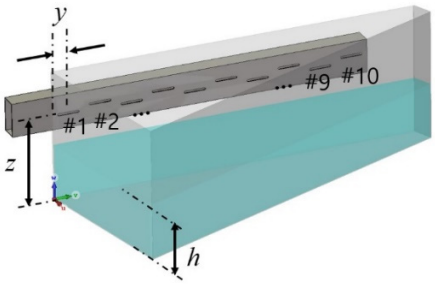

Fig. 6. A 3D model of the system with the slotted waveguide feeding structure: $z = 235$ mm, $y_1 = 42.08$ mm, $h = 150$ mm.

Table 2. Normalized shunt admittance values at 2.45 GHz and slot's properties ($SAWFM_{free}$)

Slot	Normalized admittance	Properties (mm)	
		Offset	Length
1–10	$0.1026 + j\,0.0006$	8.4	57.7

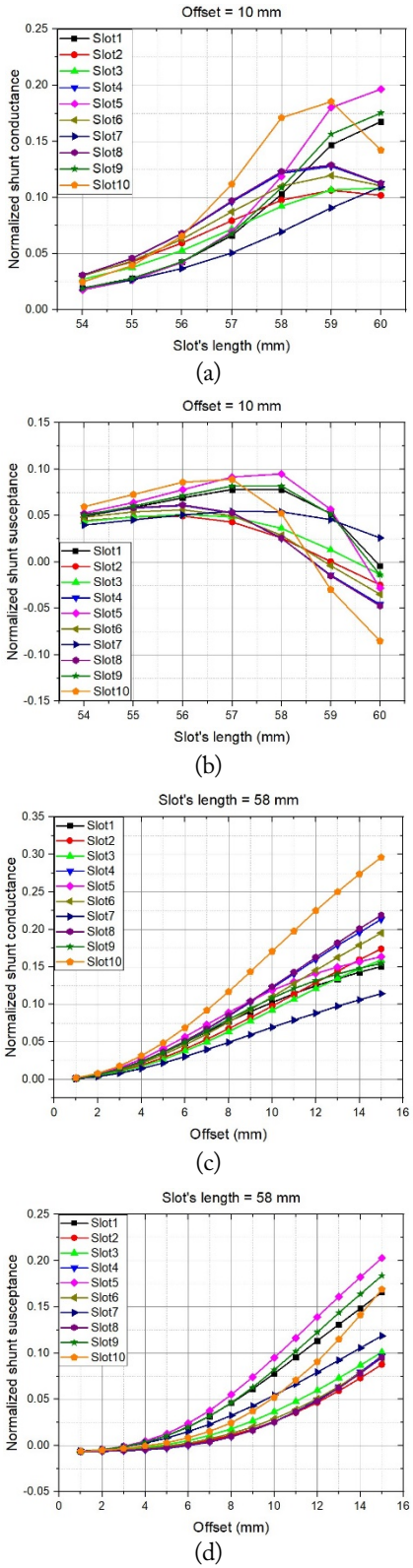

Fig. 7. Extracted normalized shunt admittance ($SAWFM_{cavity}$): (a) normalized shunt conductance with respect to the slot's length (Offset = 10 mm), (b) normalized shunt susceptance with respect to the slot's length (Offset = 10 mm), (c) normalized shunt conductance with respect to the slot's offset (Length = 58 mm), and (d) normalized shunt susceptance with respect to the slot's offset (Length = 58 mm).

(b) show the normalized shunt conductance and susceptance, respectively, according to the length change when the slot's offset is fixed at 10 mm. Fig. 7(c) and (d) show the normalized shunt conductance and susceptance, respectively, according to the offset change when the slot's length is fixed at 58 mm. Notice that the admittance values are quite different depending on the slot's position as the slot length or offset is large. On the basis of the data in Fig. 7, a slight tuning is performed to match the normalized shunt admittance value of each slot similar to $SAWFM_{free}$. Table 3 shows the derived slot's properties of $SAWFM_{cavity}$.

IV. Uniform Heating Performance

In this study, to evaluate the heating uniformity performance of various feed structures, an evaluation index related to microwave is suggested. The heat generated in the dielectric is proportional to the power loss density (W/m^3) due to electromagnetic waves expressed as

$$P = (\sigma + \omega\varepsilon'')|\mathbf{E}|^2, \tag{4}$$

where σ and ε'' represent the conductivity of the VOC absorbent dielectric medium and the imaginary part of the dielectric constant, respectively [16]. Although heat transfer should also be considered, only thermal losses due to microwaves are considered in this study. On the basis of the power loss density distribution, the figure of merit for performance evaluation is set as

$$\sigma_{\text{nor}}(\mathbf{P}) = \frac{\sqrt{\frac{\sum_{i=1}^{N}\left(P_i - \overline{P}\right)^2}{N-1}}}{\overline{P}}, \tag{5}$$

N: Number of samples

P_i : Power loss density at the i-th sample

$\overline{P}$: Average value of power loss density

Table 3. Normalized shunt admittance values at 2.45 GHz and slot's properties ($SAWFM_{cavity}$)

Slot	Normalized admittance	Properties (mm)	
		Offset	Length
1	$0.1017 - j0.0011$	7.2	58.4
2	$0.0987 - j0.0029$	7.5	59.4
3	$0.0981 + j0.0076$	8.6	58.2
4	$0.0993 + j0.0066$	9.2	60.5
5	$0.0990 - j0.0024$	9.0	58.8
6	$0.0982 + j0.0005$	7.0	59.1
7	$0.1027 - j0.0012$	8.8	58.5
8	$0.0992 - j0.0001$	9.5	59.4
9	$0.0966 + j0.0030$	9.5	58.8
10	$0.1018 + j0.0006$	7.7	59.4

where $\sigma_{nor}(\mathbf{P})$ is the normalized standard deviation of power loss density in the material. To ensure the convergence of the calculation results, the field sampling interval is set to 7 mm, which is smaller than $\lambda_d/7$, where λ_d is the wavelength in the dielectric medium. The total number of field samples in the dielectric is about 100,000 in this example. To evaluate the heating uniformity of horn-type and proposed systems, full wave EM simulation (CST Microwave Studio) is performed on the conventional horn-type feeding structure and the two WSA models ($SAWFM_{free}$ and $SAWFM_{cavity}$).

Fig. 8 shows the power loss density distribution inside the dielectric medium. Fig. 8(a) and (b) show the results for the horn-type feeding structure. Fig. 8(c) and (d) are the results for $SAWFM_{free}$, and Fig. 8(e) and (f) are the results for $SAWFM_{cavity}$. It can be seen that the structure using the horn type has a strong power loss density distribution in the vicinity of the aperture. On the other hand, it can be seen that the power loss density distributions are relatively more uniform in the $SAWFM_{free}$ and $SAWFM_{cavity}$ cases than in the case of the horn-type structure. The normalized standard deviations are given in Table 4. It is confirmed that the slotted waveguide feeding structure improves the heating uniformity by about 52% compared with the existing horn-type feeding structure. In addition, notice that there is little difference (less than 1%) in heating uniformity between the two slotted waveguide models.

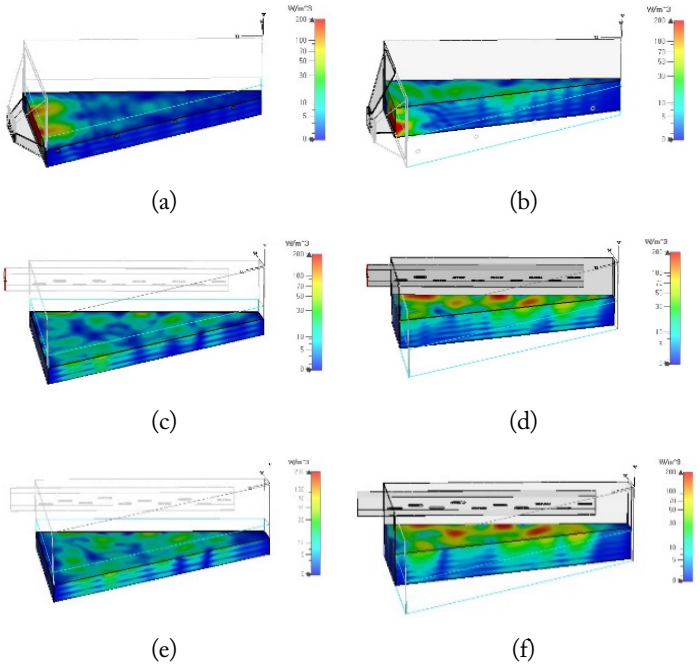

Fig. 8. Power loss density distribution in the material: (a) horn-type structure horizontal cut, (b) horn-type structure vertical cut, (c) $SAWFM_{free}$ structure horizontal cut, (d) $SAWFM_{free}$ structure vertical cut, (e) $SAWFM_{cavity}$ structure horizontal cut, and (f) $SAWFM_{cavity}$ structure vertical cut.

Table 4. Comparison of uniform heating performance

Structure	Average power loss density (W/m^3)	Normalized standard deviation
Horn type	11.70	2.62
SAWFM$_{free}$	12.70	1.25
SAWFM$_{cavity}$	13.50	1.26

V. Impedance Matching Characteristics

Fig. 9 shows the impedance matching characteristics of the three systems. The reflection coefficient characteristic for $S(1,1)$ is usually required to be lower than −10 dB. The return loss is larger than 10 dB for both designs to satisfy the impedance matching requirement. However, in the case of heating facilities using microwaves, it is better to make the reflection as small as possible (for example, $S(1,1) \leq 13$ dB corresponding to less than 5% reflection) for energy-efficient operation. To meet the conditions, an external matching circuit such as a waveguide stub tuner should be additionally attached for the horn type and SAWFM$_{free}$. In the case of SAWFM$_{cavity}$, it is possible to obtain excellent impedance matching characteristics at a center frequency of 2.45 GHz without additional impedance matching circuits. This is because a more accurate impedance matching is possible since the calculation of the normalized admittance value of each slot includes the cavity.

Generally, the resonance-based WSA antenna has very narrow band characteristics. Therefore, when it is used as the feeding structure in an industrial microwave heating facility, it may have characteristics that are very sensitive to internal load changes (e.g., dielectric constant, height, etc.). Even though the impedance matching can be obtained through the external matching circuit, the tuner has to be adjusted whenever the internal condition of the cavity changes.

Fig. 10(a) and (b) show the impedance matching characteristics according to the loading of VOC absorbent for SAWFM$_{free}$ and

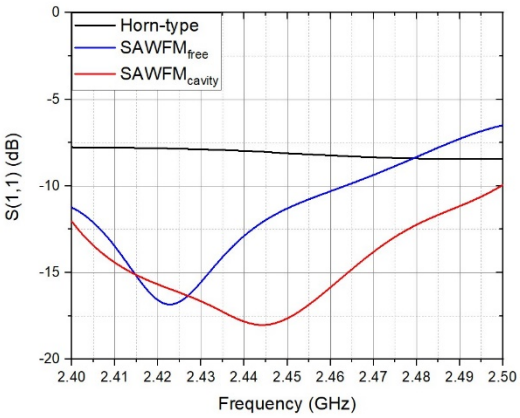

Fig. 9. Impedance matching characteristics.

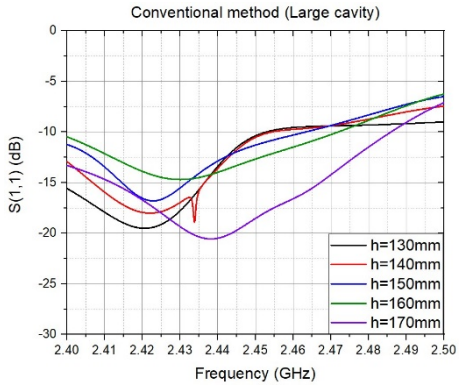

(a)

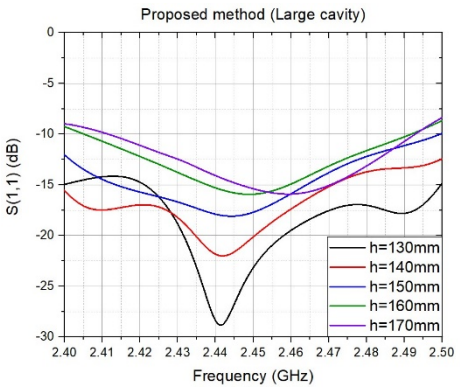

(b)

Fig. 10. Impedance matching characteristics with changing internal load condition (reference dielectric height $h = 150$ mm): (a) SAWFM$_{free}$ and (b) SAWFM$_{cavity}$.

SAWFM$_{cavity}$, respectively. The height of the VOC absorbent material inside the cavity varies from 130 to 170 mm with 10 mm intervals. In both models, the reference dielectric height is 150 mm. In the case of SAWFM$_{free}$, it can be seen that the impedance matching characteristic deteriorates to −10 dB depending on the change in dielectric height. However, in the case of SAWFM$_{cavity}$, it can be seen that the impedance matching characteristic is maintained below −15 dB despite the dielectric height change, and it can be stably operated without manipulating an external matching circuit according to a change of the load in the cavity.

VI. Conclusion

In this study, two types of slotted waveguide array in the frequency of 2.45 GHz are designed to improve the heating uniformity of the quadrangular prismatic microwave cavity used for a VOC removal system. Both follow the equivalent circuit approach of the WSA antenna design. The difference is whether the cavity is included when extracting the impedance data of the slot. Both methods confirm that the heating uniformity is improved by 52% compared with the conventional horn-type excitation case, and the uniformity difference between the two

models is below than 1%. However, the model using the impedance data of the slot including the cavity has been found to have better impedance matching by 6.35 dB and shows better load-insensitive characteristics than the model designed by extracting the impedance data of the slot in the free space. As a result, the impedance value of the slot should be extracted taking the cavity effect into account for the design of the slotted waveguide feeding structure that improves the reflection and load-insensitive characteristics while improving the heating uniformity compared with the horn-type feeding structure.

This work was supported by Business for Cooperative R&D between Industry, Academy, and Research Institute funded Korea Small and Medium Business Administration in 2018 and the BK21 Plus program of the Creative Research Engineer Development for IT, Seoul National University in 2020 (No. C0527861).

References

[1] A. C. Metaxas, "Microwave heating," *IET Power Engineering Journal*, vol. 5, no. 5, pp. 237–247, 1991.

[2] J. M. Osepchuk, "A history of microwave heating applications," *IEEE Transactions on Microwave Theory and Techniques*, vol. 32, no. 9, pp. 1200–1224, 1984.

[3] R. J. Meredith, *Engineers' Handbook of Industrial Microwave Heating*. London, UK: Institution of Electrical Engineers, 1998.

[4] F. I. Khan and A. K. Ghoshal, "Removal of volatile organic compounds from polluted air," *Journal of Loss Prevention in the Process Industries*, vol. 13, no. 6, pp. 527–545, 2000.

[5] S. J. Yoon, J. S. Min, J. Y. Kim, S. J. Park, Y. K. Han, J. Y. Choi, N. U. Cho, and S. G. Moon, "System for removing VOCs using gas distribution plate," Korea Patent 10-2017-0105033, July 2017.

[6] D. Neumaier, S. Sanseverino, G. Link, and J. Jelonnek, "Homogeneous dielectric heating in large microwave ovens by excitation of multiple eigenmodes at their resonance frequencies," in *Proceedings of the 17th International Conference on Microwave and High Frequency Heating (AMPERE)*, Valencia, Spain, 2019, pp. 166–173.

[7] S. H. Bae, M. G. Jeong, J. H. Kim, and W. S. Lee, "A continuous power-controlled microwave belt drier improving heating uniformity," *IEEE Microwave and Wireless Guided Wave Letters*, vol. 27, no. 5, pp. 527–529, 2017.

[8] D. A. Hill, "Electronic mode stirring for reverberation chambers," *IEEE Transactions on Electromagnetic Compatibility*, vol. 36, no. 4, pp. 294–299, 1994.

[9] E. Dominguez-Tortajada, J. Monzo-Cabrera, and A. Diaz-Morcillo, "Uniform electric field distribution in microwave heating applicators by means of genetic algorithms optimization of dielectric multilayer structures," *IEEE Transactions on Microwave Theory and Techniques*, vol. 55, no. 1, pp. 85–91, 2007.

[10] V. Castrillo, G. D'Ambrosio, R. Massa, F. Chiadini, V. Fiumara, A. Scaglione, G. Panariello, and I. M. Pinto, "Improved design of waveguide slot array applicators for microwave heating," *Materials Research Innovations*, vol. 8, no. 2, pp. 71–74, 2004.

[11] A. A. Barba, D. Acierno, and M. d'Amore. "Use of microwaves for *in-situ* removal of pollutant compounds from solid matrices," *Journal of Hazardous Materials*, vol. 207, pp. 128–135, 2012.

[12] S. Ahn, C. Jeong, D. Lim, and W. Lee, "Kilowatt-level power-controlled microwave applicator with multiple slotted waveguides for improving heating uniformity," *IEEE Transactions on Microwave Theory and Techniques*, vol. 68, no. 7, pp. 2867–2875, 2020.

[13] R. E. Collin, *Antennas and Radiowave Propagation*. New York, NY: McGraw-Hill, 1985, pp. 265–273.

[14] A. F. Stevenson, "The theory of slots in rectangular waveguides," *Journal of Applied Physics*, vol. 19, no. 1, pp. 24–38, 1948.

[15] A. A. Oliner, "The impedance properties of narrow radiating slots in the broad face of rectangular waveguide: Part I. theory," *IRE Transactions on Antennas and Propagation*, vol. 5, no. 1, pp. 4–11, 1957.

[16] A. C. Metaxas, *Industrial Microwave Heating*. London, UK: Institution of Electrical Engineers, 1983, pp. 5–11.

Taewoo Yu

received his B.S. degree in electronic and electrical engineering from Hongik University, Seoul, Korea, in 2017. He is currently working toward an integrated master's and Ph.D. degree in the Department of Electrical and Computer Engineering at Seoul National University, Seoul, Korea. His main research interests are industrial microwave applicators and RF systems including wireless power transfer and radar systems.

Hyunwook Lee

received his B.S., M.S., and Ph.D. degrees, all in radio sciences and engineering, from Kwangwoon University, Seoul, Korea, in 2007, 2009, and 2015, respectively. From 2015 to 2018, he was an assistant professor at the Center for Integrated Smart Sensors (CISS) at the Korea Advanced Institute of Science and Technology (KAIST), Daejeon, Korea. From 2018, he has been a researcher at ECOPRO Co. Ltd., Cheongju, Korea. His research interests are industrial microwave applicators including VOC removal and dehumidification systems.

Sang-Jun Park

received his B.S. degree in chemical engineering from Donga University, Busan, Korea, in 2002, and M.S. degree in environmental engineering from Pohang University of Science and Technology in 2008. From 2012, he has been a researcher at ECOPRO Co. Ltd., Cheongju, Korea. Since 2018, he has been working toward Ph.D. degree in chemical engineering at Chungbuk University, Cheongju, Korea. His research interests are industrial microwave applicators including VOC removal and dehumidification systems.

Sangwook Nam

received his B.S. degree from Seoul National University, Seoul, Korea, in 1981, M.S. degree from Korea Advanced Institute of Science and Technology (KAIST), Seoul, Korea, in 1983, and Ph.D. degree from the University of Texas at Austin, Austin, TX, USA, in 1989, all in electrical engineering. From 1983 to 1986, he was a researcher at the Gold Star Central Research Laboratory, Seoul, Korea. Since 1990, he has been a professor at the School of Electrical Engineering and Computer Science, Seoul National University. His research interests include analysis/design of electromagnetic structures, antennas, and microwave active/passive circuits.

JOURNAL OF ELECTROMAGNETIC ENGINEERING AND SCIENCE, VOL. 21, NO. 2, 134~142, APR. 2021

https://doi.org/10.26866/jees.2021.21.2.134
ISSN 2671-7263 (Online) · ISSN 2671-7255 (Print)

Sea Clutter Covariance Matrix Estimation and Its Application to Whitening Filter

Sanghyun Choi[1] · Hoongee Yang[2,*] · Jimin Song[3] · Hyeonmu Jeon[4] · Jongmann Kim[5] · Yongseek Chung[2]

Abstract

The accurate estimation of clutter covariance matrix (CCM) is essential in designing a radar detector/filter to suppress sea clutter. This estimation might not be easily accomplished because of the scarcity of valid training vectors adjacent to the range cell under test (CUT). We propose a new CCM estimation algorithm that is derived by modeling time-series clutter returns into a clutter Doppler spectrum in the frequency domain and exploiting mutual independence among spectral components. To justify its excellence over the conventional sample covariance matrix (SCM) algorithm, we design two filters—a maximum signal-to-interference-plus-noise ratio (SINR)-based filter and a whitening filter—that use the estimated CCMs and compare their performance in a numerically simulated sea clutter scenario. Comparisons are made by showing the eigenvector spectra of the estimated CCMs and the frequency responses and outputs of the filters. Moreover, SINRs at the target Doppler bin are examined and compared with a theoretical, analytically derived SINR.

Key Words: Clutter Suppression, Covariance Matrix Estimation, Doppler Frequency, Whitening Filter.

I. Introduction

Detecting a low velocity, small target in sea clutter, especially with low-grazing angle radar, is an important subject in maritime reconnaissance. The existence of sea clutter has been acknowledged as one of the major obstacles that hinders successful target detection. An ideal detector can inherently estimate clutter statistics, such as the clutter covariance matrix (CCM), the clutter power of cell under test (CUT), and range cells adjacent to the CUT, on the fly and apply those parameters to its signal processing component to maintain a constant false alarm rate (CFAR) [1, 2].

It has been said that the stationarity of clutter returns is as short as 100 ms at most [3]. Moreover, because of the heterogeneity of the sea environment, there are not enough training vectors that share the same CCM structure as a primary data vector [4]. These will make it difficult to estimate the CCM and consequently suppress clutter returns.

Many studies have been conducted to investigate the statistical properties of sea clutter, either by analyzing measurement data or by theoretical analysis. The statistical properties include the modeling of Doppler spectra of clutter returns, the spatial and temporal correlation of speckle and texture, clutter amplitude probability density function related with shape parameter and scale parameter, etc. [5, 6]. It turns out that a compound-Gaussian model has been found to be the best fit for sea clutter, especially at a low-grazing angle and high-resolution radar [7].

A detection scheme that works by suppressing clutter returns

Manuscript received May 4, 2020 ; Revised August 21, 2020 ; Accepted December 15, 2020. (ID No. 20200504-060J)
[1]KOMPSAT Development Division, Korea Aerospace Industries Ltd., Sacheon, Korea.
[2]Department of Electronic Convergence Engineering, Kwangwoon University, Seoul, Korea.
[3]Department of Electronics & Software, Renault Samsung Motors, Yongin, Korea.
[4]Radar Research Institute, Hanwha Systems, Yongin, Korea.
[5]The 3rd R&D Institute, Agency for Defense Development, Daejeon, Korea.
[*]Corresponding Author: Hoongee Yang (e-mail: hgyang@kw.ac.kr)

has been developed through the exploitation of the statistical properties of sea clutter. The generalized likelihood ratio test (GLRT) detector, referred to as a normalized matched filter (NMF), was derived in Gaussian noise, assuming the CCM structure was known [8]. The adaptive GLRT detector structure using the estimated CCM was derived and demonstrated to ensure the CFAR property with respect to the CCM [1].

There have been many studies proposing subspace-based clutter suppression techniques. Mathematical tools such as orthogonal projection (OP), singular value decomposition (SVD), principle eigenvector, etc. were applied to the constructed clutter subspace [9, 10].

In adaptive detectors, the estimation of the CCM has been of paramount importance in determining clutter suppression performance. The CCM in the NMF was replaced by the estimate of the sample covariance matrix (SCM) or by the normalized sample covariance matrix (NSCM) to guarantee the CFAR property with respect to the CCM or to the statistics of the texture or clutter power [4, 11]. In [12], an eigen-analysis-based CCM estimation algorithm called the regularized estimation method was proposed, and it was accessed through the adaptive NMF. Through effectively setting regularization parameters, this method tackled the problem of the scarcity of training vectors. This problem has also been dealt with in the context of the space-time adaptive processing (STAP) algorithm. Knowledge-aided STAP algorithms were proposed in this context, utilizing a priori data for the clutter map rather than many training vectors [13, 14]. To adapt to a more heterogeneous environment, a single data set (SDS) STAP algorithm that does not use any training vectors was proposed [15].

In this paper, we propose a new CCM estimation algorithm that does not require many training vectors and compare it with the conventional SCM-based algorithm, paying attention to the performance variation, which depends on the number of training vectors.

This paper is organized as follows. In Section II-1, we present the modeling of the sea CCM using discrete Fourier transform (DFT). In Section II-2, we propose a new CCM estimation algorithm. To compare it with the conventional SCM, two filters—a maximum signal-to-interference-plus-noise ratio (SINR)-based filter and a whitening filter—using the CCM estimates are introduced and analyzed in Section III-1 and Section III-2. In Section IV, through numerical simulations, we review the performance of the proposed algorithm, showing the two filters' outputs. Finally, our conclusions are stated in Section V.

II. CCM Modeling and Estimation

1. Sea CCM Modeling

We consider a shipborne radar scenario where a radar makes N consecutive pulse transmissions and corresponding receptions during period T into a radar scene. To focus on sea CCM modeling, the target signature in the radar scene is neglected in this section.

Let $c_j[n]$ denote a clutter return of the jth range cell for the nth pulse. For N consecutive transmissions, we obtain the clutter return vector of the jth range cell, $\{c_j[n]\}(n = 0, 1, \cdots, N-1)$. Let $\{C_j[k]\}$ $\left(k = -\frac{N}{2}, \ldots, \frac{N}{2}-1\right)$ denote the DFT of $\{c_j[n]\}$, where k is related to Doppler frequency $f_k = \frac{k}{NT}$. According to [5], $C_j[k]$ is modelled as the product of two random variables: texture and speckle. Using the Wiener–Khinchin theorem, the DFT of the autocorrelation function of $c_j[n]$ corresponds to the clutter power spectral density (PSD), which is approximately $\mathrm{E}\left[\left|C_j(k)\right|^2\right]$. According to the DFT theory, $c_j[n]$ can be expressed as

$$c_j[n] = \sum_{k=-\frac{N}{2}}^{\frac{N}{2}-1} C_j[k] \exp\left[j\left(\frac{2\pi}{N}\right)kn\right] \tag{1}$$

Eq. (1) can be rewritten in vector notation as

$$\boldsymbol{c_j} = \sum_{k=-\frac{N}{2}}^{\frac{N}{2}-1} \gamma_{j,k}\sqrt{N}\boldsymbol{u}_k \tag{2}$$

where $\boldsymbol{c_j} \in \mathbb{C}^{N\times 1}$ denotes $\boldsymbol{c}_j \equiv \left[c_j[0], \ldots, c_j[N-1]\right]^{\mathrm{T}}$ (superscript T denotes transpose) and for notational simplicity, $r_{j,k}$ is used in place of $C_j[k]$. Meanwhile, $\boldsymbol{u}_k$ in Eq. (2) denotes

$$\boldsymbol{u}_k = \frac{1}{\sqrt{N}}[e^{j\left(\frac{2\pi}{N}\right)k(0)}, \ldots e^{j\left(\frac{2\pi}{N}\right)k(n)} \ldots, e^{j\left(\frac{2\pi}{N}\right)k(N-1)}]^T \tag{3}$$

It is noted that $\boldsymbol{u}_k \in \mathbb{C}^{N\times 1}$ is, in fact, a Doppler steering vector of $f_k = \frac{k}{NT}$ with intensity $|\boldsymbol{u}_k| = 1$. The overall interference vector $\boldsymbol{v}_j$ can be expressed as

$$\boldsymbol{v}_j = \boldsymbol{c}_j + \boldsymbol{n}_j \tag{4}$$

where $\boldsymbol{n}_j$ is a complex additive white Gaussian noise vector. Using Eq. (2) and the statistical independence between $\boldsymbol{c}_j$ and $\boldsymbol{n}_j$, the theoretical covariance matrix for $\boldsymbol{v}_j$, i.e., $\boldsymbol{R}_j \in \mathbb{C}^{N\times N}$, is expressed as

$$\begin{aligned}\boldsymbol{R}_j &= E\left[\boldsymbol{v}_j\boldsymbol{v}_j^H\right] \\ &\cong \sum_{k=-\frac{N}{2}}^{\frac{N}{2}-1}\sum_{m=-\frac{N}{2}}^{\frac{N}{2}-1} E\left[\gamma_{j,k}\gamma_{j,m}^*\right](\sqrt{N}\,\boldsymbol{u}_k)(\sqrt{N}\boldsymbol{u}_m)^H \\ &+ E\left[\boldsymbol{n}_j\boldsymbol{n}_j{}^H\right].\end{aligned} \tag{5}$$

When manipulating Eq. (5), we use the orthogonality $\boldsymbol{u}_k \perp \boldsymbol{u}_m$ for $k \neq m$ and $\boldsymbol{u}_k \perp \boldsymbol{n}_j$. According to [16], a collection of random variables—namely, $\gamma_{j,k}$s—can be assumed to be mutually independent, having zero mean. That is,

$$\mathrm{E}\left[\gamma_{j,k}\gamma_{j,m}^{*}\right] = \delta_{k,m}\ E\left[\left|\gamma_{j,k}\right|^{2}\right] \tag{6}$$

where $\delta_{k,m}$ is the delta function defined as $\delta_{k,m} = 1$ for $k = m$ and $\delta_{k,m} = 0$ otherwise.

Using Eq. (6), Eq. (5) is further simplified as

$$\boldsymbol{R_j} \cong N \sum_{k=-\frac{N}{2}}^{\frac{N}{2}-1} \eta_{j,k}^{2}\boldsymbol{u}_k\boldsymbol{u}_k^{H} + \sigma^{2}\boldsymbol{I} \tag{7}$$

where $\eta_{j,k}^{2} = E\left[\left|\gamma_{j,k}\right|^{2}\right]$ is the clutter PSD at $f_k = \frac{k}{NT}$, σ^2 is noise variance, and $\boldsymbol{I}$ is the identity matrix.

$\boldsymbol{R_j}$ in Eq. (7) can be rewritten as the form of the eigen-decomposition, that is,

$$\boldsymbol{R}_j \cong \boldsymbol{U\Lambda}_j\boldsymbol{U}^{H} \tag{8}$$

where $\boldsymbol{U} = [\boldsymbol{u}_1\ \boldsymbol{u}_2\ \dots\ \boldsymbol{u}_N]$ is an $N\times N$ matrix whose columns are the eigenvectors of $\boldsymbol{R}_j$, and $\boldsymbol{\Lambda}_j = \mathrm{diag}\{\lambda_{j,1}\ \lambda_{j,2}\dots\lambda_{j,N}\}$ is a diagonal matrix in which $\lambda_{j,k} = N{\eta_{j,k}}^2 + \sigma^2$ is an eigenvalue corresponding to eigenvector $\boldsymbol{u}_k \in \mathbb{C}^{N\times 1}$.

2. Proposed Algorithm for CCM Estimation

Let $\widetilde{\boldsymbol{R}}_{\boldsymbol{j}}$ denote an estimate for $\boldsymbol{R}_j$ obtained by the SCM, which used to be a primary choice for CCM estimation. $\widetilde{\boldsymbol{R}}_{\boldsymbol{j}}$ is then expressed as

$$\widetilde{\boldsymbol{R}}_{\boldsymbol{j}} = \frac{1}{L}\sum_{l\neq j,\ l=j-\frac{L}{2}}^{j+\frac{L}{2}} \boldsymbol{v_l}\boldsymbol{v_l^H} \tag{9}$$

where L is the number of valid training vectors adjacent to the CUT and $\boldsymbol{v_l}$ is the interference vector at the lth range cell. Because of a finite number of training vectors, $\widetilde{\boldsymbol{R}}_{\boldsymbol{j}}$ cannot be ideally eigen-decomposed, as expressed in Eq. (8).

Let $\boldsymbol{z}_l$ be the DFT of $\boldsymbol{v}_l$. $\boldsymbol{z}_l$ can then be written as

$$\boldsymbol{z}_l = \frac{1}{\sqrt{N}}\boldsymbol{D}^{H}\boldsymbol{v_l}\ . \tag{10}$$

In Eq. (10), $\boldsymbol{D} = \frac{1}{\sqrt{N}}\left[\boldsymbol{d}_{-\frac{N}{2}},\ \boldsymbol{d}_{-\frac{N}{2}+1},\dots,\ \ \boldsymbol{d}_{\frac{N}{2}-1}\right]^{\boldsymbol{T}}$ is an $N\times N$ Fourier transformation matrix where

$$\boldsymbol{d_l} = \left[1,\ \ \ e^{i\frac{2\pi}{N}l},\dots\ ,\ \ \ e^{i\frac{2\pi}{N}l(N-1)}\ \right]. \tag{11}$$

Let $\boldsymbol{C_j} = \left[\gamma_{j,-\frac{N}{2}}\ \ \gamma_{j,-\frac{N}{2}+1}\ \dots\ \gamma_{j,\frac{N}{2}-1}\right]^{T}$, i.e., the DFT of $\boldsymbol{c_j}$. $\boldsymbol{z}_l$ is then $\boldsymbol{z_l} = \frac{1}{\sqrt{N}}(\boldsymbol{C_l} + \boldsymbol{n_l'})$, where $\boldsymbol{n_l'} = \frac{1}{\sqrt{N}}\boldsymbol{D^H n_l}$.

Using Eq. (10), $\widetilde{\boldsymbol{R}}_{\boldsymbol{j}}$ in Eq. (9) can be rewritten as

$$\widetilde{\boldsymbol{R}}_{\boldsymbol{j}} = \boldsymbol{D}\left(\frac{N}{L}\sum_{l}\boldsymbol{z_l}\boldsymbol{z_l}^{\boldsymbol{H}}\right)\boldsymbol{D^H}. \tag{12}$$

If there were an infinite number of training vectors available, $\frac{N}{L}\sum_l \mathbf{z_l}\mathbf{z_l^H}$ in Eq. (12) would be approximately expressed as

$$\begin{aligned}\frac{N}{L}\sum_{l}\boldsymbol{z_l}\boldsymbol{z_l}^{\boldsymbol{H}} &\cong N\begin{bmatrix} E\left[\left|\gamma_{j,1}\right|^{2}\right]+\sigma^{2} & \cdots & E\left[\gamma_{j,1}{\gamma_{j,N}}^{*}\right] \\ \vdots & \ddots & \vdots \\ E\left[\gamma_{j,N}{\gamma_{j,1}}^{*}\right] & \cdots & E\left[\left|\gamma_{j,N}\right|^{2}\right]+\sigma^{2}\end{bmatrix}\end{aligned} \tag{13}$$

The off-diagonal terms of the matrix in Eq. (13) should theoretically be zero because of the mutual independence of $\gamma_{j,k}$s, as mentioned in Eq. (6). Although $\frac{N}{L}\sum_l \mathbf{z_l}\mathbf{z_l^H}$ cannot be a diagonal matrix if it is calculated with a finite number of training vectors, we could manipulate it into a diagonal matrix by using the Hadamard product with identity matrix $\boldsymbol{I}$. Thus, the proposed CCM estimate, hereafter denoted as $\widehat{\boldsymbol{R}}_{\boldsymbol{j}}$, becomes

$$\widehat{\boldsymbol{R}}_{\boldsymbol{j}} = \boldsymbol{D}\left(\frac{N}{L}\sum_{l}\boldsymbol{z_l}\boldsymbol{z_l}^{\boldsymbol{H}} \circ \boldsymbol{I}\right)\boldsymbol{D}^{H} \tag{14}$$

where $\circ$ denotes the Hadamard product.

In summary, the proposed CCM estimation procedures are described as follows: i) obtaining a collection of training vector $\boldsymbol{v_l}$s from the range bins adjacent to the CUT, ii) obtaining $\boldsymbol{z_l}$s by taking the DFT of $\boldsymbol{v_l}$s, iii) calculating $\left(\frac{N}{L}\sum_l \boldsymbol{z_l}\boldsymbol{z_l^H}\right)\circ\boldsymbol{I}$, and finally, iv) calculating $\boldsymbol{D}\left\{\left(\frac{N}{L}\sum_l \boldsymbol{z_l}\boldsymbol{z_l^H}\right)\circ\boldsymbol{I}\right\}\boldsymbol{D^H}$.

III. Filter Construction Using Estimated CCM

1. Max SINR Filter

We now consider a scenario of the presence of a moving target in the target scene. Since we are concerned with a case with a short observation interval, the target is assumed to have a constant Doppler frequency.

Let the clutter power only reside in $[-p_1,\ p_2]$ in the k domain. $\lambda_{j,k}$ in (8) is then expressed as

$$\lambda_{j,k} = \begin{cases} N{\eta_{j,k}}^2 + \sigma^2 & k = -p_1, -p_1+1,\ \dots p_2 \\ \sigma^2 & elsewhere \end{cases} \tag{15}$$

In this section, we intend to design an adaptive filter that maximizes the output SINR, which hereafter will be referred to simply as the max SINR filter. In this case, for the desired Doppler steering vector $\boldsymbol{s_r}$ with unity intensity, optimum weight $\boldsymbol{w}_{j,r}$ becomes [17]

$$\boldsymbol{w_{j,r}} = \boldsymbol{R}_{\boldsymbol{j}}^{-\boldsymbol{1}}\boldsymbol{s_r} = \left(\sum_{k=1}^{N}\lambda_{j,k}^{-1}\boldsymbol{u_k}\boldsymbol{u_k^H}\right)\boldsymbol{s_r} \tag{16}$$

For $k \neq r$, $\boldsymbol{s_r}$ is orthogonal to $\boldsymbol{u_k}$. In this case, $\boldsymbol{w}_{j,r}$ is expressed as

$$\boldsymbol{w}_{j,r} = \begin{cases} \dfrac{1}{N\eta_{j,r}{}^2 + \sigma^2}\boldsymbol{u}_r & r = -p_1, \ldots, p_2 \\ \dfrac{1}{\sigma^2}\boldsymbol{u}_r & elsewhere \end{cases} \quad (17)$$

Let the target Doppler frequency be f_q, i.e., $k = q$. In this case, the received radar return from the jth range cell, $\boldsymbol{x}_j$, can be expressed as

$$\boldsymbol{x}_j = \zeta_j\sqrt{N}\boldsymbol{u}_q + \sum_{k=-p_1}^{k=p_2}\gamma_{j,k}\sqrt{N}\boldsymbol{u}_k + \boldsymbol{n_j} \quad (18)$$

where ζ_j is the target reflectivity. ζ_j is assumed constant in the following derivation because the change in target reflectivity for short processing intervals might be negligible. To examine the SINR of the filter output at the target bin, that is, the qth Doppler bin, we let f_q be located somewhere within the clutter PSD, i.e., $-p_1 \le q \le p_2$. The max SINR filter output at f_r, namely, $y_{j,r}$, then becomes

$$\begin{aligned} y_{j,r} &= \boldsymbol{w}_{j,r}^H\boldsymbol{x}_j \\ &= \begin{cases} \dfrac{\sqrt{N}\zeta_j}{\beta_r} + \dfrac{\sqrt{N}\gamma_{j,r} + \boldsymbol{u}_r^H\boldsymbol{n_j}}{\beta_r} & r = q \\ \dfrac{\sqrt{N}\gamma_{j,r} + \boldsymbol{u}_r^H\boldsymbol{n_j}}{\beta_r} & r \ne q,\ -p_1 \le r \le p_2 \\ \dfrac{\boldsymbol{u}_r^H\boldsymbol{n}_j}{\sigma^2} & \text{elsewhere} \end{cases} \end{aligned} \quad (19)$$

where $\beta_r = N\eta_{j,r}{}^2 + \sigma^2$. The output SINR at the qth Doppler bin becomes

$$\begin{aligned} SINR &= \frac{\left|\dfrac{\sqrt{N}\zeta_j}{\beta_q}\right|^2}{E\left\{\left|\dfrac{\sqrt{N}\gamma_{j,q} + \boldsymbol{u}_q^H\boldsymbol{n}_j}{\beta_q}\right|^2\right\}} \\ &= \frac{N|\zeta_j|^2}{N\eta_{j,q}{}^2 + \sigma^2} \end{aligned} \quad (20)$$

In deriving Eq. (20), we use the mutual independence between $\gamma_{j,q}$ and $\boldsymbol{u}_q^H\boldsymbol{n}_j$. Initially, the filter input SINR at the qth Doppler bin is $\frac{|\zeta_j|^2}{E\left[|\gamma_{j,q}|^2\right]} = \frac{|\zeta_j|^2}{\eta_{j,q}{}^2}$. As expected, when the noise power is negligible, the filter output SINR is approximately the same as the filter input SINR. This result is quite obvious because the mathematical expression of the clutter spectral component at the qth Doppler bin is the same as that of the target return at the qth Doppler bin, except for being scaled by an unknown complex amplitude $\gamma_{j,q}$. Hence, the filter weight $\boldsymbol{w}_{j,r}$ cannot make differences in the SINRs before and after filtering. Moreover, when noise power is negligible, N does not contribute to SINR improvement, as will be shown in Section IV.

Now, we examine the change in clutter power before and after filtering at the target-free bins. Let the rth Doppler bin be one out of the target-free region, that is, $r \ne q$ and $-p_1 \le r \le p_2$. Employing some manipulations, the clutter power at the rth Doppler bin, which is the mean square value of $\mathrm{y_{j,r}}$, $\mathrm{E}\left[\left|\mathrm{y_{j,r}}\right|^2\right]$, is expressed as $\frac{1}{N\eta_{j,r}{}^2 + \sigma^2}$, whereas the clutter power at the rth Doppler bin before filtering is $\eta_{j,r}{}^2$. This result implies that the bigger $\eta_{j,r}{}^2$ and N are, the larger the clutter suppression ratio becomes.

2. Whitening Filter

In this section, we introduce the whitening filter, whose weight is dictated by $\boldsymbol{w_{j,r}} = \boldsymbol{R_j^{-\frac{1}{2}}s_r}$ (as opposed to the max SINR filter, which uses $\boldsymbol{w_{j,r}} = \boldsymbol{R_j^{-1}s_r}$) and present analytical comparisons of the two filters in terms of the output SINR at the target bin and the interference suppression at the target-free bins.

Following the same procedures leading to Eq. (19) in Section III-1, the whitening filter output at f_r, $y_{j,r}$, is

$$\begin{aligned} y_{j,r} &= \boldsymbol{w}_{j,r}^H\boldsymbol{x}_j \\ &= \begin{cases} \dfrac{\sqrt{N}\zeta_j}{\sqrt{\beta_r}} + \dfrac{\sqrt{N}\gamma_{j,r} + \boldsymbol{u}_r^H\boldsymbol{n_j}}{\sqrt{\beta_r}} & r = q \\ \dfrac{\sqrt{N}\gamma_{j,r} + \boldsymbol{u}_r^H\boldsymbol{n_j}}{\sqrt{\beta_r}} & r \ne q,\ -p_1 \le r \le p_2 \\ \dfrac{\boldsymbol{u}_r^H\boldsymbol{n}_j}{\sigma} & e.w. \end{cases} \end{aligned} \quad (21)$$

where $\beta_r = N\eta_{j,r}{}^2 + \sigma^2$, which is defined the same way it was in Eq. (19). As expected, at the target-free bins where $r \ne q$, the mean square value of $y_{j,r}$ in (21) becomes approximately 1, which implies that the interference PSD is whitened. The SINR at the qth target Doppler bin is approximately $\frac{N|\zeta_j|^2}{N\eta_{j,q}{}^2+\sigma^2}$, which is the same as that of the max SINR filter.

Let us compare two filter outputs in terms of the interference suppression at the target-free bins. First, for the clutter-plus-noise bins in which $r \ne q$ and $-p_1 \le r \le p_2$, the $\mathrm{E}\left[|y_{j,r}|^2\right]$s of the max SINR filter and the whitening filter are approximately $\frac{1}{N\eta_{j,r}{}^2}$ and 1, respectively. Since the initial clutter power at the rth Doppler bin is $\eta_{j,r}{}^2$, their interference suppression ratios are approximately $\frac{1}{N\eta_{j,r}{}^4}$ and $\frac{1}{\eta_{j,r}{}^2}$, respectively. Thus, depending on whether $N\eta_{j,r}{}^2$ is greater than 1, one filter outperforms the other.

We next examine two filter outputs at the noise-only Doppler bins that do not include clutter components. Employing some

calculations, the output noise power $\mathrm{E}\left[\left|y_{j,r}\right|^2\right]$s of the max SINR filter and the whitening filter are approximately $\frac{1}{\sigma^2}$ and 1, respectively. To compare suppression performance in the noise-only region, we compare the output noise power after equating the target return power at two filter outputs. This can be done by multiplying $\frac{1}{\sqrt{\beta_r}}$ by the whitening filter output $y_{j,r}$ in Eq. (21). The calculated noise power ratio is $\frac{N\eta_{j,r}{}^2+\sigma^2}{\sigma^2}$, which is always greater than 1. Thus, the whitening filter always suppresses more noise than the max SINR, which will be evident from the simulation results in Section IV.

To conclude, the whitening filter is generally more advantageous than the max SINR filter in that it outperforms noise suppression in the noise-only region while providing comparable results in terms of SINR at the target bin and in the extent of clutter suppression in the clutter plus noise region. In addition, it provides interference whitening in the target-free region, which may simplify the CFAR algorithm that will be applied to the filter output.

IV. SIMULATIONS

Before delving into the simulation details, we will briefly describe how the sea clutter returns were simulated. We essentially applied the procedure proposed in [5, 18] and simulated two kinds of clutter returns, VV polarized and HH polarized data, for 64 consecutive pulse transmissions. To simulate VV polarized data, the following steps are taken. Since the clutter spectrum in VV polarization is known to resemble a Gaussian function, we tried to assign the mean Doppler frequency and the spectrum width of the Gaussian function that characterize the function shape. To do this, we assumed that the wind speed is 12.5 m/s, operating frequency is 3 GHz, antenna look angle relative to the wind direction is 0°, relative texture value is 1, and platform-induced Doppler frequency is 0 Hz. With the parameter values assumed, the mean Doppler frequency of the Gaussian function becomes roughly 50 Hz. Its spectrum width was made arbitrarily large such that a moving target signature resides within the clutter spectrum. If a radar platform has motion, the platform-induced Doppler frequency is no longer 0 Hz, and a shift in the mean Doppler frequency is created. We will deal with this nonzero Doppler scenario in a later part of this section. For the chosen function shape, we next obtained the autocorrelation function by taking the inverse DFT (IDFT) of the Gaussian function. The sample values of the autocorrelation function were used as the finite impulse response (FIR) filter weights. As the input sequence to the FIR filter, we used a sequence of complex samples whose in-phase and quadrature components are random variables with zero mean and a variance of one-half. The output sequence of the FIR filter corresponds to the time-series clutter/speckle return data in VV polarization. We used the same texture value for the 64 clutter speckle components, as the interval is relatively short. The dashed line in Fig. 1 shows the initially chosen Gaussian-shaped Doppler spectrum. Following the afore- mentioned procedures, we generated 25 sets of the time-series speckle data $c_j[n]$ $(n = 0, \cdots, 63)$, which is the output of the FIR filter. The solid line in Fig. 1 shows an ensemble average of $\left|C_j[k]\right|^2$, which is the clutter PSD.

To simulate HH polarized return data, we first determine a *Lorentzian* function characterized by a small number of mean Doppler frequencies. We arbitrarily chose two mean Doppler frequencies, –150 Hz and 200 Hz. We next obtained the speckle Doppler function by convolving the *Lorentzian* function with an arbitrarily chosen Gaussian function. Since HH polarization returns are related to scatterers moving faster than Bragg scatterers, the typical function shape of the Doppler spectrum cannot be specified in such a way as to associate it with sea state and radar parameters. Thus, we do not enumerate the associated parameter values. For a given Doppler function, the rest of the procedure to simulate the time-series speckle return data is the same as before. The dashed line and the solid line in Fig. 2, respectively, show the initially chosen Doppler function and the PSD of the simulated HH polarized speckle data.

The first scenario concerns a short interval case of 64 radar returns in VV and HH polarization. A shipborne radar with a single transceiver operating at 3 GHz sends a sequence of pulses at 1 kHz of pulse repetition frequency (PRF). Within the target scene, there exists a moving target whose arbitrarily chosen Doppler frequency is 109 Hz. Considering the short interval, we assumed the target reflectivity was constant.

To calculate $\widetilde{\boldsymbol{R}}_{\boldsymbol{j}}$ using the SCM shown in Eq. (9) with the VV polarized data, we used 25 training vectors adjacent to the CUT. We next decomposed $\widetilde{\boldsymbol{R}}_{\boldsymbol{j}}$ into eigenvectors and eigenvalues. For all eigenvectors, we took the DFT and obtained

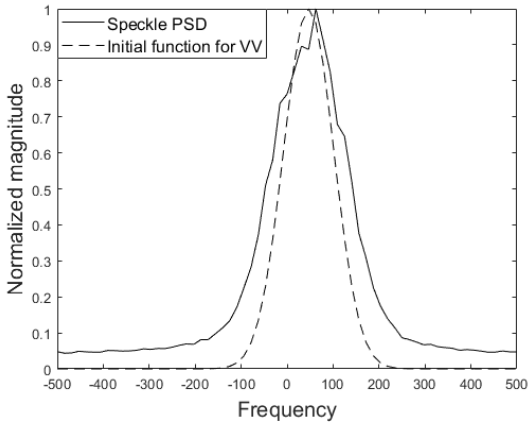

Fig. 1. Initial function and speckle PSD in VV polarization.

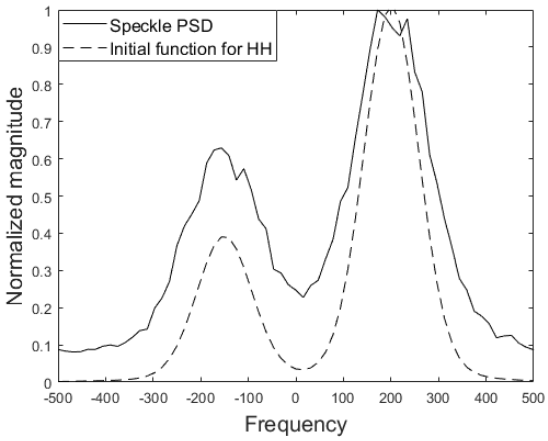

Fig. 2. Initial function and speckle PSD in HH polarization.

their spectra. Fig. 3(a) shows the spectra arranged in such a manner that the spectrum of an eigenvector associated with a larger eigenvalue lay to the left of the x axis. We next applied the proposed algorithm to obtain $\widehat{\boldsymbol{R}}_{\boldsymbol{j}}$. Fig. 3(b) shows the plots of the spectra of the eigenvectors in $\widehat{\boldsymbol{R}}_{\boldsymbol{j}}$, which are arranged as in Fig. 3(a). We note that from the spectra shown in Fig. 3(b), the eigenvectors look to have a form of a Doppler steering vector of a single frequency, which is particularly apparent in the eigenvectors associated with larger eigenvalues. In order to determine the results that could be achieved if there were a sufficient number of training vectors, we arbitrarily generated 250 training vectors, calculated the $\widetilde{\boldsymbol{R}}_{\boldsymbol{j}}$ using the SCM, and finally

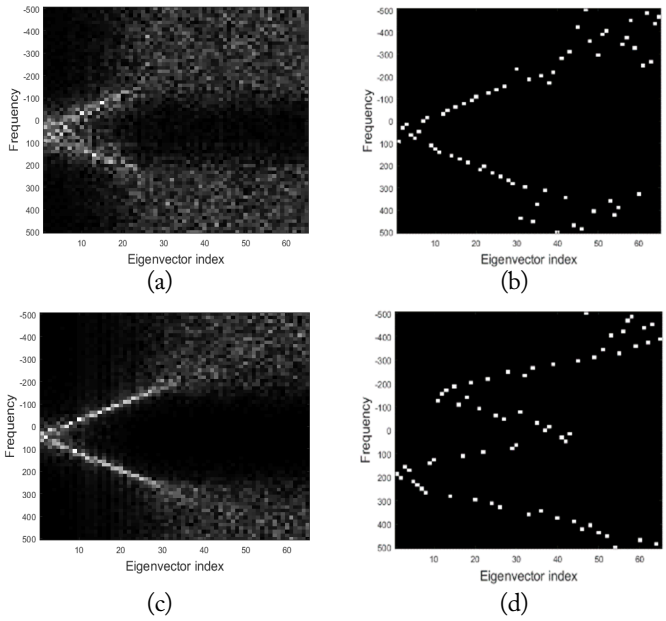

Fig. 3. Spectra of eigenvectors. (a) CCM estimate by SCM (25 training vectors; VV). (b) CCM estimate by proposed algorithm (VV). (c) CCM estimate by SCM (250 training vectors; VV). (d) CCM estimate by proposed algorithm (HH).

obtained the eigenvector spectra shown in Fig. 3(c). More eigenvectors with larger eigenvalues appear to have the form of Doppler steering vectors of a single frequency. Fig. 3(d) is the plot of the eigen vector spectra obtained with the HH polarized data by applying the proposed method. Two dominant Doppler frequencies can be observed in the spectra of the eigenvectors associated with the large eigenvalues.

We next compared the frequency responses of the four filters constructed with CCM estimates by the VV polarized data. For convenience, three of these filters—whose weights are $\widetilde{\boldsymbol{R}}_{\boldsymbol{j}}^{-\mathbf{1}}\boldsymbol{s}_{\boldsymbol{r}}$, $\widehat{\boldsymbol{R}}_{\boldsymbol{j}}^{-\mathbf{1}}\boldsymbol{s}_{\boldsymbol{r}}$, and $\widehat{\boldsymbol{R}}_{\boldsymbol{j}}^{-\frac{\mathbf{1}}{\mathbf{2}}}\boldsymbol{s}_{\boldsymbol{r}}$—obtained with 25 training vectors are called filter A, filter B, and filter C, respectively. The filter with weight $\widetilde{\boldsymbol{R}}_{\boldsymbol{j}}^{-\mathbf{1}}\boldsymbol{s}_{\boldsymbol{r}}$ using 250 training vectors is called filter D. Fig. 4(a)–(d) show the frequency responses of filters A–D, respectively. The frequency responses of filter B and filter C appeared smoother around the clutter-dominant region than those of filter A, which implies that filter A might not effectively suppress clutter components. As expected, filter D, which was obtained with many training vectors, exhibits better performance than filter A.

We next added a target signature to the generated interference, VV polarized data plus additive noise, and examined the filter outputs. The target return power was set to be small enough that the input signal-to-clutter ratio (SCR) and input clutter-to-noise ratio (CNR) were -27 dB and 20 dB, respectively. As shown in Fig. 5(a), the target peak could not be observed at the target Doppler bin of filter A. The target peak

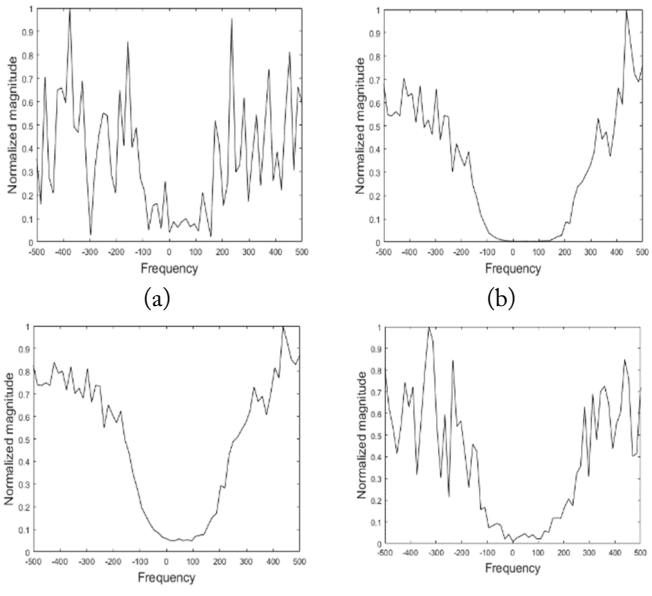

Fig. 4. (a) Frequency response of filter A. (b) Frequency response of filter B. (c) Frequency response of filter C. (d) Frequency response of filter D.

could be observed at the right Doppler frequency in Fig. 5(b), (c), and (d), which are the outputs of filter B, filter C, and filter D, respectively. The target peak shown in Fig. 5(c) looked more dominant because the interference in the target-free region was whitened.

Fig. 6(a)–(d) show the outputs of filter A, filter B, filter C, and filter D, respectively, for the HH polarized data scenario. We may easily observe the same results as we did in the VV polarization case.

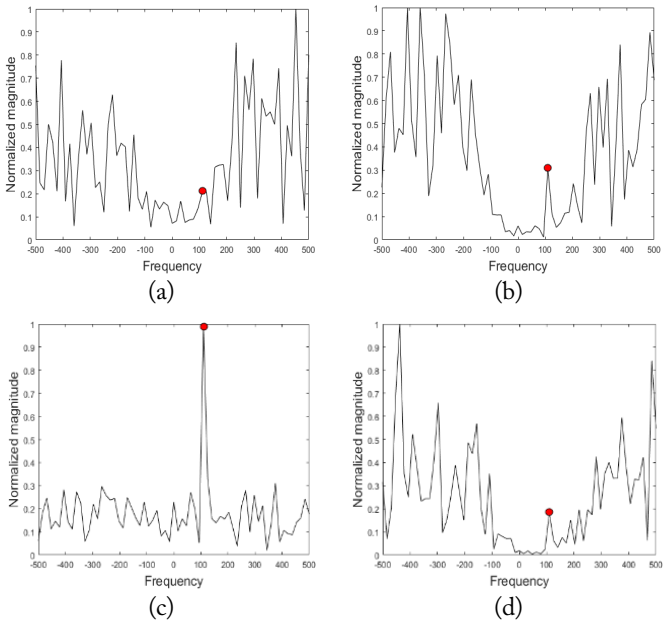

Fig. 5. Filter outputs in VV polarization. (a) Output of filter A. (b) Output of filter B. (c) Output of filter C. (d) Output of filter D.

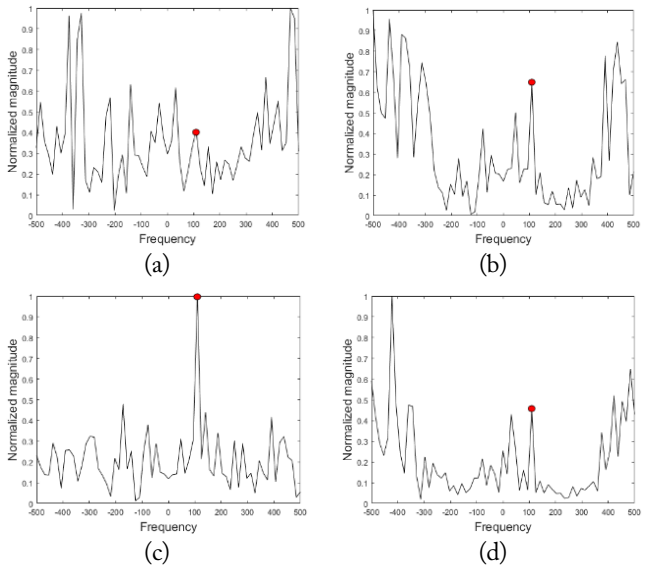

Fig. 6. Filter outputs in HH polarization. (a) Output of filter A. (b) Output of filter B. (c) Output of filter C. (d) Output of filter D.

As mentioned earlier, the platform-induced Doppler frequency tends to shift the mean Doppler frequency of the clutter spectrum [18]. To reflect this aspect, we examined the filter outputs, moving around the moving target Doppler frequency while the clutter spectrum remained fixed. From a radar detector standpoint, this is basically equivalent to shifting the clutter mean Doppler frequency. Fig. 7(a) and (b) denote three SINRs obtained from the VV and HH polarized data, respectively.

The three SINR curves shown in Fig. 7 are the theoretical SINR curve and two other SINR curves obtained with the CCM estimates by the proposed and the conventional/SCM method, respectively. Calculation of SINRs was made at arbitrarily selected different Doppler frequencies in either the clutter plus noise region or the noise-only region of the clutter spectrum. As the theoretical SINR was obtained by Eq. (20), that is, by using a true CCM, it must put a ceiling on the SINR. For both the VV and the HH polarized data, the SINRs by the proposed method are closer to the theoretical SINRs than are the SINRs by the conventional method. This is quite obvious in the clutter plus noise region (see Figs. 1 and 2), which implies that the filter designed with the CCM from the proposed method effectively suppresses clutter. However, no noticeable difference among the three SINRs in the noise-only region can be observed, as the filter performance has no effect in this region.

V. Conclusion

In this paper, we proposed a CCM estimation algorithm in a sea clutter environment. To develop the algorithm, we modified the time-series clutter returns into the frequency domain clutter spectrum and exploited the mutual independence among the complex-valued Doppler spectral components. To compare the proposed algorithm with the SCM algorithm, two filters—the max SINR filter and the whitening filter—that require the CCM were used. We first analytically derived the SINR at the target bin and the clutter suppression ratio in clutter and noise-only regions. Next, we numerically simulated sea clutter, applied the conventional and proposed estimation algorithms, and examined the outputs of the filters designed with the estimated

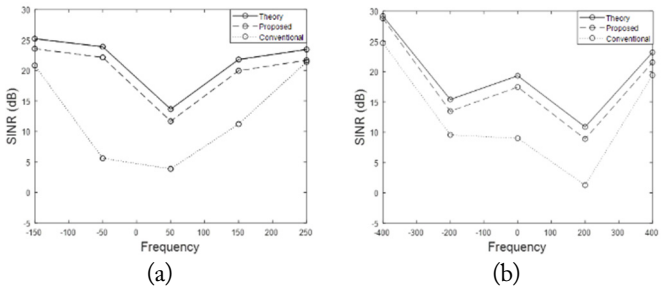

Fig. 7. Three SINRs in (a) VV polarization data and (b) HH polarization data.

CCMs. Comparisons were made by showing the eignvector spectra of the estimated CCMs and the frequency responses and outputs of the filters. Moreover, SINRs at target Doppler bins were examined with a theoretical, analytically derived SINR.

The filter using the proposed CCM estimate, regardless of the filter type, always showed better performance in suppressing clutter than the filter using the SCM estimate. Moreover, the whitening filter was more advantageous, especially in the noise-only region.

This work was supported by a Research Grant from Kwangwoon University in 2020 and by the Agency for Defense Development (No. UD170020FD).

REFERENCES

[1] E. J. Kelly, "An adaptive detection algorithm," *IEEE Transactions on Aerospace and Electronic Systems*, vol. AES-22, no. 2, pp. 115–127, 1986.

[2] E. Conte, M. Longo, M. Lops, and S. L. Ullo, "Radar detection of signals with unknown parameters in K-distributed clutter," *IEEE Proceedings F (Radar and Signal Processing)*, vol. 138, no. 2, pp. 131–138, 1991.

[3] P. L. Shui and Y. L. Shi, "Subband ANMF detection of moving targets in sea clutter," *IEEE Transactions on Aerospace and Electronic Systems*, vol. 48, no. 4, pp. 3578–3593, 2012.

[4] M. Greco, P. Stinco, and F. Gini, "Impact of sea clutter nonstationarity on disturbance covariance matrix estimation and CFAR detector performance," *IEEE Transactions on Aerospace and Electronic Systems*, vol. 46, no. 3, pp. 1502–1513, 2010.

[5] S. Watts, "Modeling and simulation of coherent sea clutter," *IEEE Transactions on Aerospace and Electronic Systems*, vol. 48, no. 4, pp. 3303–3317, 2012.

[6] M. Greco, F. Gini, and M. Rangaswamy, "Statistical analysis of measured polarimetric clutter data at different range resolutions," *IEEE Proceedings–Radar, Sonar and Navigation*, vol. 153, no. 6, pp. 473–481, 2006.

[7] E. Conte, M. D. Bisceglie, C. Galdi, and G. Ricci, "A procedure for measuring the coherence length of the sea texture," *IEEE Transactions on Instrumentation and Measurement*, vol. 46, no. 4, pp. 836–841, 1997.

[8] E. Conte, M. Lops, and G. Ricci, "Asymptotically optimum radar detection in compound-Gaussian clutter," *IEEE Transactions on Aerospace and Electronic Systems*, vol. 31, no. 2, pp. 617–625, 1995.

[9] M. W. Y. Poon, R. H. Khan, and S. Le-Ngoc, "A singular value decomposition (SVD) based method for suppressing ocean clutter in high frequency radar," *IEEE Transactions on Signal Processing*, vol. 41, no. 3, pp. 1421–1425, 1993.

[10] S. P. Sira, D. Cochran, A. Papandreou-Suppappola, D. Morrell, W. Moran, and S. Howard, "A subspace-based approach to sea clutter suppression for improved target detection," in *Proceedings of 2006 40th Asilomar Conference on Signals, Systems and Computers*, Pacific Grove, CA, 2006, pp. 752–756.

[11] E. Conte, M. Lops, and G. Ricci, "Adaptive detection schemes in compound-Gaussian clutter," *IEEE Transactions on Aerospace and Electronic Systems*, vol. 34, no. 4, pp. 1058–1069, 1998.

[12] A. Kammoun, R. Couillet, and F. Pascal, "Optimal design of the adaptive normalized matched filter detector using regularized Tyler estimators," *IEEE Transactions on Aerospace and Electronic Systems*, vol. 54, no. 2, pp. 755–769, 2018.

[13] W. Melvin, M. Wicks, P. Antonik, Y. Salama, P. Li, and H. Schuman, "Knowledge-based space-time adaptive processing for airborne early warning radar," *IEEE Aerospace and Electronic Systems Magazine*, vol. 13, no. 4, pp. 37–42, 1998.

[14] H. Jeon, Y. Chung, W. Chung, J. Kim, and H. Yang, "Clutter covariance matrix estimation using weight vectors in knowledge-aided STAP," *Electronics Letters*, vol. 53, no. 8, pp. 560–562, 2017.

[15] Z. Y. Chen, Y. Zhou, L. R. Zhang, Q. Li, and Y. B. Gu, "A robust single data set-STAP algorithm," in *Proceedings of IET International Radar Conference*, Hangzhou, China, 2015.

[16] S. Theodoridis and R. Chellappa, *Academic Press Library in Signal Processing: Communications and Radar Signal Processing*. New York, NY: Academic Press, 2014.

[17] J. R. Guerci, *Space-Time Adaptive Processing for Radar*. Norwood, MA: Artech House, 2003.

[18] S. Kemkemian, L. Lupinski, V. Corretja, R. Cottron, and S. Watts, "Performance assessment of multi-channel radars using simulated sea clutter," in *Proceedings of 2015 IEEE Radar Conference (RadarCon)*, 2015, pp. 1015-1020.

Sanghyun Choi

received B.S. and M.S. degrees in electric wave engineering from Kwangwoon University, Seoul, Korea, in 2017 and 2019, respectively. He currently works at Korea Aerospace Industries Ltd., Sacheon, Korea, where he is engaging in research on and development of satellite electrical systems. His research interests include the generation and suppression of sea clutter and moving target imaging in a MIMO radar environment.

Hoongee Yang

received a B.S. degree in electronic engineering from Yonsei University, Seoul, Korea, in 1985 and M.S. and Ph.D. degrees in electrical and computer engineering from the State University of New York at Buffalo, Amherst, NY, in 1987 and 1992, respectively. Since 1993, he has been with the Department of Electronic Convergence Engineering, Kwangwoon University, Seoul, Korea. His current research interests are radar signal processing, array signal processing, and SAR/ISAR imaging.

Jimin Song

received B.S. and M.S. degrees in electric wave engineering from Kwangwoon University, Seoul, Korea, in 2017 and 2019, respectively. He is currently working in the Electronics & Software Development Department of Renault Samsung Motors, Yongin, Korea, where he is being engaged in the development of a control logic for safety & seat systems. His current interests are radar imaging techniques and sensor fusion using radar and vision data.

Hyeonmu Jeon

received a B.S. degree in electronic engineering and a Ph.D. degree in radio science and engineering from Kwangwoon University, Seoul, Korea, in 2017. Since 2017, he has been with the Radar Research Institute at Hanwha Systems, where he is currently a Senior Engineer. His main research interests are array signal processing, space time adaptive processing, and synthetic aperture radar.

Jongmann Kim

received a B.S. degree in electronic and electrical engineering from Kyungpook National University, Daegu, Korea, in 2002 and an M.S. degree in electronic and electrical engineering from Pohang University of Science and Technology (POSTECH), Pohang, Korea, in 2004. Since 2005, he has been with the Agency for Defense Development (ADD), Daejeon, Korea, where he is currently a Principle Researcher. His current research interests include radar signals and data processing.

Yongseek Chung

received his B.S., M.S., and Ph.D. degrees in electrical engineering from Seoul National University, Seoul, Korea, in 1989, 1991, and 2000, respectively. From 1991 to 1996, he was with the Living System Laboratory at LG Electronics. From 1998 to 2000, he was a Teaching Assistant in electrical engineering at Seoul National University. From 2001 to 2002, he was with Syracuse University, Syracuse, NY. From 2003 to 2005, he has been a faculty member with the Department of Communication Engineering, Myongji University, Kyunggi, Korea. He is currently a professor in the Department of Electronic Convergence Engineering, Kwangwoon University, Seoul, Korea. His current interests are radar signal processing and microwave imaging techniques.

JOURNAL OF ELECTROMAGNETIC ENGINEERING AND SCIENCE, VOL. 21, NO. 2, 143~147, APR. 2021

https://doi.org/10.26866/jees.2021.21.2.143
ISSN 2671-7263 (Online) · ISSN 2671-7255 (Print)

Four-Array Printed Monopole Yagi-Uda Antenna Mounted on a Small Missile Warhead

Dong-Su Choi[1] · Yoon-Seon Choi[1] · Jae-Yeop Jeong[2] · Tae-Hwan Jung[3] · Jong-Myung Woo[1,*]

Abstract

In this study, the structure of a circular four-array antenna was designed for a monopulse radar attached to a conical small missile warhead with a diameter of 29 mm and a lateral length of 63 mm. A printed monopole Yagi-Uda antenna was adopted as the basic model for the antenna to decrease production cost and reduce weight. The director structure of the printed monopole Yagi-Uda antenna that we proposed was modified to λ/2 to improve the beam direction. Unlike the existing structure, the proposed director was made to be separated from the ground, so that it could act as a director. The antenna was expanded to a four-array structure for the detection of vertical and horizontal planes. As a result of the design, the S_{11} had excellent matching characteristics at the center frequency of 9.375 GHz, and the beam pattern also had directivity in the same direction as the missile travel direction. In the case of gain, it showed more than 6 dBi performance. Finally, the proposed four-array structure antenna was fabricated to verify that the S_{11} and radiation patterns were maintained.

Key Words: Missile Antenna, Printed Monopole Yagi-Uda Antenna, Sum and Difference Pattern, Tracking Antenna.

I. Introduction

Missile accuracy is directly affected by the performance of the radar mounted on the missile. On a large missile, an array of slot antennas or a patch antenna structure is typically used for the missile's radar [1–3]. Antennas with this type of structure are generally mounted with a phase shifter on the back end of the antenna, which tracks and intercepts an object by modifying the beam directing angle. Since such systems are large and relatively expensive, they are not suitable for mounting on a small missile for tracking a small object. Instead, a semi-active-type radar, which only has a receiver module, is employed on small missiles [4].

Among such semi-active-type radar systems, one of the representative antenna designs applied to the surfaces of small missiles is the sub-wavelength-aperture monopulse conformal antenna patented by Lockheed Martin [5]. This antenna is produced by modifying a bull's eye antenna, and to control the missile's flight direction, the beam angle is steered using a dielectric. Detection is performed by the monopulse method utilizing four antenna arrays on the warhead surface. However, when the beam direction setup is modified in the basic bull's eye antenna, the side lobe level is increased, resulting in a complicated structure and high manufacturing cost [6]. In [7], patch antenna used for the transmission and reception module can also be mounted on the sharp and the structure is simple, the missile

Manuscript received September 5, 2020 ; Revised December 14, 2020 ; Accepted January 28, 2021. (ID No. 20200905-134J)
[1]Department of Radio and Information Communication Engineering, Chungnam National University, Daejeon, Korea.
[2]The Attached Institute of Electronics and Telecommunications Research Institute (ETRI), Daejeon, Korea.
[3]Land Radar Team, Hanwha Systems, Yongin, Korea.
[*]Corresponding Author: Jong-Myung Woo (e-mail: jmwoo@cnu.ac.kr)

surface. Although the beam is sharp and the structure is simple, the antenna beam direction does not match the missile's travel direction. Therefore, this is inadequate for use as an antenna for a monopulse radar.

In this study, a position tracking antenna is proposed for use in such radar systems, by using a printed monopole Yagi-Uda antenna that can be mounted on the warhead of a small missile. The antenna can be manufactured by a simple method, and the cost of manufacturing is low. In addition, the beam pattern can be easily modified, and the gain can be easily improved by using a reflector and a director. Moreover, since its shape is easily changed, a printed monopole Yagi-Uda antenna can be easily mounted on the surface of a missile warhead. The typical printed Yagi-Uda antenna uses λ/2 dipole as driven elements [8, 9]. Such a structure requires a balun or an additional ground on the dipole, resulting in a complex or large structure. To solve this problem, we studied a new structure in which the feeding element is a monopole [10–18], which has the symmetry pattern in the broadside direction. However, while this had a simpler structure than the existing Yagi-Uda antenna, it is not suitable for use as a monopulse because the beam does not point in the endfire direction due to the ground effect. To overcome these shortcomings, we proposed a printed Yagi-Uda antenna that can be used as a monopulse radar antenna by applying a λ/2 director to a missile warhead.

II. Antenna Design

Fig. 1 shows the design structure of the antenna proposed in this study. Fig. 1(a) shows the structure with the front part removed in the antenna proposed in [10]. This is to align the beam direction with the missile's travel direction. The antenna director shown in Fig. 1(a) did not perform properly. To solve this problem, a λ/2 director is proposed, as shown in Fig. 1(b). The director attached to the ground was manufactured with a 0.5 mm gap from the ground. The structure shown in Fig. 1(c) is the four-array version of the structure shown in Fig. 1(b).

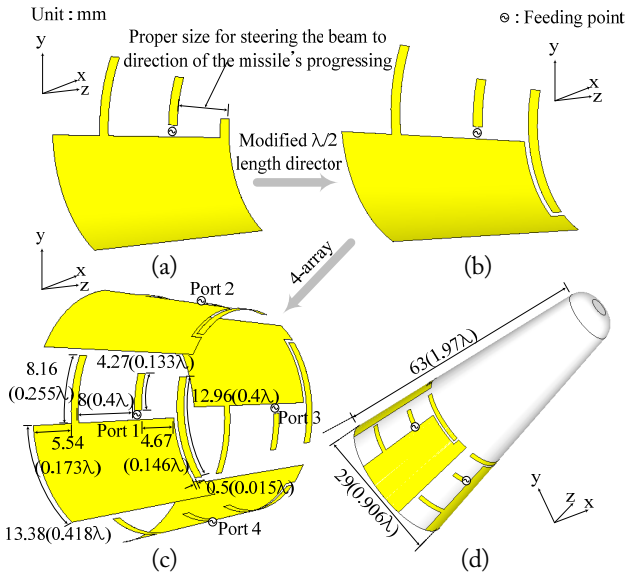

Fig. 1. Structure of the proposed antenna: (a) λ/4 director monopole Yagi-Uda antenna, (b) transferred λ/2 director monopole Yagi-Uda antenna, (c) four-array transferred λ/2 director monopole Yagi-Uda antenna, and (d) missile warhead mounted shape.

Fig. 1(d) shows the three-dimensional shape of the structure mounted on a warhead. The diameter of the bottom surface of the conical warhead was determined to be 29 mm. The antenna was attached to the back end in order to keep the beam direction of the antenna aligned with the missile direction.

Fig. 2 shows the change in gain at 0° when the length of the director of the Fig. 1(c) antenna is swept. Below 0.4λ, it can be seen that the gain increases as the length of the director increases. Above 0.4λ, it can be seen that the gain decreases as the length increases. This is because when the element length becomes larger than a certain length, it operates as a reflector rather than a director. Therefore, in this study, a director of 0.4λ length was designed with the maximum gain. Moreover, the gain change was simulated by changing the distance from the driven element from 0.5 to 2.5 mm in 0.5 mm increments. As a result, the difference between the maximum and minimum values was 0.33 dB. Accordingly, it was confirmed that the distance between the ground and the director does not have a significant effect on gain.

Fig. 3 shows the structure of the manufactured antenna. Coated paper was attached to both sides of the antenna to realize curvature. Two of the antennas are used to detect the vertical plane, while the other two are used to detect the horizontal plane.

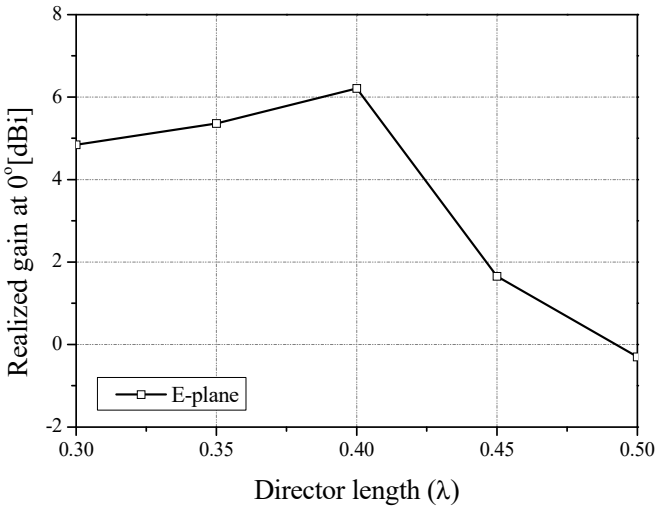

Fig. 2. Realized gain at 0° according to director length.

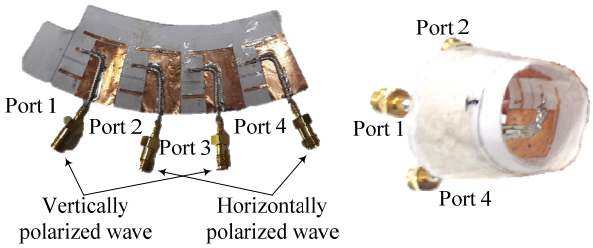

Fig. 3. Manufactured antenna: (a) unfolded form and (b) folded form.

III. Simulated and Measured Results

Fig. 4 shows the simulated (CST Studio Suite, https://www.cst.com) current distribution of the antennas shown in Fig. 1(a) and (b). Fig. 4(a) shows that the current of the director does not flow independently and flows along the ground and does not act as a director. In contrast, the current flow shown in Fig. 4(b) reveals that the current of the director flows in the direction opposite to the feed and operates normally as a director.

Fig. 5 shows the comparison between the S_{11} simulation value and the S_{11} graph of the four ports of the manufactured antenna. Both simulation and measurement values had excellent matching characteristics of −20 dB or more at 9.375 GHz. The measured bandwidth was slightly narrower than the simulated bandwidth of 1,332 MHz, because the ground height of the manufactured antenna was larger than that in the simulation. As the area of the ground plane increases, this effect decreases relatively and thus the tendency of bandwidth increase decreases significantly as the ground plane effect is enhanced. In Fig. 6(a) and (b), the radiation patterns of the Fig. 1(a)–(c) antennas are compared and shown. When changing from the director structure in Fig. 1(a) to the director structure in Fig. 2(b), the 0° gain increased by 1.58 dBi from 4.36 dBi to 5.94 dBi. The four-array structure shown in Fig. 1(c) showed an even better gain of 6.24 dBi. Fig. 6(c) and (d) show the comparison between the simulation and the measured values. Result showed that the front beam pattern and gain were similar. Other directions had different beam patterns, which are considered to be different in the feeding method of simulation and measurement. Table 1 shows the comparison of maximum gain between the simulation and measurement. It can be seen that all four ports have gains similar to the simulation.

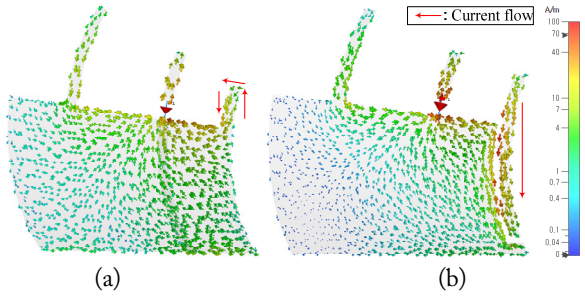

Fig. 4. Current flow: (a) Fig. 1(a) antenna and (b) Fig. 2(b) antenna.

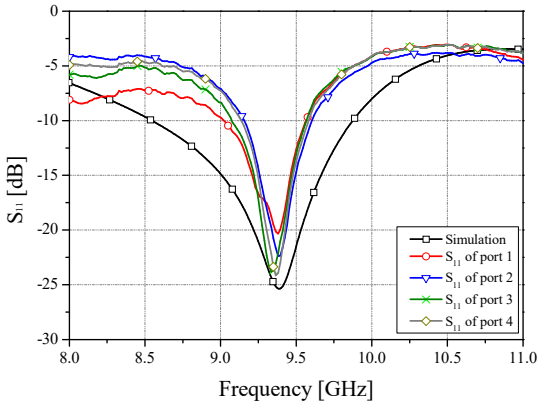

Fig. 5. S_{11} of Fig. 1(c) antenna.

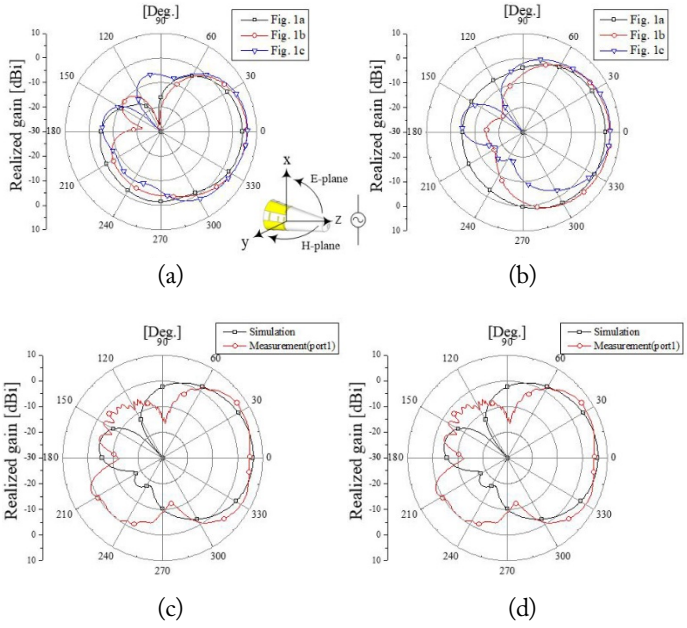

Fig. 6. Comparison of radiation patterns: (a) simulation E-plane comparison of Fig. 1(a)–(c) antennas, (b) simulation H-plane comparison of Fig. 1(a)–(c) antennas, (c) E-plane comparison of Fig. 1(c) antenna simulation and measurement, and (d) H-plane comparison of Fig. 1(c) antenna simulation and measurement.

Table 1. Total efficiency levels and peak gains of the designed antenna

	Maximum gain (dBi)				
	Simulation	Measurement			
		Port 1	Port 2	Port 3	Port 4
E-plane	6.24	6.41	6.19	6.18	6.35
H-plane	6.24	6.63	6.42	6.13	5.98

IV. Conclusion

In the present study, a four-array antenna was proposed for a small missile radar that can be mounted on a conical warhead. The antenna adopts the printed Yagi-Uda antenna as the basic structure to solve the complex structure, which is the disadvantage of the general Yagi-Uda antenna. In addition, a $\lambda/2$ director was applied to improve the beam direction, which is a disadvantage of the printed monopole Yagi-Uda antenna. Unlike the existing structure, the director is positioned in front of the ground so that current flows independently and can function as a director. As a result of the design, S_{11} has excellent matching characteristics of -20 dB or more at the center frequency of 9.375 GHz in the simulation and manufacture. In addition, in the case of the radiation pattern, it has a characteristic that is directed in the same direction as the missile travel direction, and in the case of gain, both simulation and production values have excellent performance of 6 dBi or more. As a result of the design, the simulation has a maximum gain of 6.24 dBi, and the manufactured antenna has a similar gain of 6 dBi or more. For this reason, the antenna proposed in this study can be mounted on a missile warhead and used as an antenna for radar.

References

[1] H. S. Lee and J. M. Woo, "A study on the aerial vehicle mounted antenna," in *Proceedings of KIEES Microwave and Electromagnetic Wave Communication Conference*, 1999, pp. 141–144.

[2] H. J. Visser, *Array and Phased Array Antenna Basics*. New York, NY: John Wiley & Sons Inc., 2005.

[3] K. B. Kim, B. C. Jung, and J. M. Woo, "A compact dual-polarized (CP, LP) with dual-feed microstrip patch array for target detection," *IEEE Antennas and Wireless Propagation Letters*, vol. 19, no. 4, pp. 517–521, 2020.

[4] D. Ciampa and D. Bucco, "The performance of semi-active radar guided missiles against sea skimming target," Defence Science and Technology Organization, Canberra, Australia, 1995.

[5] B. A. Williams, "Subwavelength aperture monopulse conformal antenna," US Patent 8,354,953, Jan 15, 2013.

[6] C. J. Vourch and T. D. Drysdale, "V-band "Bull's eye" antenna for cubesat application," *IEEE Antenna and Wireless Propagation Letters*, vol. 13, pp. 1092–1095, 2014.

[7] V. Jaeck, L. Bernard, K. Mahdjoubi, R. Sauleau, S. Collardey, P. Pouliguen, and P. Potier, "A conical patch antenna array for agile point-to-point communications in the 5.2-GHz band," *IEEE Antenna and Wireless Propagation Letters*, vol. 15, pp. 1230–1233, 2016.

[8] M. Nasir, Y. Xia, M. Jiang, and Q. Zhu, "A novel integrated Yagi-Uda and dielectric rod antenna with low sidelobe level," *IEEE Transactions on Antennas and Propagation*, vol. 67, no. 4, pp. 2751–2756, 2019.

[9] B. K. Tehrani, B. S. Cook, and M. M. Tentzeris, "Inkjet printing of multilayer millimeter-wave Yagi-Uda antennas on flexible substrates," *IEEE Antennas and Wireless Propagation Letters*, vol. 15, pp. 143–146, 2015.

[10] H. S. Ham, Y. R. Kim, and J. M. Woo, "Active printed inverted F antenna for beam steering," in *Proceedings of 2007 IEEE Antennas and Propagation Society International Symposium*, Honolulu, HI, 2007, pp. 3348–3351.

[11] S. M. Moon, J. M. Woo, and H. C. Shin, "Printed monopole Yagi-Uda antenna," in *Proceedings of KIEES Fall Microwave and Propagation Conference*, 2001.

[12] S. M. Lee, N. E. Sung, and J. M. Woo, "Printed active Yagi-Uda antenna," in *Proceedings of KIEES Spring Microwave and Propagation Conference*, 2002, pp. 169–172.

[13] H. S. Ham, S. M. Moon, and J. M. Woo, "Printed beam steering active antenna mounted on a vehicle," in *Proceedings of the Korea Institute of Military Science and Technology Conference*, 2005, pp. 165–168.

[14] H. S. Ham, S. M. Moon, J. C. Kim, and J. M. Woo, "Characteristics of a printed beam steering active Yagi-Uda antenna mounted on an aircraft model," in *Proceedings of Summer Microwave and Propagation Conference*, 2006, pp. 252-252.

[15] J. M. Lee and J. M. Woo, "Design of GPS receiving antenna installed in a missile's warhead," *Journal of Korean Institute of Electromagnetic Engineering and Science*, vol. 17, no. 9, pp. 900–912, 2006.

[16] S. K. Han, J. Y. Park, and J. M. Woo, "Printed folded monopole Yagi-Uda antenna," in *Proceedings of KIEES Microwave and Lightwave Technology Conference*, 2007, pp. 41–44.

[17] D. H. Shin, Y. S. Choi, and J. M. Woo, "Missile mounted beam steering print type inverted F antenna design," in *Proceedings of KIEES Microwave and Lightwave Technology Conference*, 2014, pp. 27–28.

[18] J. M. Woo, "Aerial vehicle mounted antenna," in *Proceedings of KIEES Microwave and Electromagnetic Wave Communication Conference*, 2020, pp. 26–26.

Dong-Su Choi

received his B.S. degrees in physics from Gyeongsang National University in 2013 and M.S. degrees in radiowave engineering from Chungnam National University in 2019, respectively. He is currently working toward his Ph.D. degree at the antenna laboratory. His main research interest is antennas.

Yoon-Seon Choi

received her B.S. and M.S. degrees in radiowave engineering from Chungnam National University in 2014 and 2016, respectively. She is currently working toward her Ph.D. degree at the antenna laboratory. Her main research interest is antennas.

Jae-Yeop Jeong

received his B.S. and M.S. degrees in radiowave engineering from Chungnam National University in 2015 and 2017, respectively. He is currently working as a researcher in the attached institute of ETRI. His main research interest is antennas.

Tae-Hwan Jung

received his B.S. and M.S. degrees in radiowave engineering from Chungnam National University in 2012 and 2014, respectively. He is currently working about land radar as a senior engineer in Hanwha systems. His main research interest are antennas and radar.

Jong-Myung Woo

received his B.Sc. degree in electronics engineering from Konkuk University in Korea and Ph.D. degree in electronics engineering from Nihon University in Japan. He is a professor of Department of Radio and Information Communications Engineering in Chungnam National University in Korea. He is mainly interested in antennas.

JOURNAL OF ELECTROMAGNETIC ENGINEERING AND SCIENCE, VOL. 21, NO. 2, 148~152, APR. 2021

https://doi.org/10.26866/jees.2021.21.2.148
ISSN 2671-7263 (Online) · ISSN 2671-7255 (Print)

Distances between Rats in Reverberation Chambers Used for Large-Scale Experiments

Sangbong Jeon[1] · Wook Jang[2] · Ae-Kyoung Lee[1] · Hyung-Do Choi[1] · Jeong-Ki Pack[3] · Jianqing Wang[4] · Dongho Kim[2,*]

Abstract

We investigate the whole-body average specific absorption rate (WBA-SAR) of rats under various plane wave exposure characteristics, including different polarizations, incidence angles, distances between rats, and total number of rats. Unlike many other studies, we start our SAR analysis from one rat and expand it to 27 rats facing random directions in a three-dimensional area. In a one-rat analysis, we examine how the incidence direction and polarization affect the SAR of a single rat. Moreover, we look into how various incidence polarizations behave differently after they are transmited through a rat, the information of which is then used to analyze the effect of spacing among 27 randomly arranged rats. Next, we analyze the effect on spacing of the 27 rats deployed under a 52-plane-wave exposure, which is introduced to mimic a realistic reverberation chamber (RC) environment. We show the deviation in WBA-SAR according to the distance between rats, which provides guidelines for selecting the appropriate rat distance based on the number of animals and the exposure deviation within a limited working volume in an RC for large-scale experiments.

Key Words: Incident Angle, Incident Polarization, Rat Distance, SAR, Standard Deviation, Statistical Analysis.

I. Introduction

Various types of experimental systems have been used to study the toxicology and carcinogenesis of animal exposure to electromagnetic waves [1]. A reverberation chamber (RC) is one of the most widely used facilities, which not only provides a statistically uniform field distribution within a specific volume, but also permits the animals to move freely around in their cages [2]. Although an RC offers a uniform distribution, obtaining an evenly distributed specific absorption rate (SAR) is another important aspect that should be accurately analyzed for individual animals within an RC. In [3], it was reported that the SAR depends on certain parameters such as the polarization or rat arrangement, which was investigated in an RC. In [4], using a rat phantom in an RC, the authors showed that a two-dimensional statistical SAR distribution can explain the corresponding distance between rats. However, despite these previous studies, there are still no practical guidelines for an optimum cage deployment in a practical RC design, which should consider the overall effect of the incident polarization, angle, distance between rats, and arrangement.

In this letter, we provide a new method for determining the optimum distance between rats to obtain even SAR levels among rats; this will be used in the RC design for a preliminary

Manuscript received September 7, 2020 ; Revised December 4, 2020 ; Accepted February 14, 2021. (ID No. 20200907-136J)
[1]Radio & Satellite Research Division, Electronics and Telecommunications Research Institute (ETRI), Daejeon, Korea.
[2]Department of Electrical Engineering, Sejong University, Seoul, Korea.
[3]Radio Sciences & Engineering Department, Chungnam National University, Daejeon, Korea.
[4]Electrical and Electronic Engineering, Nagoya Institute of Technology, Nagoya, Aichi, Japan.
[*]Corresponding Author: Dongho Kim (e-mail: dongkim@sejong.ac.kr)

study promoted by a Korea – Japan joint animal study. Specifically, we analyze how the incident polarizations and angles affect the SAR of a single rat, which will then be expanded to a three-dimensional (3D) random arrangement of 27 rats to examine the rat–distance effect on the SAR variations.

II. Methods

The overall simulation setup used throughout this work is as follows:

- Simulation program and data: Sim4Life (Zurich MedTech AG) [5]
- Rat model: big male rat model with a straight tail (IT'IS Foundations) (Sprague Dawley, 567 g)
- Incident wave: plane wave with a 1 V/m electric field at 900 MHz
- Analysis data: whole-body average SAR (WBA-SAR, μW/kg)

The big male rat model used is shown in Fig. 1(a), where each face of the imaginary rectangular parallelepiped is touching the outermost body part of the rat. The distances (d) between neighboring rats are the same along the x-, y-, and z-axes, as shown in Fig. 1(b), and will be used for the 27-rat arrangement.

III. Results

Fig. 2 shows how the incident angles and polarization of a plane wave affect the WBA-SAR of a single rat. We can see that, when the incident polarization is parallel to the rat axis (z-axis), and the incident angle is facing the maximum cross-section area of the rat, the WBA-SAR increases (see E_1 and E_4). On the contrary, for the perpendicular incidence (E_2 and E_3), the WBA-SAR is very low.

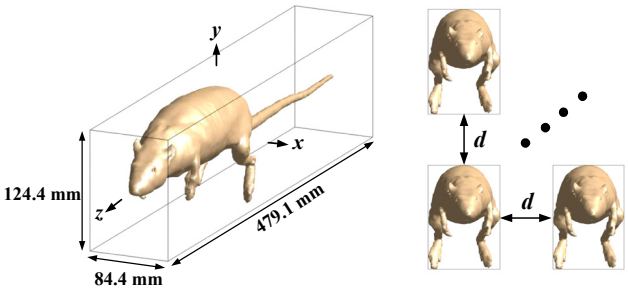

Fig. 1. (a) Big male rat model and (b) rat distance for 27-rat arrangement shown in Fig. 4.

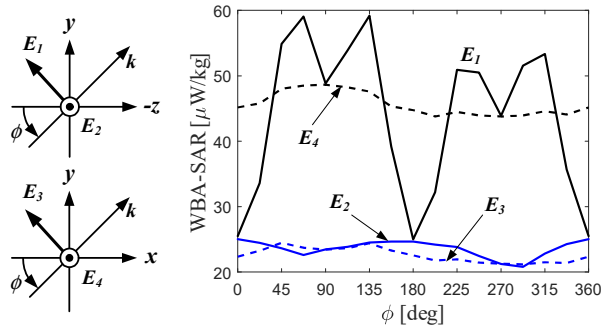

Fig. 2. WBA-SAR variations of a single rat for different incident angles and polarizations.

We examine how the incident polarization perturbs the electric fields around the rat, as shown in Fig. 3 for two specific cases of E_3 and E_4 under $\Phi = 0°$. In both cases, there is strong interference between the incident and scattered waves in region A, which produces high periodic oscillations. In region B, however, the scattering properties are extremely different from each other, and a rat under a z-polarized incidence induces a high shadowing effect immediately behind the rat. In contrast, for y-polarized incidence, the total E field is immediately restored to the incident level. Therefore, when we arrange a large number of rats in a particular area such as in an RC, we can expect that the SAR of each rat will be significantly affected by the incident polarization, direction, distance between rats, and the direction the rat is facing.

To analyze the overall effect of these parameters, we arranged 27 rats as shown in Fig. 4. For the arrangement, we first arranged

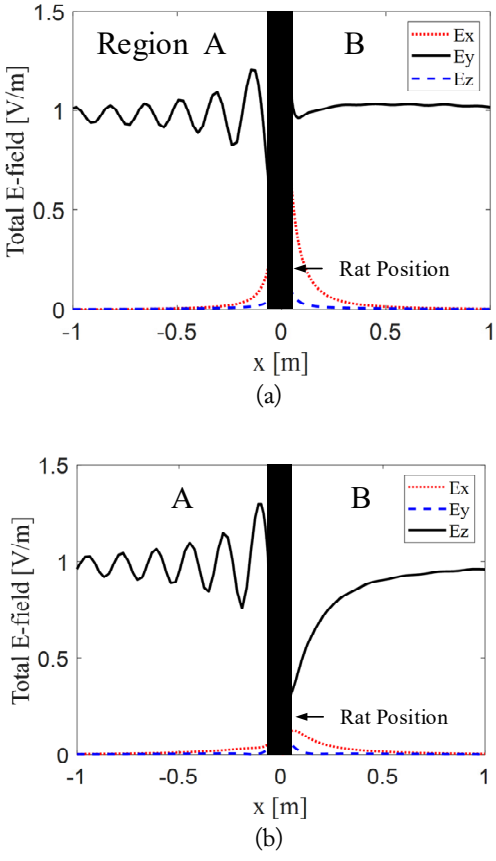

Fig. 3. Magnitude of total E-field behaviors for (a) y-polarized (E3, $\Phi = 0°$) and (b) z-polarized incident (E4, $\Phi = 0°$) waves propagating toward the positive x-axis.

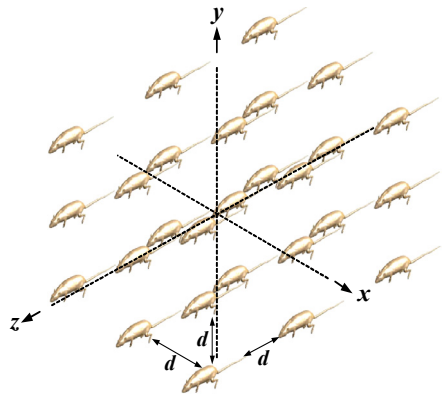

(a)

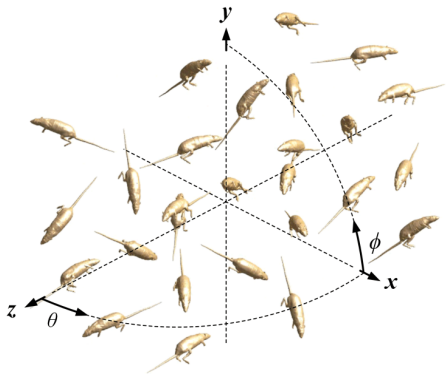

(b)

Fig. 4. Arrangement of 27 rats for (a) regular directions and (b) facing random directions according to the random rotation angles defined in Table 1.

all rats regularly in a 3 × 3 × 3 formation with the same distance (d) between rats. We then rotated each rat according to the random angles given in Table 1, where the center of rotation of each rat is at the center of each rectangular parallelepiped. All rotation angles were chosen from uniformly distributed random numbers using MATLAB such that none of the rats overlapped even at the minimum distance of $d = 50$ mm. A regular deployment, as shown in Fig. 4(a), is unrealistic considering the animals' movement. However, the deployment of Fig. 4(b) is more realistic for a simulation. As shown in Fig. 5, the average WBA-SAR and the corresponding standard deviation (SD) of the 27 rats were analyzed for both regular and random deployments. Here, we used 52 incident plane waves coming from every 45° angle to mimic the environment in the RC. As the distance between rats increased in both deployments, the average WBA-SAR reached the WBA-SAR of one rat at $d = 400$ mm because the shadowing effect gradually diminished for a larger spacing. In addition, note that there is a small difference between the average WBA-SARs of the regular and random deployments.

In this study, the same spacing d was used for the x-, y-, and z-axes for a simple arrangement and calculation. However, in an actual experimental environment, in many cases, it is inevitable

Table 1. Random rotation angles of each rat for the arrangement of Fig. 4(b)

Rat no.	θ (°)	ϕ (°)	Rat no.	θ (°)	ϕ (°)
1	62	169	15	60	19
2	65	315	16	138	159
3	15	30	17	135	300
4	32	269	18	67	323
5	140	290	19	32	70
6	50	345	20	150	0
7	162	66	21	10	110
8	21	215	22	134	190
9	178	108	23	60	60
10	97	48	24	31	359
11	127	76	25	37	0
12	150	250	26	163	107
13	155	25	27	122	50
14	40	60	-	-	-

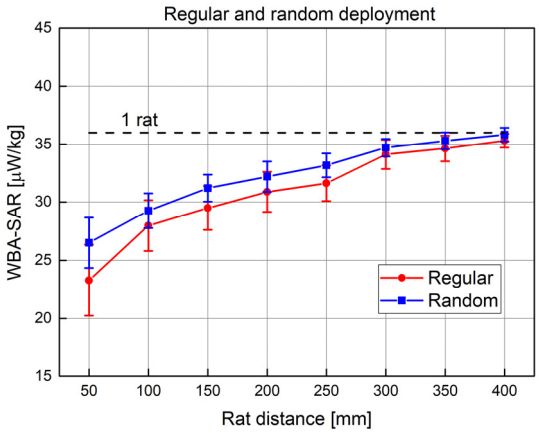

Fig. 5. Average WBA-SAR of 27 rats.

for different intervals to be used depending on the axis. The working volume of the RC designed and manufactured for the Korea–Japan joint animal study was 1.5 × 1.3 × 1.5 m^3, and 75 rats (one per cage) had to be placed within this limited space. The final distances between cages were 150 mm, 50 mm, and 180 mm in the three directions, respectively. The SAR calculations were conducted, and the results for the 27 regular and random arrangements were 30.42 ± 1.4 μW/kg and 31.23 ± 1.4 μW/kg, respectively. The average WBA-SAR was 0.6 dB lower than the single rat case, and the SAR value of each rat falls within ±5% of the average WBA-SAR of the 27 rats. In addition, we also found that the average WBA-SARs between regular and random deployments was no greater than 2.6%.

IV. Conclusion

In large-scale SAR experiments within a limited working

volume of an RC, as the distance between objects (rats) increases, the shadowing effect decreases, but requires a larger space. To provide the relation between the rat distance and exposure deviation (mean and SD), 27 rats in an RC were simulated according to their deployments, which were drawn from a statistical analysis of their 3D arrangement. Using our results, we will reflect the distance of 150 × 50 × 180 mm^3 between the cages in the RC design for the Korea–Japan joint animal study. In the future, we will carry out rat weight-based exposure simulations for 75 rats under the designed distance between rats. In addition, we expect that the proposed approach will be a helpful guideline for a practical RC design for large-scale experiments.

This work was supported by the ICT R&D program of MSIP/IITP (No. 2019-0-00102, A Study on Public Health and Safety in a Complex EMF Environment).

REFERENCES

[1] A. Paffi, C. Merla, R. Pinto, G. A. Lovisolo, M. Liberti, C. Marino, M. Repacholi, and F. Apollonio, "Microwave exposure systems for *in vivo* biological experiments: a systematic review," *IEEE Transactions on Microwave Theory and Techniques*, vol. 61, no. 5, pp. 1980–1993, 2013.

[2] K. B. Jung, T. H. Kim, J. L. Kim, H. J. Doh, Y. C. Chung, J. H. Choi, and J. K. Pack, "Development and validation of reverberation chamber type whole-body exposure system for mobile-phone frequency," *Electromagnetic Biology and Medicine*, vol. 27, no. 1, pp. 73–82, 2008.

[3] B. J. Klauenberg and D. Miklavcic, *Radio Frequency Radiation Dosimetry and Its Relationship to the Biological Effects of Electromagnetic Fields.* Dordrecht: Kluwer Academic Publishers, 2000.

[4] J. Chakarothai, J. Wang, O. Fujiwara, K. Wake, and S. Watanabe, "Dosimetry of a reverberation chamber for whole-body exposure of small animals, " *IEEE Transactions on Microwave Theory and Techniques*, vol. 61, no. 9, pp. 3435–3445, 2013.

[5] Zurich MedTech (ZMT), "Sim4Life 5.2," 2019; https://www.zmt.swiss.

Sang Bong Jeon

received his B.S., M.S., and Ph.D. degrees in electronic engineering from Yeungnam University, Gyeongsan, Korea, in 2001, 2003, and 2007, respectively. From 2008 to 2010, he was a senior research engineer at the Korea Radio Promotion Association, Seoul, Korea, where he conducted research in the fields of electromagnetic compatibility technology. Since 2010, he has been with Radio & Satellite Research Division, Electronics and Telecommunications Research Institute, Daejeon, Korea. His research interests include bioelectromagnetics and electromagnetic compatibility.

Wook Jang

received the B.S. degree in electronics and information engineering from Sejong University, Seoul, Korea, in 2020. Since March 2021, he is currently working towards his M.S. degree at the electronic engineering, Sejong University. His research interests include the analysis and design of high-gain beam scanning antennas by using a partially reflective surface.

Ae-Kyoung Lee

received her B.S. and M.S. degrees in electronics and engineering from Chungang University, Seoul, Korea in 1990 and 1992, respectively, and a PhD in radio science and engineering from Chungnam National University, Daejeon, Korea in 2003. In 1992, she joined the Radio Technology Group at the Electronics and Telecommunications Research Institute, Daejeon, Korea, where she has been involved in projects on measurement technologies and numerical analyses of electromagnetic compatibility and human exposure to RF fields. Dr. Lee was the recipient of the Japan Microwave Prize at the 1998 Asia-Pacific Microwave Conference, Japan and the Technology Award from the Korea Electromagnetic Engineering Society in 1999.

Hyung-Do Choi

received his M.S. and Ph.D. degree in material sciences from Korea University in 1989 and 1996, respectively. Since 1997, he has been with Electronics and Telecommunications Research Institute, Daejeon, Korea, where he is presently a principal member of Radio & Satellite Research Division. He has conducted research on the biological effects of RF radiation and has developed RF radiation protection standards. His current research interests include spectrum management, microwave tomography, and EMC countermeasures.

Jeong-Ki Pack

received his B.S. in Electronic Engineering from Seoul National University, Seoul, Korea, in 1978. From 1978 to 1983, we worked for the Agency for Defence Development in Korea as a researcher. He received his M.S. and Ph.D. degrees in 1985 and in 1988, respectively, in electromagnetic wave propagation from Virginia Tech., USA. He joined ETRI in 1988 and moved to Dong-A University in 1989. Since February 1995, he has been with Chungnam National University, Daejeon, Korea, as a professor at the Department of Radio Science and Engineering. He is currently an emeritus professor at the same department. His research interests include electromagnetic wave propagation and bio-electromagnetics.

Jianqing Wang

received the B.E degree in electronic engineering from Beijing Institute of Technology, Beijing, China, in 1984, and the M.E. and D.E. degrees in electrical and communication engineering from Tohoku University, Sendai, Japan, in 1988 and 1991, respectively. He was a Research Associate with Tohoku University and a Senior Engineer with Sophia Systems Co., Ltd. In 1997, he joined the Nagoya Institute of Technology, Nagoya, Japan, where he has been a Professor, since 2005. He has authored Body Area Communications (Wiley-IEEE), in 2012, and received the IEEE EMCS Technical Achievement Award, in 2019. He is IEEE Fellow. His current research interests include biomedical communications and electromagnetic compatibility.

Dongho Kim

received the B.S. and M.S. degrees in electronics engineering from Kyungpook National University, Daegu, Korea, in 1998 and 2000, respectively, and the Ph.D. degree in electrical and electronics engineering from Korea Advanced Institute of Science and Technology (KAIST), Daejeon, Korea, in 2006. From 2000 to 2011, he was a Senior Researcher in Electronics and Telecommunications Research Institute (ETRI), Daejeon, Korea. In 2011, he joined the Department of Electrical Engineering, Sejong University, Seoul, Korea, where he is now a Professor. Prof. Kim is a member of the Institute of Electrical and Electronics Engineers (IEEE), an expert of the International Electrotechnical Commission (IEC), and a life-member of the Korean Institute of Electromagnetic Engineering and Science (KIEES). His research interests include advanced electromagnetic wave theory, antenna design, metamaterials, and bio-electromagnetics.

JOURNAL OF ELECTROMAGNETIC ENGINEERING AND SCIENCE, VOL. 21, NO. 2, 153~160, APR. 2021

https://doi.org/10.26866/jees.2021.21.2.153
ISSN 2671-7263 (Online) · ISSN 2671-7255 (Print)

Experimental Characterization of 2 × 2 Electronically Reconfigurable 1 Bit Unit Cells for a Beamforming Transmitarray at X Band

Biswarup Rana[1] · In-Gon Lee[1] · Ic-Pyo Hong[2,*]

Abstract

This paper proposes a reconfigurable unit cell for a transmitarray operating at the X band. The unit cell consists of an active patch, a passive patch, and a phase shifter. The active patch has two PIN diodes that change the phase of 180° of the transmitted waves. The passive and active patches both have circular slots to enhance the bandwidth of the transmitted wave. We also propose a new type of experimental characterization technique to measure the performance of the unit cells at the X band without fabricating the entire transmitarray. Instead of a 1 unit cell as described in the literature, we propose 2 × 2 unit cells to measure the performance of unit cells using the X band waveguide. The waveguide consists of a WR-90 section and a rectangular to square waveguide transition section that can be fit to our proposed structure. A good agreement between simulated and measured results was found.

Key Words: Beamforming, PIN Diode, Reconfigurable Unit Cell, Transmitarray.

I. Introduction

Transmitarrays are one of the promising candidates for beam steering and polarization conversion at microwave and millimeter waves instead of the traditional phased arrays, which suffer from large insertion loss. Automotive radars, 5G networks, and some advanced military equipment require electronic scanning and a polarization converted beam. These types of antennas were extensively investigated in the last few years [1–12], and in [13], the first transmitarray was proposed, connecting upper patch and lower patch through a via for beam steering operation. Since then, different types of transmitarrays have been proposed by different authors. Transmitarrays consist of several periodical identical elements known as unit cells. The unit cell can be based on a frequency selective surface or microstrip patches, or they can be inspired by metamaterial structures. Transmitarrays can be fabricated using conventional printed circuit board (PCB) technology by etching different layers and then connecting those layers. They are very lightweight and planar, which makes them suitable for integration with other planar devices. Moreover, the feeding antenna for a transmitarray is kept separated and at a distance, making transmitarrays ideal for a greater degree of modularity in comparison to conventional phased array antennas. A simple design, low fabrication design costs, greater flexibility, low losses, and low-profile characteristics make the transmitarray antenna system ideal for beam steering and polariza-

Manuscript received November 14, 2020 ; Revised January 9, 2021 ; Accepted February 14, 2021. (ID No. 20201114-183J)
[1]Smart Natural Space Research Center, Kongju National University, Cheonan, Korea.
[2]Department of Information and Communication Engineering, Kongju National University, Cheonan, Korea.
[*]Corresponding Author: Ic-Pyo Hong (e-mail: iphong@kongju.ac.kr)

tion conversion of waves, and they are preferable in comparison to phased array. The transmitarray antennas are also more attractive when compared to reflect arrays [14–16] because waves are passed through the transmitarray, so they have no feed blockage. To achieve electronic beam steering, polarization conversion, or frequency tuning characteristics, transmitarrays require different types of elements, such as PIN diodes, varactor diodes, microelectromechanical systems, liquid crystals, and more. Several types of unit cells have been proposed in recent years using PIN diodes [1, 3, 5, 10, 11], varactor diodes [7, 17], microfluidics [18], or MEMS [19], and it is crucial to understand the performance of the unit cell before fabricating a complete transmitarray structure.

In this paper, a new type of very wideband 1 bit (0°/180°) electronically reconfigurable unit cell is proposed using PIN diodes. The size of the unit cell at X band is not comparable to the size of the X band waveguide. Thus, it is difficult to fabricate a waveguide transition section from X band WR-90 to the size of the unit cell [1]. To overcome this, we propose a new type of experimental characterization procedure based on an X band waveguide rectangular to square transition section where we have used 2 × 2 unit cells instead of a 1 unit cell. The design of the rectangular to square waveguide transition section is very easy, and the proposed method is useful for determining the performance of unit cells at the initial stages, without having to fabricate the entire transmitarray.

The remainder of this paper is arranged as follows. In Section II, the configuration and operating principle of the unit cell are discussed, and then the simulated performance of the unit cell is described in Section III. The waveguide transition section is a vital part of our design, and we describe the performance of the waveguide transition section with a WR-90 waveguide in Section IV. Similarly, biasing lines for our 2 × 2 unit cells are crucial, so biasing lines and the configuration of the 2 × 2 unit cells are explained in Section V. The performances of the 2 × 2 unit cells with an X band WR-90 waveguide and the rectangular to square waveguide transition are discussed in Section VI. Finally, a conclusion of the total work is presented in Section VII.

II. Configuration and Operating Principle of the Unit Cell

Fig. 1(a) shows the cross-sectional view of the proposed unit cell, and Fig. 1(b) shows the 3D view of the proposed unit cell. A passive circular-shaped patch antenna with an 8.8 mm diameter that is loaded with a circular slot having a diameter of 3.1 mm on the receiving side were considered for our design. A similar circular patch and slot on the transmitting side were also considered. The transmitting side of the patch has two PIN

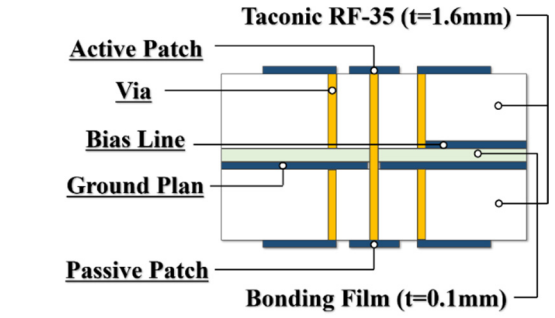

(a)

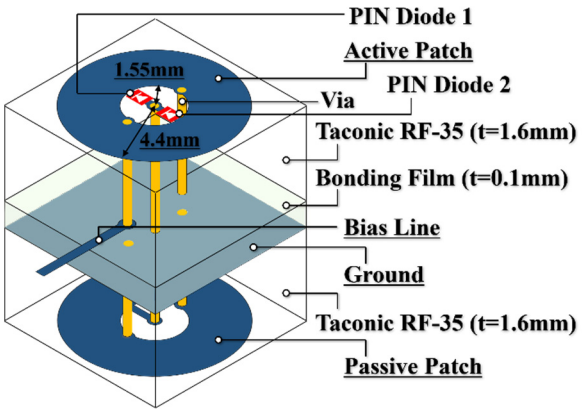

(b)

Fig. 1. (a) Cross-sectional view of the unit cell. (b) 3D view of the unit cell.

diodes (MA4GP907; MACOM, Lowell, MA, USA), which are shown in Fig. 1(b). The diagram shows two circular type microstrip patches connected by metallized via holes located at their centers and separated by a ground plane and bonding film with permittivity of 3.88, loss tangent of 0.0236, and thickness of 0.1 mm. The diameter and height of the metallized via holes connecting the active patch and passive patch are 0.4 mm and 3.3 mm, respectively.

As shown in Fig. 1(b), the active microstrip antenna loaded with a circular type slot has two PIN diodes for phase switching operation. The passive microstrip antenna in Fig. 1(b) also has a circular slot to enhance operational bandwidth. A Taconic RF-35 substrate with permittivity of 3.5, loss tangent of 0.0018, and height of 1.6 mm was considered for our proposed design. Table 1 shows the dimensions of the proposed unit cell. Although two metallized via holes are sufficient for our design, we used four metallized via holes to keep the structure symmetrical. This configuration also reduces the cross-polarization level. One metallized via hole shown in Fig. 1(b) (forming the top of the active path to the bonding film) was used with the bias line that connects the PIN diodes and the power supply. The bias line has a width of 0.21 mm. Another metallized via hole (forming the top of the active path to bonding film) was kept as a dummy via hole. Both metallized via holes have a diameter of 0.4 mm

Table 1. Main features of the unit cell

Parameter	Value
Unit cell size	15 mm × 15 mm
Patch diameter	8.8 mm
Slot diameter	3.1 mm
Substrate	Taconic RF-35 (ε_r = 3.5, tanδ = 0.0018, h = 1.6 mm)
Bonding film	ε_r = 3.88, tanδ = 0.0236, h = 0.1 mm
Diameter of connecting via	0.4 mm
Diameter of bias vias	0.4 mm

and a height of 1.6 mm. As shown in Fig. 1(b), the PIN diodes are connected in such a way that they always stay in opposite biased conditions for any single biasing signal. Therefore, the slot on the active patch always stays in a short-circuited condition on one side.

III. Simulated Performance and Equivalent Circuit of the Unit Cell

The unit cell was simulated with the ANSYS Electronics Desktop simulator for both phase states. The unit cell was illuminated by a plane wave under normal incidence, with boundary conditions on the four walls of the boundaries. To present forward bias and reverse bias of the PIN diodes, an equivalent lumped RLC circuit model was used, and Fig. 2 shows the equivalent RLC circuit model of a PIN diode for the forward bias (L_{11} = 0.05 nH, R_{11} = 5.2 Ω for the forward bias condition, and for the reverse bias, L_{22} = 0.05 nH, R_{22} = 300 kΩ, C_{22} = 25 fF). In this paper, we used the label State1 when the PIN Diode 1 shown in Fig. 1(b) was in a reverse biased condition and PIN Diode 2 was forward biased. The opposite conditions were used for State2. The magnitude of transmission and reflection coefficients are depicted in Fig. 3, which shows that a −3 dB transmission bandwidth for State1 was 1.08 GHz (8.82–9.9 GHz), while it was 1.02 GHz (8.81–9.83) for State2. There was a slight difference between the simulated performance of the magnitude of transmission and reflection coefficients for State1

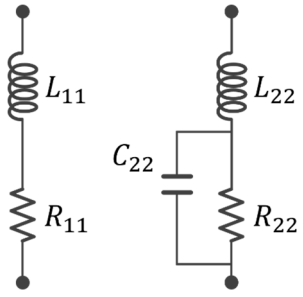

Fig. 2. Equivalent model of PIN diode for forward bias and reverse bias conditions.

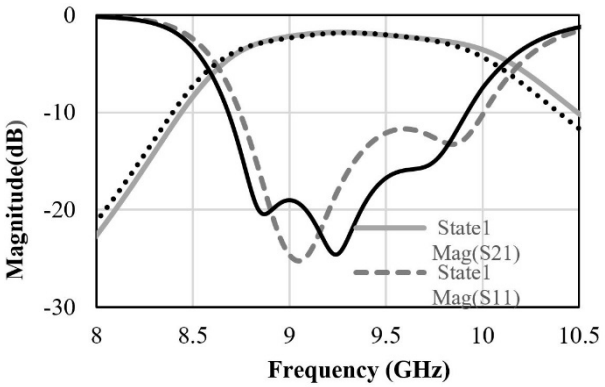

Fig. 3. Magnitude of *S*-parameters of the unit cell, obtained from the ANSYS Electronics Desktop simulations.

and State2. This may be due to the effect of the opening diameter on the ground plane, weak signal interaction between active and passive patches, and the asymmetric structure of the passive patch. The phases of the transmission coefficient are shown in Fig. 4. It can be seen that there was a phase shift of around 180° for State1 and State2 of the unit cell. At 9.1 GHz, phases of the transmission coefficients for State1 and State2 were 35.2° and −147.4°, respectively. The insertion loss at 9.1 GHz was −0.7 dB.

In Fig. 5, an equivalent circuit for the proposed unit cell is depicted. The slot-loaded circular patch on the top layer can be modeled by two impedances Z_1 and Z_2. Similarly, the slot-loaded circular patch on the bottom layer can be modeled by two impedances Z_6 and Z_5. The patches on the top and bottom

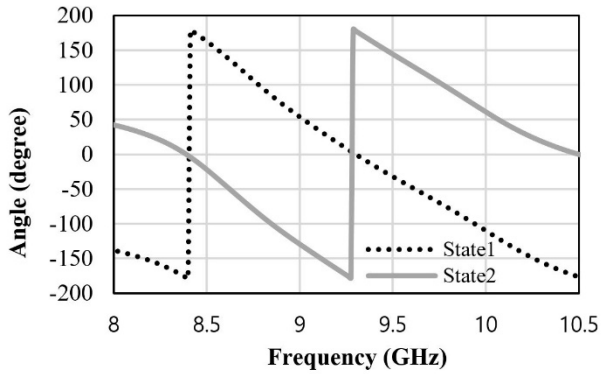

Fig. 4. Phases of the transmission coefficient of the unit cell obtained from the ANSYS Electronics Desktop simulations.

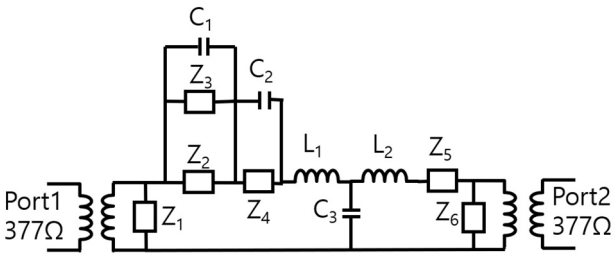

Fig. 5. Equivalent circuit of the 1 bit transmitarray unit cell.

layers are in the free space, which can be modeled as an ideal transformer with 377 Ω port impedance. The unit cell has two PIN diodes that are connected in such a way that while one PIN diode is in the forward bias condition, the other PIN diode is in a reversed bias condition. The forward bias and reverse bias conditions can be represented as equivalence impedances of Z_4 and Z_3, respectively. Furthermore, the PIN diodes have a bulk volume that gives additional capacitance, and a series capacitance C_1 and shunt capacitance C_2 are needed to compensate for the bulk volume of the PIN diodes.

IV. Design of Waveguide Transition Section and its Performance

The geometry of the waveguide WR-90 with transition section is shown in Fig. 6. The X band rectangular WR-90 waveguide has an opening area of 22.86 × 10.16 mm^2. But our proposed 2 × 2 elements transmitarray has an area of 30 × 30 mm^2, so it requires a transition section through which the signal can propagate at X band. Thus, we designed a rectangular WR-90 to square waveguide transition section. The cross-sectional view of the waveguide transition section is shown in Fig. 6. The cut-off frequency of the WR-90 waveguide for TE_{10} mode is 6.557 GHz, and the next highest order cut-off frequency for that waveguide is 13.114 GHz. The cut-off frequency for the 30 × 30 mm^2 section for the lowest order and next low order modes were 4.99 GHz and 6.24 GHz, respectively. However, because of the very small length of the transition section, the signal for the TE_{10} mode can propagate at the edge of the transition section without any significant attenuation.

The transition section was fabricated with copper material and is shown in Fig. 7. In the ANSYS Electronics Desktop simulator, the complete waveguide setup was simulated, and it was measured with an Agilent vector network analyzer and rectangular to square waveguide transition section. The simulated and measured transmission and reflection coefficients with the rectangular to square waveguide transition section are shown in Fig. 8.

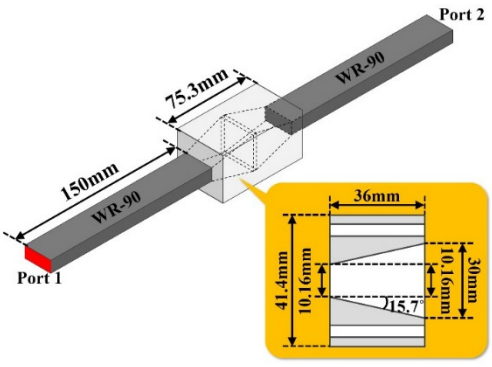

Fig. 6. The geometry of the waveguide transition section.

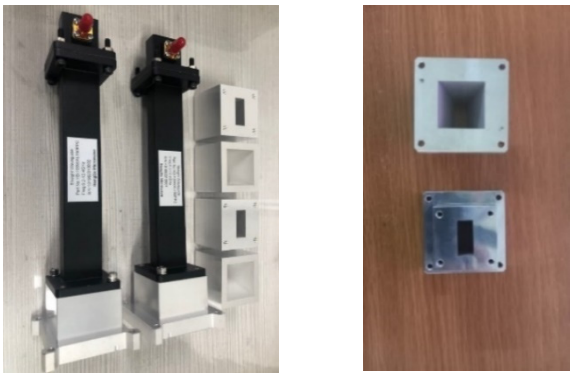

Fig. 7. Fabricated waveguide transition sections.

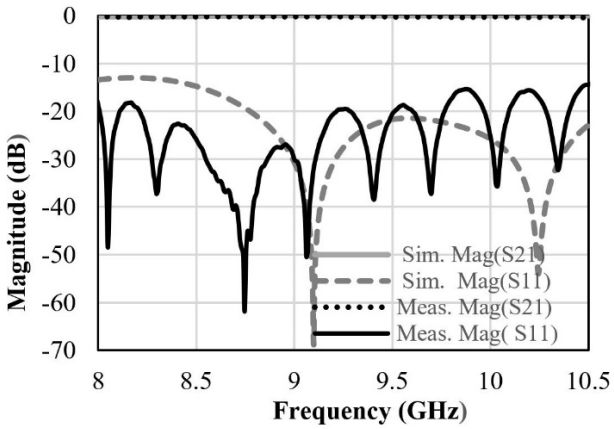

Fig. 8. Magnitudes of S_{11} and S_{21} with the transition section.

V. Design of 2 × 2 Elements Unit Cells with Biasing Line

Before designing the whole transmitarray, it was necessary to fabricate and measure the performances of the unit cell using the waveguide. To do this, we designed and fabricated 2 × 2 1-bit unit cells instead of a single 1 bit unit cell because of the simplicity of the waveguide transition section for 2 × 2 1-bit unit cells. Fig. 9, the top view of our proposed unit cells, shows

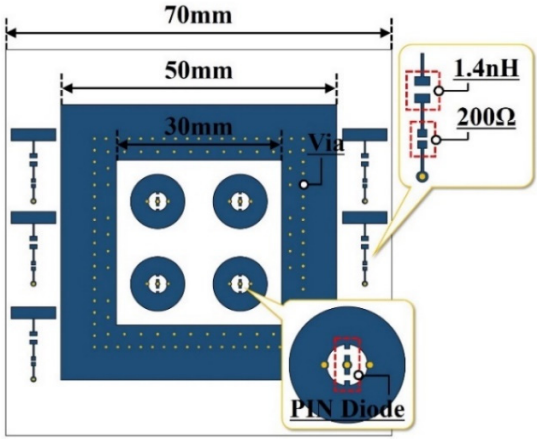

Fig. 9. Schematic top view of the 2 × 2 1-bit unit cells.

that the total structure was 70 × 70 mm^2. The large ground plane of 50 × 50 mm^2 and two rows of metallized via holes with a diameter of 0.4 mm each ensured continuity of the waveguide wall through the prototype.

There are four circular patches, each of which has two PIN diodes. A 10 V power source was used to feed the basing network for 2 × 2 unit cells. An inductor of 1.4 nH and a resistor of 200 Ω (self-resonant frequency at 10 GHz) were used to suppress the effect of the bias network. Fig. 10 shows the biasing line of our design. The biasing lines were kept inside the structure to minimize their effect on the unit cell performances, and it was found through simulation that the biasing line had no significant effect on the unit cell performances. As shown in Fig. 9, there are five connection lines: four connect to eight PIN diodes, and one is for the ground plane.

Fig. 11 shows the bottom view of the proposed 2 × 2 1-bit unit cells with four passive patches that receive the signal from a source and send to the active patch through the central metallized via hole. The top and bottom views of the fabricated prototype, with PIN diodes, chip inductor, and chip resistor, are shown in Fig. 12(a) and (b), respectively.

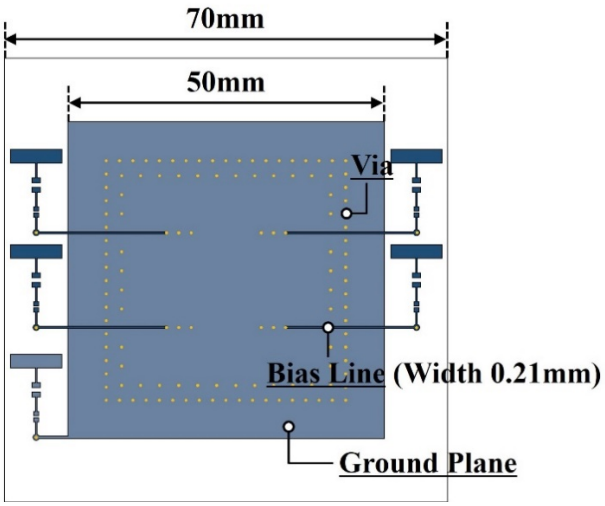

Fig. 10. Schematic of the biasing lines for our 2 × 2 1-bit unit cells.

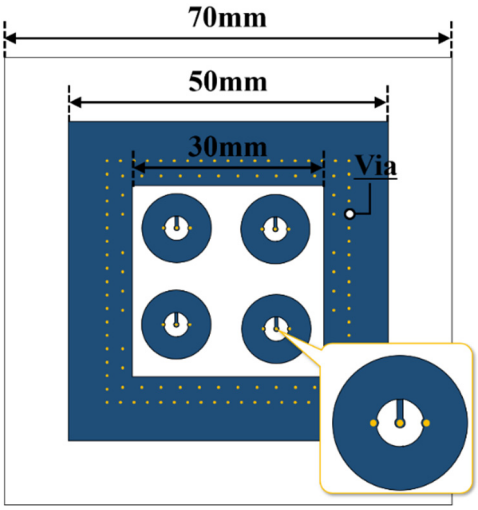

Fig. 11. Schematic bottom view of the 2 × 2 1-bit unit cell.

VI. Experiential Characterization of 4-Element Unit Cells

Fig. 13 shows the complete setup used to measure the performance of the 2 × 2 1-bit unit cells. This included an Agilent vector network analyzer, two X band WR-90 waveguides, two rectangular to square waveguide transition sections, and a voltage source. The voltage source was set at 10 V so that sufficient current could pass through the forward-biased PIN diode. The vector network analyzer was calibrated using the through-reflect-line (TRL) method. Fig. 14 shows the simulated and measured magnitudes of transmission coefficients for State1, and Fig. 15 shows the simulated and measured magnitudes of transition coefficients for State2.

At 9.1 GHz, the simulated and measured magnitudes of transmission coefficients for State1 were −1.8 dB and −1.4 dB, respectively. At the same frequency, the magnitudes of transmission coefficients were −1.6 dB and −1.6 dB, respectively, for State2. Thus, there was little difference between the simulated and measured results across the bandwidth. This can be due to

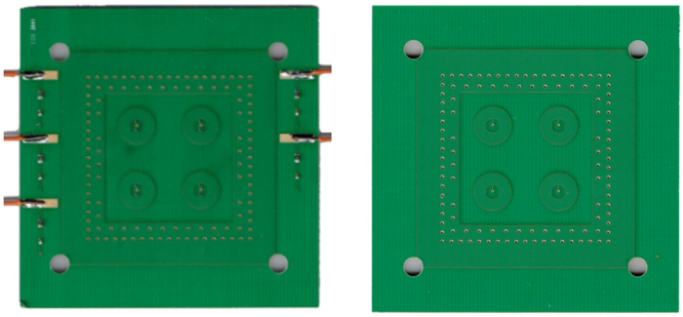

(a) (b)

Fig. 12. Fabricated 2 × 2 1-bit unit cells with PIN diode, chip inductor, and chip resistor: (a) top view, (b) bottom view.

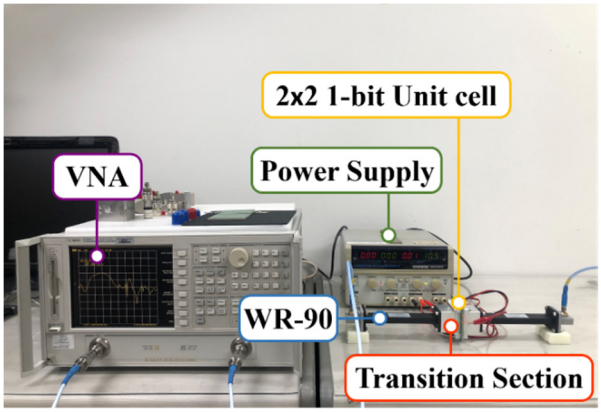

Fig. 13. Measurement setup with VNA and power supply.

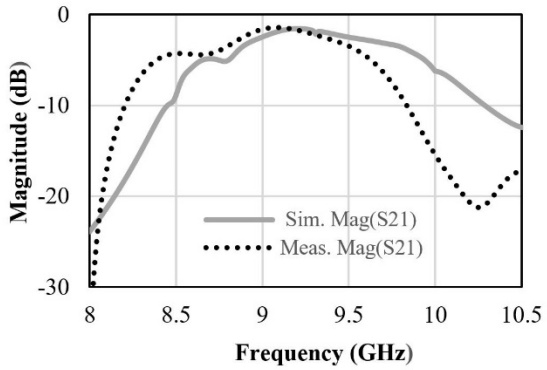

Fig. 14. Simulated and measured magnitudes of transmission coefficient for State1.

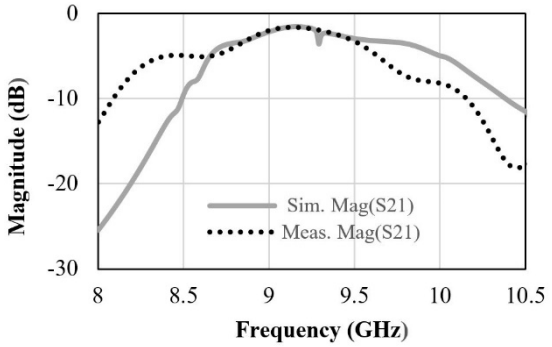

Fig. 15. Simulated and measured magnitude of transmission coefficients for State2.

fabrication errors in the unit cells and adding a coating material to the top and bottom layers during fabrication. The simulated and measured phases of the transmission coefficients for State1 and State2 are provided in Fig. 16. Using a Floquet mode approach, the simulated results showed −3 dB bandwidth for 1.08 GHz. Figs. 14 and 15 show narrowly different simulated and measured results using the waveguide and the rectangular to square waveguide transition. These differences were due to the imperfect rectangular to square transition section.

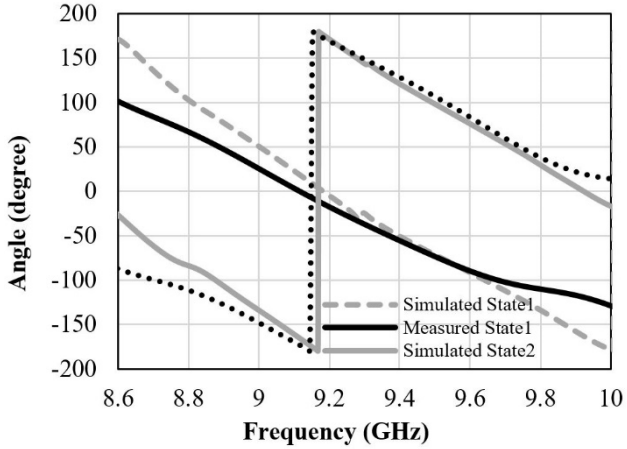

Fig. 16. Simulated and measured phases of transmission coefficients for State1 and State2.

We compared our proposed unit cell with the 1 bit unit cells (having PIN diodes) shown in Table 2, which were used in earlier studies found in the literature. Our proposed 1 bit transmitarray has two PIN diodes, while most of the previously proposed 1 bit unit cells had varactor diodes. However, to make a unit cell completely digital, one needs to use a PIN diode. Most 1 bit unit cells have very narrow transmission bandwidth. For instance, [1] reported a bandwidth of 1.50 GHz with an insertion loss of −1.87. Our proposed transmitarray has a bandwidth of 1.08 GHz with an insertion loss of − 0.7 dB. As shown in Fig. 17, the unit cell simulated in free space using the Floquet mode shows good agreement with the results of the unit cells simulated using a waveguide transition. This shows that measuring in this way gives accurate results.

VII. Conclusion

In this paper, a new type of electronically reconfigurable unit cell with two phase states was proposed. The proposed cell had a 1.08 GHz transmission bandwidth with constant phase shift and low insertion losses in the operating bandwidth. A circular patch and a circular type slot were used for this unit cell.

We also proposed a new method for experimental characterization of a transmitarray using the 2 × 2 1-bit unit cell. The prototype was tested successfully using an X band waveguide and rectangular to square waveguide transition section. This

Table 2. Comparison of our proposed unit cell with other unit cells (considering 1 bit unit cell with PIN diode)

	Transmission bandwidth (GHz)	Insertion loss (dB)	Unit cell size (mm^2)
Proposed unit cell	1.08	−0.70	0.45λ × 0.45λ
Clemente et al. [1]	1.50	−1.87	0.5λ × 0.5λ
Nguyen and Pichot [10]	n/a	n/a	0.54λ × 0.54λ

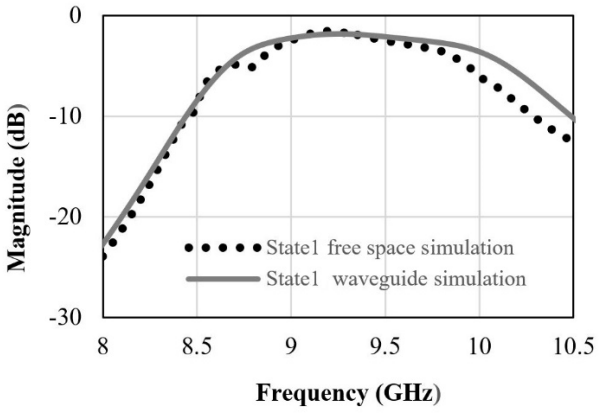

Fig. 17. Simulated magnitudes of transmission coefficients for State1 in free space and in the waveguide model.

method allows for checking the performance of the unit cells initially without having to fabricate an entire transmitarray antenna. A large array of this unit cell placed in front of a conventional horn antenna or any other suitable antenna with a specific focal length to diameter ratio can be used as a beamforming module, and the unit cell characterization method described in this paper can be applied to any type of unit cell in a transmitarray. The proposed transmitarray is only our initial work. We would like to design a transmitarray with a horn antenna, which will have both beam steering and polarization conversion properties. The circular-shaped allows us to make polarization conversion happen at the same frequency band because of its symmetrical structure. This cannot be achieved using a rectangular patch, because it is impossible to obtain vertical linearly polarized and horizontal linearly polarized beams at the same frequency band.

This research was supported by Basic Science Research Program (No. 2020R1I1A3057142), the Priority Research Centers Program (No. 2019R1A6A1A03032988) through the National Research Foundation of Korea, and the research grant of the Kongju National University in 2020.

REFERENCES

[1] A. Clemente, L. Dussopt, R. Sauleau, P. Potier, and P. Pouliguen, "1-Bit reconfigurable unit cell based on PIN diodes for transmit-array applications in X-band," *IEEE Transactions on Antennas and Propagation,* vol. 60, no. 5, pp. 2260–2269, 2012.

[2] A. Clemente, L. Dussopt, R. Sauleau, P. Potier, and P. Pouliguen, "Wideband 400-element electronically reconfigurable transmitarray in *X band*," *IEEE Transactions on Antennas and Propagation*, vol. 61, no. 10, pp. 5017–5027, 2013.

[3] M. Wang, S. Xu, F. Yang, and M. Li, "Design and measurement of a 1-bit reconfigurable transmitarray with subwavelength H-shaped coupling slot elements," *IEEE Transactions on Antennas and Propagation*, vol. 67, no. 5, pp. 3500–3504, 2019.

[4] M. Pan, C. Huang, X. Ma, B. Jiang, and X. Luo, "A dual linearly polarized transmitarray element with 1-bit phase resolution in X-band," *IEEE Antennas and Wireless Propagation Letters*, vol. 14, pp. 167–170, 2015.

[5] C. Huang, W. Pan, X. Ma, and X. Luo, "1-Bit reconfigurable circularly polarized transmitarray in X-band," *IEEE Antennas and Wireless Propagation Letters*, vol. 15, pp. 448–451, 2016.

[6] P. Padilla, A. Munoz-Acevedo, M. Sierra-Castaner, and M. Sierra-Perez, "Electronically reconfigurable transmitarray at Ku band for microwave applications," *IEEE Transactions on Antennas and Propagation*, vol. 58, no. 8, pp. 2571–2579, 2010.

[7] J. Y. Lau and S. V. Hum, "Analysis and characterization of a multipole reconfigurable transmitarray element," *IEEE Transactions on Antennas and Propagation*, vol. 59, no. 1, pp. 70–79, 2011.

[8] J. Y. Lau and S. V. Hum, "Reconfigurable transmitarray design approaches for beamforming applications," *IEEE Transactions on Antennas and Propagation*, vol. 60, no. 12, pp. 5679–5689, 2012.

[9] M. Frank, F. Lurz, R. Weigel, and A. Koelpin, "Electronically reconfigurable 6 × 6 element transmitarray at K-band based on unit cells with continuous phase range," *IEEE Antennas and Wireless Propagation Letters*, vol. 18, no. 4, pp. 796–800, 2019.

[10] B. D. Nguyen and C. Pichot, "Unit-cell loaded with PIN diodes for 1-bit linearly polarized reconfigurable transmitarrays," *IEEE Antennas and Wireless Propagation Letters*, vol. 18, no. 1, pp. 98–102, 2019.

[11] L. Di Palm a, A. Clemente, L. Dussopt, R. Sauleau, P. Potier, and P. Pouliguen, "Experimental characterization of a circularly polarized 1 bit unit cell for beam steerable transmitarrays at Ka-band," *IEEE Transactions on Antennas and Propagation*, vol. 67, no. 2, pp. 1300–1305, 2019.

[12] J. R. Reis, M. Vala, and R. F. Caldeirinha, "Review paper on transmitarray antennas," *IEEE Access*, vol. 7, pp. 94171–94188, 2019.

[13] D. McGrath, "Planar three-dimensional constrained lenses," *IEEE Transactions on Antennas and Propagation*, vol. 34, no. 1, pp. 46–50, 1986.

[14] E. Carrasco, M. Barba, and J. A. Encinar, "X-band reflectarray antenna with switching-beam using PIN diodes and gathered elements," *IEEE Transactions on Antennas and Propagation*, vol. 60, no. 12, pp. 5700–5708, 2012.

[15] M. Riel and J. J. Laurin, "Design of an electronically beam scanning reflectarray using aperture-coupled elements," *IEEE Transactions on Antennas and Propagation*, vol. 55, no. 5, pp. 1260–1266, 2007.

[16] H. Yang, F. Yang, S. Xu, M. Li, X. Cao, and J. Gao, "A 1-bit multipolarization reflectarray element for reconfigurable large-aperture antennas," *IEEE Antennas and Wireless Propagation Letters*, vol. 16, pp. 581–584, 2017.

[17] J. Y. Lau and S. V. Hum, "A wideband reconfigurable transmitarray element," *IEEE Transactions on Antennas and Propagation*, vol. 60, no. 3, pp. 1303–1311, 2012.

[18] E. Erdil, K. Topalli, N. S. Esmaeilzad, O. Zorlu, H. Kulah, and O. A. Civi, "Reconfigurable nested ring–split ring

transmitarray unit cell employing the element rotation method by microfluidics," *IEEE Transactions on Antennas and Propagation*, vol. 63, no. 3, pp. 1163–1167, 2015.

[19] C. C. Cheng, B. Lakshminarayanan, and A. Abbaspour-Tamijani, "A programmable lens-array antenna with monolithically integrated MEMS switches," *IEEE Transactions on Microwave Theory and Techniques*, vol. 57, no. 8, pp. 1874–1884, 2009.

Biswarup Rana

received the Ph.D. degree from the Indian Institute of Engineering Science and Technology (IIEST), Shibpur, India, in 2017. He was as a post-doctoral researcher at Seoul National University of Science and Technology, South Korea. Currently, he is working at Kongju National University, South Korea. His research interests include analysis and design of microstrip antennas, substrate integrated waveguide antennas, phased array antennas, dielectric resonator antennas, implantable antenna and transmitarray.

In-Gon Lee

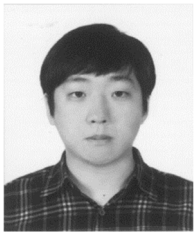

received his M.S. and Ph.D. degrees in information and communication engineering from Kongju National University, Cheonan, South Korea, in 2016 and 2020, respectively. Now, he is currently a post-doc research fellow at the same university, Korea. His research interests include periodic electromagnetic structures.

Ic-Pyo Hong

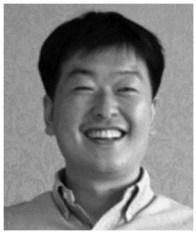

received the B.S., M.S., and Ph.D. degrees in electronics engineering from Yonsei University, Seoul, South Korea, in 1994, 1996, and 2000, respectively. From 2000 to 2003, he was with the Information and Communication Division, Samsung Electronics Company, Suwon, South Korea, where he was a Senior Engineer with CDMA Mobile Research. Since 2003, he has been with the Department of Information and Communication Engineering, Kongju National University, Cheonan, South Korea, where he is currently a Professor. In 2006 and 2012, he was a Visiting Scholar with the Texas A\&M University, College Station, TX, USA, and Syracuse University, Syracuse, NY, USA, respectively. His research interests include numerical techniques in electromagnetics and periodic electromagnetic structures.

JOURNAL OF ELECTROMAGNETIC ENGINEERING AND SCIENCE, VOL. 21, NO. 2, 161~164, APR. 2021

https://doi.org/10.26866/jees.2021.21.2.161
ISSN 2671-7263 (Online) · ISSN 2671-7255 (Print)

Theoretical Minimum Detection Range for a Rapidly Moving Target and an Experimental Evaluation

Ilkyu Kim[1] · Hyun Kim[2] · Jeong-Hae Lee[3,*]

Abstract

There have been considerable challenges with radar systems for detecting high-speed projectiles at a short range. This necessitates the presentation of a guideline for the minimum detection range that will guarantee detection of a target. In this letter, the detection range for a rapidly flying target is studied based on the characteristics of the target, such as speed and launch angle, and radar parameters such as pulse repetition interval, dwell time, beamwidth, and so on. The derived equation was applied to parametric studies for different characteristics of targets in order to investigate the influential parameters that affect the minimum detection range. A field test using the radar system's prototype was performed to evaluate the validity of the proposed equation.

Key Words: Minimum Detection Range, Radar System, Rapid Target.

I. Introduction

One of the important functions of a radar system is the detection of a fast-moving target launched from the ground. The probability of detecting a target is mostly determined by parameters such as the frequency band, antenna type, and waveforms. A radar system is capable of sequentially allocating a pencil-shaped beam to sectors along a horizontal line. When a launched object passes over the sectors, the radar system can detect it, track its path, and provide queuing information (position, direction, speed, etc.). A radar system needs to recognize the presence of a rapidly moving target before it quickly passes through the search sector. For such an application, the minimum detection range is a function of various parameters such as target speed and launch angle, including the pulse repetition interval (PRI), beamwidth, and dwell time. However, previous studies have focused on the calculation of the minimum range based on the blindness of the receiver, which is determined by the transmit pulse width [1]. Alert–confirm detection has been investigated with respect to optimum dwell time and reduced false alarm probabilities [2]. However, to the best of our knowledge, no comprehensive research has been conducted that focused on the range of detection and took into account the characteristics of the target.

In this letter, the minimum detection range of a radar system is studied based on the geometry of the target. A radar system often fails to detect a rapid object at a short range that is greater than the one calculated by the blindness of the receiver. This work deals with a projectile that can move at a speed of hundreds of meters per second. In order to avoid missing such a target, it is necessary to provide guidelines on the minimum detection ranges for rapidly moving targets. This letter discusses

Manuscript received March 17, 2020 ; Revised December 29, 2020 ; Accepted March 12, 2021. (ID No. 2020317-033J)
[1]C4I Team, Defense Agency for Technology and Quality, Jinju, Korea.
[2]Radar R&D, LIG Nex1 Co., Yongin, Korea.
[3]Department of Electronics and Electrical Engineering, Hongik University, Seoul, Korea.
[*]Corresponding Author: Jeong-Hae Lee (e-mail: Jeonglee@hongik.ac.kr)

theoretical derivations and parametric studies on the minimum detection range, as well as the results of field tests that were conducted to validate the calculations.

II. Derivation of Minimum Detection Range

The minimum detection range can be derived as an aspect of the pulse width of the transmitter and the geometries of the target detection. First, a receiver is restricted to listening to returning echoes during the pulse width of the transmitter. This blindness of the receiver leads to a minimum detection range of

$$R_{min} = \frac{\tau_t c}{2} \tag{1}$$

where τ_t is the pulse width of the transmitter, and c is the speed of light. Second, the detection range is derived from the geometry of the detection as described in Fig. 1.

In order to meet the requirements for the probability of detection, an adequate number of PRI beams must be in use when the target passes through the sectors along a horizontal line. Thus, the time duration T_{pass} can be defined as

$$T_{pass} \geq N_{PRI} \times T_{scan} \tag{2}$$

The scanning time duration T_{scan} can be written as

$$T_{scan} = N_{sector} \times T_{dwell} \tag{3}$$

where N_{sector} is the number of sectors covered by the radar above the horizontal line, and T_{dwell} is the length of time that a pencil beam dwells in each sector. The duration that T_{pass} will be passing through the beam cross-section can then be calculated based on the geometries depicted in Fig. 1 by using Eq. (4).

$$T_{pass} = \frac{R \times \sin(\theta_{el}/2)}{M_v \times \sin\theta_t}\left(\frac{1}{\sin\left(\theta_t + \theta' + \frac{\theta_{el}}{2}\right)} + \frac{1}{\sin(\theta_t + \theta')}\right) \tag{4}$$

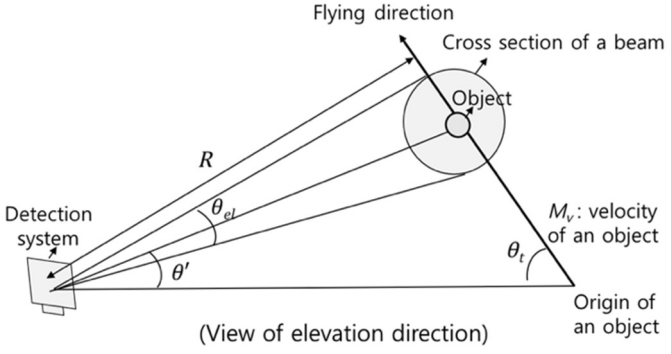

Fig. 1. Geometries of a rapidly moving object.

where M_v and θ_t are the speed and launch angle for the object, respectively, and R and θ_{el} are the detection range from the radar system to the object and the 3 dB beamwidth for the radar system, respectively. The angle θ' is the elevation angle between the ground and the target. For surveillance radar systems, the detection is made along a horizontal line, which assumes that the angle θ' is zero. The parametric studies discussed in Section III were performed based on the assumption that substituting Eqs. (3) and (4) into Eq. (2) will produce the detection range R (Table 1). The minimum detection range R_{min} can be defined as the smallest detection range R by using the following equation.

$$R_{\min} = \frac{M_v}{\sin(\theta_{el}/2)}\left(\frac{1}{\sin\left(\theta_t + \theta' + \frac{\theta_{el}}{2}\right)} + \frac{1}{\sin(\theta_t + \theta')}\right)^{-1} \times N_{PRI} \times N_{sector} \times T_{dwell} \tag{5}$$

The derivation in Eq. (5) is based on the assumption that the signal-to-noise ratio (SNR) is satisfied because the detection range of interest is much closer than the maximum one. The minimum detection range in Eq. (5) can be used when the range is greater than the blind range in Eq. (1).

III. Parametric Studies on the Detection Range

It is desirable to reduce the minimum detection range in terms of the operational aspects of a target detection system. In principle, the minimum detection ranges can be defined based on Eq. (1), as with the representative examples provided in the following:

i) PRI = 350 μs, Tx pulse width = 35 μs, and R_{min} = 5.25 km.
ii) PRI = 200 μs, Tx pulse width = 20 μs, and R_{min} = 3 km.

When the above ranges are smaller than the ones obtained from the geometries of the rapidly moving object, the radar system is likely to miss the target at the above range. The geometry

Table 1. Typical parameters of detection systems and objects

Parameter	Value
M_v (m/s)	300−800
θ_t (deg)	30−60
T_{dwell} (ms)	7.1−9.1
θ_{el} (deg)	1−7
N_{PRI}	3−5
N_{sector}	25−40

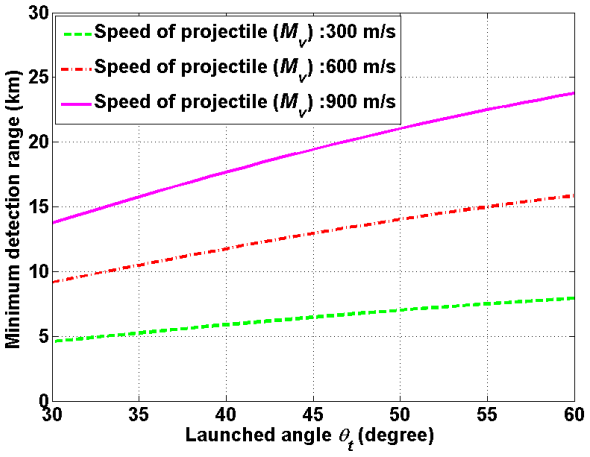

Fig. 2. Minimum detection range in terms of M_v and θ_t.

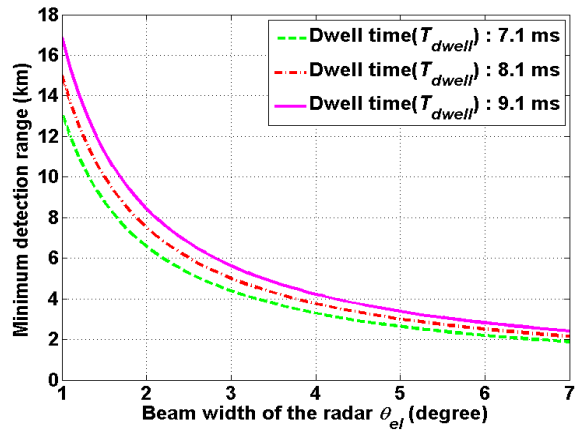

Fig. 3. Minimum detection range in terms of T_{dwell} and θ_{el}.

of the target can be emphasized more for a system in which it is required to detect a projectile moving at high speeds. The first case of the study was the calculation of the minimum range according to the launched angle and the speed of the projectile. As illustrated in Fig. 2, when the launch angle was increased, the minimum range also increased due to a reduction of T_{pass} for each beam sector. In addition, it was observed that a faster target led to a higher minimum detection range. The parameter settings T_{dwell} = 7.1 ms, θ_{el} = 2.0°, N_{sector} = 30, and N_{PRI} = 5 were used for this case study. The second case involved the settings of the beamwidth and dwell time. As shown in Fig. 3, the exploitation of a greater beamwidth allowed the T_{pass} in each beam sector to be increased. It was observed that an increase in the duration T_{pass} reduced the minimum detection range. In contrast, the use of a longer dwell time increased an entire duration of the search with all beam sectors. The longer dwell time led to the increase in the minimum detection range. Note that the parameter settings θ_t = 46°, M_v = 300 m/s, N_{sector} = 30, and N_{PRI} = 5 were used in this evaluation.

The third case was the calculation of the minimum detection range in terms of the number of sectors and PRI beams. Fig. 4 depicts the variation of the minimum detection range with respect to the number of sectors and PRI beams. The minimum detection range increased as the number of sectors and/or PRI beams increased. This is because more assigned sectors and PRI beams led to an increase in the search duration. The parameter settings T_{dwell} = 7.1 ms, θ_{el} = 2.0°, θ_t = 46°, and M_v = 300 m/s were used in the last case study.

The field test was performed using the prototype of a radar system. Fig. 5 shows the trajectory of a projectile obtained by the field test. The radar system tracked a flying projectile until the detection range was as short as possible. The distance between the radar system and the origin of the object was set as 5 km, and the validity of the calculated minimum range R_{cal} was verified by comparing it to the minimum range R_{mea} measured in the field test. The minimum detection range obtained from the trajectory in Fig. 5 is the first case provided in Table 2, which reveals that both cases showed agreement at less than 5% deviation. This radar system was designed to search and track above the horizontal line to reduce adverse effects from geometric clutter. The short-range detection is less affected by time variances in atmospheric reflectivity and any estimation error.

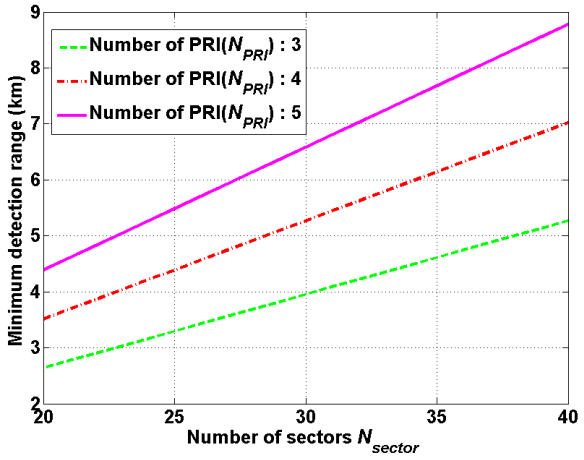

Fig. 4. Minimum detection range in terms of N_{sector} and N_{PRI}.

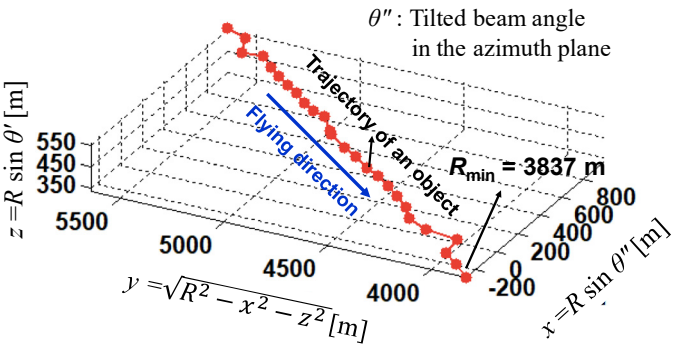

Fig. 5. The projectile trajectory as measured with a field test.

Table 2. Comparison of calculated and measured results

	R_{cal}(km)	R_{mea}(km)
Case 1 (M_v = 297 m/s, θ_t = 18°, N_{PRI} = 4)	3.62	3.8
Case 2 (M_v = 350 m/s, θ_t = 23°, N_{PRI} = 4)	5.35	5.4

IV. Conclusion

In this letter, a simple equation for the minimum detection range of a rapidly moving target was derived based on the geometry of the rapid movement. The use of this formula means that parametric studies could be performed to determine the minimum detection range, and our field test results validated the effectiveness of the equation.

Ilkyu Kim

received his B.S. degree in electrical engineering from Hongik University, Seoul, South Korea in 2003 and the M.S. degree in electrical engineering from University of Southern California, Los Angeles, CA in 2006 and Ph.D. degrees in electrical engineering from University of California at Los Angeles in 2012. He was with Samsung Advanced Institute of Technology from 2006 to 2008. After gaining his Ph.D. degree, he joined in Defense Agency for Technology Quality where he is currently working as a team leader of C4I technology planning team. His research interests include but not limited to computation of electromagnetic mutual coupling, antenna measurement, and antenna design for space and radar applications.

Hyun Kim

Photograph and biography not available at the time of publication.

The research work of the author Jeong-Hae Lee was supported by Basic Science Research Program through Ministry of Education (No. 2015R1A6A1A03031833).

References

[1] S. H. Al Sadoon and B. H. "Radar theoretical study: minimum detection range and maximum signal to noise ratio (SNR) equation by using MATLAB simulation program, " *American Journal of Modern Physics*, vol. 2, no. 4, pp. 234–241, 2013.

[2] E. H. Kim and J. Park, "Dwell time optimization of alert-confirm detection for active phased array radars," *Journal of Electromagnetic Engineering and Science*, vol. 19, no. 2, pp. 107–114, 2019.

Jeong-Hae Lee

received B.S. and M.S. degrees in electrical engineering from Seoul National University in Korea in 1985 and 1988, respectively, and a Ph.D. degree in electrical engineering from the University of California, LA in 1996. From 1993 to 1996, he was a visiting scientist of general atomics in San Diego, CA, where his major research initiatives were developing a millimeter-wave diagnostic system and studying plasma wave propagation. Since 1996, he has been working at Hongik University in Seoul, Korea as a professor in the Department of Electronic and Electrical Engineering. He has more than 100 papers published in journals and 60 patents. He was a president of the Korea Institute of Electromagnetic Engineering and Science in 2019. He is currently a director of the Metamaterial Electronic Device Center. His current research interests include metamaterial radio frequency devices and wireless power transfer.

https://doi.org/10.26866/jees.2021.21.2.e
ISSN 2671-7263 (Online) · ISSN 2671-7255 (Print)

Erratum to "Characterization of a 1 mm (DC to 110 GHz) Calibration Kit for VNA"

Chihyun Cho* · Jin-Seob Kang · Joo-Gwang Lee · Hyunji Koo

In the paper entitled "Characterization of a 1 mm (DC to 110 GHz) Calibration Kit for VNA (*Journal of Electromagnetic Engineering and Science*, vol. 19, no. 4, pp. 272–278, 2019)", a typographical error occurred in Equation (7). The correct equation follows:

$$R_i = \omega L_i = \left(\frac{1}{\pi d} + \frac{1}{\pi D} \right) \sqrt{\frac{\omega \mu_0 \mu_r}{2\sigma}} \tag{7}$$

Group for Electromagnetic Wave Metrology, Division of Physical Metrology, Korea Research Institute of Standards and Science, Daejeon, Korea.
*Corresponding Author: Chihyun Cho (e-mail: chihyun.cho@kriss.re.kr)

JEES Journal of
Electromagnetic Engineering and Science

Instructions for Authors

Journal of Electromagnetic Engineering and Science (*J. Electromagn. Eng. Sci.*; *JEES*) is an official English journal of the Korean Institute of Electromagnetic and Engineering Science (KIEES). The objective of *JEES* is to publish academic as well as industrial research results and foundings on electromagnetic engineering and science. The journal covers all aspects of researches and technology related to electromagnetics: Electromagnetic Compatibility/Electromagnetic Interference, Microwave and Millimeter-Wave Engineering, Antenna and Propagation, Electromagnetic Theory, Wireless Communication, Lightwave and Electro-Optics, Materials and Components, Software Defined Radar, Radar, Bioelectromagnetics, and etc.

I. Copyright and Creative Commons Attribution Licensing

The copyright and the transfer rights of the digital content of published papers and the journal is owned by the KIEES. All published materials are also assigned a Creative Commons Attribution License (http://creativecommons.org/licebses/by-nc/4.0/). The journal accepts manuscripts for consideration with the understanding that the manuscript has not been published previously and is not currently under consideration for publication elsewhere, and in addition, that the authors (or their employer, if it holds the copyright) are authorizing the transfer of the copyright to the Institute when the manuscript is submitted. Author should check the copyright transfer conditions and forms at http://www.jees.kr.

II. Research and Publication Ethics

Research published in *JEES* must have followed institutional, national, and international guidelines. For policies on research and publication ethics that are not stated in these instructions, please refer to the *Committee on Publication Ethics* (*COPE*) *Guidelines* (http://publicationethics.org/resources/code-conduct).

1. Originality and Duplicate Publication

A manuscript submitted for publication in *JEES* should be an original work with technical values. It must not have been previously published and is not under consideration for publication elsewhere. *JEES* assumes that the materials submitted for its publications are properly available for general dissemination for the readership of those publications. It is the responsibility of the authors, not *JEES*, to determine whether disclosure of their materials requires prior consent of other parties and, if so, to obtain it. If an author uses charts, photographs, or other graphics from any previously printed materials, he/she is responsible for obtaining written permissions from the publisher to use them in his/her manuscript. Responsibility for the contents of published papers rests upon the authors, not *JEES*.

2. Conflict of Interest

Authors are required to complete a declaration of conflict of interests. All conflict of interests that are declared will be listed at the end of published articles.

3. Authorship

Authorship should be restricted to those individuals who have met each of the following three criteria:
1) made a significant contribution to the conception and design of the project, or the analysis and interpretation of the data, or other substantial scholarly effort; 2) participated in drafting, reviewing and/or revising the work; and 3) approved the final version for publication. After the initial submission of a manuscript, any changes whatsoever in authorship (adding author(s), deleting author(s), or re-arranging the order of authors) must be explained by a letter to the editor from the authors concerned. The content of this

letter must be acknowledged and agreed upon by all of the authors of the paper.

If you accept the policies on research and publication issued by KIEES, authors must click the response of "The Code of Research Ethics" through online.

III. Submission of Manuscripts

Authors are expected to be members of the KIEES except for some special cases approved by the Editorial Board of KIEES. All manuscripts should be submitted electronically through the online submission and review site (https://mc03.manuscriptcentral.com/jees). For the first submission, you may be required to create an account on the submission site. A manuscript can be submitted at any time of the year. When submitting a manuscript, authors need to make sure that their manuscripts do not provide any of their identities such as authors' names and affiliations as the review is double-blinded. More detailed submission instruction is available in the upper right corner of the submission site. All manuscripts submitted to the Journal must comply with the instruction and the standard format of the Journal. Otherwise, it will result in return of the manuscript and possible delay in publication. For assistance, please contact us via e-mail (admin-jees@kiees.or.kr).

IV. Peer Review Process

The manuscript will be forwarded to three reviewers selected for their expertise in the field of the submitted manuscript. The acceptance criteria for all papers are based on the quality and originality of the research and its clinical and scientific significance. During the review process, the author is often asked to expand, rewrite, or clearly explain the specific contents of his/her paper. It is not uncommon that an author is asked to provide another draft with the suggested changes for further review. A revised manuscript should be submitted to the homepage within a month from the date on which any change of the manuscript is requested to the author. Once a manuscript has received the final approval of the reviewers and Editor-in-Chief, the author will be notified and asked to prepare the manuscript for final publication and to possibly complete an additional information form.

V. Publication Type

The papers are classified into five categories.

Regular Paper should be an original work that contributes to the academic interests of the KIEES members with technical values. The paper should also be written within 12 pages with A4 size including figures, charts, and tables (The main body of text consists of two columns).

Letter consists of reports of preliminary results or short reports on completed work that are of current interest to many researchers in the field. Comments on material previously published in the journal, suggestions for new directions, and errata could be included. Their length must be less than 3 pages (with a two-column format) including paper title, author affiliation, reference, etc.

Review Paper will be published by direct submission as well as from invited experts. In both cases, the work will be subject to editorial review. Review papers should critically review topics not only to inform the reader of the background, but also to communicate the state of the art and outstanding research problems.

Technical Report is on innovative technical achievements of interest to the community and usually a report of an extensive series of measurements. Report is often involving display in the form of tables or graphs, with text describing the conditions and procedures of measurement.

Editorial is a brief report of research findings adequate for the journal's scope and of particular interest to the community.

VI. Manuscript Preparation

All manuscripts must be written in MS-Word and adhere to the following guidelines:

1. A cover of each paper manuscript should include a title, authors' names (main author and co-authors), author's organizations, contact information (e-mail and phone number), and the author's area of expertise.

2. The first page of a main text should only contain title, abstract with a length of about 150 words, and key words with around five words.
3. The contents of the manuscript should be arranged in the order of abstract, main text, acknowledgments, references, and appendix.
4. The numbers corresponding to chapters in the manuscript should be written in Roman numerals (I, II, III, IV...) and the numbers corresponding to sections should be written in Arabic numerals (1, 2, 3, 4...).
5. Equation numbers should be given in Arabic numerals enclosed in parentheses on the right-hand margin. They should be cited in the text as, for example Eq. (1) or Eqs. (1)-(3).
6. All tables should be numbered consecutively with Arabic numerals. They should be referred to in the text and should be numbered according to their order of mention in the text. In addition, all tables should, not only list all abbreviations in the table in footnotes at the end, but also have a title that is concise and describes the table's contents. Vertical lines are not used. The table should be self-explanatory and supplement, not duplicate, the text. If the table or any data therein have been published, a footnote to the table must give permission information to the original source. The structure should be clear, with simple column headings giving all units. A table should not exceed one page when printed. Use lowercase letters in superscripts $^{a,b,c...}$ for special remarks.
7. All figures should be of high quality meeting with the publishing requirement with legible symbols and legends. In preparing the figures, authors should consider a size reduction during the printing process to have acceptable line clarity and character sizes. Use only figures that are necessary to illustrate the meaning of the text. Figures must be black and white of high contrast. All figures should be referred to in the text as, for example, Fig. 1, Fig. 2(a), or Figs. 1-3.
8. Only those references cited in the text should be listed in the references. Authors are responsible for the accuracy and completeness of their references and the correct text citations. In the text the reference should be numbered in bracket in ascending order (e.g., [1, 3], or [4-6]; Lee [2] and Kim and Park [5]; Jang et al. [7]). In case of the paper title, only the first letter is to be capitalized. However, in case of journal and book titles, the first letter of each word should be capitalized and all of the letters should be italicized. See the example below.

Books

[1] F. Giannini and G. Leuzzi, *Nonlinear Microwave Circuit Design.* NewYork, NY: John Wiley & Sons Inc., 2004.

Journals

[2] H. Ahn and B. Kim, "Equivalent transmission-line sections for very high impedances and their application to branch-line hybrids with very weak coupling power," *Journal of Electromagnetic Engineering and Science*, vol. 9, no. 2, pp. 85-97, 2009.

Report

[3] E. E. Reber, R. L. Michell, and C. J. Carter, "Oxygen absorption in the earth's atmosphere," Aerospace Corp., Los Angeles, CA, Tech. Rep. TR-0200 (4230-46)-3, Nov. 1988.

Conference Proceedings

[4] S. P. Bingulac, "On the compatibility of adaptive controllers," in *Proceedings of the 4th Annual Allerton Conference on Circuit and System Theory*, NewYork, pp. 8-16, 1994.

Papers Presented at Conferences

[5] J. G. Kreifeldt, "An analysis of surface-detected EMG as an amplitude-modulated noise," presented at the 8th International Conference on Medical and Biological Engineering, Chicago, IL, 1969.

[6] J. Arrillaga and B. Giessner, "Limitation of short-circuit levels by means of HVDC links," presented at the IEEE Summer Power Meeting, Los Angeles, CA, Jul. 1990.

Theses (M.S.) and Dissertations (Ph.D.)

[7] N. Kawasaki, "Parametric study of thermal and chemical nonequilibrium nozzle flow," M.S. thesis, Department of Electronic Engineering, Osaka University, Osaka, Japan, 1993.

[8] J. O. Williams, "Narrow-band analyzer," Ph.D. dissertation, Department of Electronic Engineering, Harvard University, Cambridge, MA, 1993.

Standards

[9] *IEEE Criteria for Class IE Electric Systems*, IEEE Standard 308, 1969.

Online Sources

[10] R. Bartle, "Early MUD History," Nov. 1990; www.ludd.luth.se/aber/mud-history.html.

9. When citing any paper published in JEES, it should be indicated the name of the journal as *Journal of Electromagnetic Engineering and Science* or *J. Electromagn. Eng. Sci*.

10. Acknowledgment, if needed, appears before the reference. Sponsorship or financial support acknowledgment should be included here.

11. Unit and Abbreviation:If the authors describe length, height, weight, and volume, they should use standard metric units. Temperature should be given in degrees Celsius. All other units should follow the International System of Units (SI). All units must be preceded by one space except percentages (%) and temperatures (°C).

Abbreviations must be used as an aid to the reader, rather than as a convenience of the author, and therefore their use should be limited. Generally, abbreviations that are used less than 3 times in the text, including tables and figure legends, should be avoided. Standard SI abbreviations are recommended. Other common abbreviations are as follows (the same abbreviations are used for plural forms): h (hour), min (minute), s (second), d (day), wk (week), mo (month), y (year), L (liter), mL (milliliter), μL (microliter), g (gram), kg (kilogram), mg (milligram), μg (microgram), ng (nanogram), pg (picogram), *g* (gravity; not g), nm (nanometer), μm (micrometer), mV (millivolt), mA (milliampere), mW (milliwatt), C (coulomb), μF (microfarad), mH (millihenry), n (samplesize), SD (standard deviation of the mean), and SE (standard error of the mean).

VII. Accepted Manuscript

Once the review process has been completed with a decision of acceptance, the final manuscript accommodating all of the reviewers' comments should be submitted along with photos of the authors and their brief biographies (including major research areas). The accepted papers will be published, in principle, in the order of initially submitted dates subject to decision of the Editorial Board.

1. Page Proofs

Authors will be given an opportunity to review the laser printed version of their manuscripts before printing. One set of page proofs in PDF format will be sent by e-mail to the corresponding author. The review should be solely dedicated to detecting typographical errors.

2. Publishing Charge

The publishing charge for general publishing is KRW 450,000 (USD 450) for up to the first 6 pages. For 7 to 8 pages, an extra charge of KRW 120,000 (USD 120) per page is applied. For 9 pages or more, an extra charge of KRW 160,000 (USD 160) per page is applied. Twenty reprints without a cover will be supplied without an additional charge. With a corresponding author who is non-member of the KIEES, an additional charge of KRW 100,000 (USD 100) will be applied to the total charge. The guidance of the KIEES membership enrollment can be found in the link below.
(https://www.kiees.or.kr/html/?pmode=MemberInfo#)

Contact Us

Editorial office of the Korean Institute of Electromagnetic Engineering and Science
217, Saechang-ro, Yongsan-gu, Seoul, 04376, Korea
Tel: +82-2-337-9666/332-9665 Fax: +82-2-6390-7550
http://www.jees.kr, E-mail: admin-jees@kiees.or.kr

https://www.kiees.or.kr

Call for Papers

※ Hybrid (Online/Offline) Conference

The Korean Institute of Electromagnetic Engineering and Science (KIEES)

Summer Conference 2021

August 18 (Wed.) ~ August 21 (Sat.) 2021
Ramada Plaza Jeju, Jeju Island, Republic of Korea

Important Dates

Paper Submission Deadline : June 25 (Fri.) 2021
Notification : July 23 (Fri.) 2021
Early Bird Registration : July 26 (Mon.) ~ August 6 (Fri.) 2021

Topics of Interest

(1) EMI/EMC/EMP	(2) EM Theory & Computational EM	(3) Microwave/mmWave Passive Circuits
(4) Microwave/mmWave Active Circuits	(5) EM Components and Materials	(6) Radio Wave Propagation & Scattering
(7) Antenna Theory & Design	(8) THz/Optical Systems & Components	(9) IoT & Sensor Network
(10) Radar & Remote Sensing	(11) CR/SDR	(12) EM Bio-effects & EMF
(13) Biomedical Applications	(14) Satellite and Cosmic Radio Waves	(15) Wireless Communication Systems
(16) Radio & Broadcasting Policies/Standards	(17) EM Measurement	(18) Wireless Power Transfer & Energy Harvesting
(19) Electronic Warfare & EM Security	(20) Broadcasting Technologies/Applications	(21) Technologies for 5G & Beyond, AI & Deep Learning for EM Applications

* Presentation Time
- Oral presentations : 15 minutes (Including Q&A) - Poster presentations : 1 hour

Submission Details

- All papers (general/special sessions, invited and undergraduate student papers) can be written in English. The length is restricted to one page (A4).
  ※Papers submitted for the Best Paper Award (AP/EMC/MTT) can be written in two pages (A4).
  ※It is requested to choose the presentation type as oral presentation to apply for the Best Paper Award. Note that this guideline is not applicable to undergraduate students. The poster presentation type is only available option for undergraduate students.
- Submission Method : Please visit the webpage of the KIEES (http://www.kiees.or.kr) and log in with your credentials. You can submit the paper(s) at "Detailed Information for the Conference"
- Writing Form (Template) : Download this form from the submission page on the KIEES's website. --> Use the template available from the submission page of the webpage of the KIEES.
- Presentation Form : Either oral or poster presentation can be chosen during the online submission. The presenter's choice will be considered as a top priority, however, please note that the presentation type might be changed by TPC due to the limited session time and space. The corresponding author will be notified with the presentation type with the final acceptance letter.
  ※It is requested to join the membership of the KIEES to submit the papers.

Additional Information

- Best Paper Award (AP/EMC/MTT)
  Prepare your paper in two pages (A4) to apply for the Best Paper Award. The authors can choose one field among AP, EMC, and MTT during the online submission.
  The papers will be evaluated by the award committee, and the selected papers will be presented in the best paper presentation session for the final decision.
  Note that this is a separate session and the presenters are still requested to present their papers in general/special sessions.
- Best Paper Award for Business Corporations and Research Institutes
  If the first/corresponding authors are from business corporations or research institutions, the best paper award for the business corporations or research institutions can be applied.
  The submitted papers will be evaluated during the general/special sessions.
- Poster Session for the Undergraduate Students
  The undergraduate students can present their papers at the poster session, and the best papers will be selected by the session chairs.
- Special issues of the KIEES Korean Journal and the Journal of Electromagnetic Engineering and Sciences (JEES)*
  Papers recommended by the session chairs and those selected for the Best Paper Award can be published in a special issue of the Korean Journal of the KIEES or the JEES* after the regular peer-review process. A further development of the article is requested.
  *JEES(SCIE)
- Special Session
  Please contact secretariat (KIEES office) for information of the organization of the Special Sessions. Research groups, branches, research institutes, businesses corporations, and other organizations are welcome to apply.

KIEES office (Secretariat)

- Tel. +82-2-337-9666 (#4)
- Fax. +82-2-6390-7550
- E-mail : kees@kiees.or.kr

AUTHOR CHECKLIST

Title : _____

General

☐ This paper has not been and will not be published in any other journal.

☐ This paper follows the format of the KIEES paper submission guideline, is less than 12 pages long, including figures and tables (3 pages for a letter), and has a two-column layout.

☐ This paper includes a cover page, an abstract, keywords, main text, appendix, and references in the correct order. Each page has a consecutive page number.

Cover page

☐ The cover page includes the title, authors, affiliation of all authors, identifier of the corresponding author, and provides contact information for the corresponding author (phone number, e-mail address, and mobile number).

Abstract and key words

☐ An abstract is provided and is less than 500 words long.

☐ Fewer than 5 keywords are provided.

Main text

☐ The reference number is written next to the quote.

☐ The chapter numbers are written in Roman numerals (I, II, III, IV…) and subheading numbers are written in Arabic numerals (1, 2, 3, 4…).

References

☐ Sufficient Korean as well as international literature is referenced in the paper.

☐ Only the references used in the main text are included in the reference list and these are numbered according to their order of appearance.

☐ All reference citations follow the correct format indicated in the submission regulations.

Figures and tables

☐ For the figures and tables, the first letter of the very first word is capitalized.

☐ All figure legends include both a title and a detailed explanation to help in understanding what the figure depicts.

☐ All tables are self-explanatory and do not repeat the content from figures or sources included in the main text.

* Check each box after confirming that the statement is true.

The authors of this paper have confirmed the above items, following the paper submission regulations of *the Korean Institute of Electromagnetic Engineering and Science (KIEES)*, and are requesting publication of this paper.

_____/_____/ 2021

Representative author: _____ (signature)

Journal of Electromagnetic Engineering and Science

http://www.jees.kr

JEES
Volume 21, Number 2,
April, 2021

REGULAR PAPERS

ERRATUM